Politecnico di Milano
Scuola di Ingegneria Industriale e dell'Informazione
Laurea Magistrale in Ingengeria Nuclaeare

# Non-Evaporable Getter Thin Film Coatings for Vacuum Applications

*Autore:*
Chiara Barcellini

*Matricola:*
787014

*Anno Accademico:*
2014 – 2015

*Relatore:*
Prof. Marco Beghi
*Correlatore:*
Paolo Chiggiato

CERN Genève, September 2014

POLITECNICO DI MILANO

# *Abstract*

**Non-Evaporable Getter Thin Film Coatings for Vacuum Applications**

by Chiara BARCELLINI

Among the most challenging requisites for the design of an accelerator or a synchrotron there is the reaching of Ultra High Vacuum (UHV) conditions. This goal is reached in the Large Hadron Collider (LHC) coating the internal surface of some beam pipe sections with $Ti_{30}Zr_{30}V_{40}$ Non-Evaporable Getter (NEG) thin film.
During the Long Shutdown 1 (LS1), started in February 2013, some of the NEG coated vacuum chambers were exposed to the air of the LHC tunnel because of maintenance. It has been decided to study in details if the exposure to tunnel atmosphere for long periods affects the pumping properties of a NEG coated vacuum chamber. In the first part of this work the results obtained are presented; six $Ti_{30}Zr_{30}V_{40}$ coated vacuum chambers have been exposed for different periods and in different points of the tunnel. $H_2$ pumping speed and $CO$ saturation measurements have been performed. The results obtained suggest that the exposition at the LHC tunnel atmosphere does not affect the the pumping properties of the NEG coating. However, there have been problems in the activation of some chambers due to the experimental set-up. Further investigations are needed.
Other alloy, with properties close to those of $TiZrV$, exist and are suitable to becoming NEG thin film coating for vacuum applications; low activation temperatures and high pumping speed are looked for. In the present work three alloys have been tested: $ZrV$, $HfV$ e $TiZrHfV$. More than 30 stainless steel chambers have been coated and fully characterized: pumping speed and sticking probability have been evaluated, surface elemental chemical composition, morphology and crystallinity have been checked. The obtained results suggest that the activation temperature is liked to the nano-crystallinity: only nano-crystal samples have activation temperature compatible with the bake-out temperature of the vacuum chambers structural materials. The film crystallinity is affected by the composition: a certain percentage of vanadium is needed for having grains smaller than 5 $nm$. The pumping properties depends on the surface morphology and the from the elements present in the alloy.

POLITECNICO DI MILANO

# *Sommario*

**Non-Evaporable Getter Thin Film Coatings for Vacuum Applications**

by Chiara Barcellini

Tra i requisiti più stringenti da soddisfare nella costruzione di un acceleratore di particelle o di un sincrotrone, c'è sicuramente il raggiungimento di condizioni di ultra alto vuoto (UHV). Per il pompaggio di alcune sezioni del *Large Hadron Collider* (LHC), per esempio, si è scelto di usare i materiali *Non-Evaporable Getter* (NEG), in particolare il $Ti_{30}Zr_{30}V_{40}$.
Durante lavori di manutenzione di LHC si è presentata la necessità di esporre le camere rivestite di NEG all'atmosfera del tunnel. Si è quindi deciso di intraprendere uno studio sistematico degli effetti che l'esposizione può avere sulle proprietà di pompaggio dei film. Nella prima parte del presente lavoro di tesi sono presentati i risultati ottenuti; sei camere rivestite di un fin sottile di $Ti_{30}Zr_{30}V_{40}$ sono state esposte per diversi periodi e in diversi punti del tunnel. Misure di velocità di pompaggio per l'idrogeno e misure di saturazione per il monossido di carbonio sono state effettuate. I risultati ottenuti suggeriscono che l'esposizione all'atmosfera del tunnel di LHC non condizioni i rivestimenti interni di NEG delle camere a vuoto. Tuttavia, si sono riscontrati problemi dell'attivazione di alcune camere dovuti all'apparato sperimentale usato. Sono necessarie quindi ulteriori studi.
Esistono elementi che potrebbero essere adatti al rivestimento delle camere da vuoto; in particolare si è alla ricerca di materiali che possano essere depositati come film sottili ed abbiano caratteristiche simili a quelle del $TiZrV$: basse temperature di attivazione e grandi velocità di pompaggio. In questo lavoro di tesi sono state testate tre diverse leghe metalliche: $ZrV$, $HfV$ e $TiZrHfV$. Più di 30 camere di acciaio inossidabile sono state rivestite e completamente caratterizzate, sia da un punto di vista macroscopico (velocità di pompaggio e *sticking probability*), sia da una punto di vista microscopico (analisi di composizione chimica superficiale, analisi morfologiche e di cristallinità). Dai risultati ottenuti è possibile concludere che per tutte le leghe la temperature di attivazione è legata alla cristallinità del film: solo film nano-cristallini presentano basse temperature di attivazione. La dimensione dei grani cristallini di un film è influenzata dalla composizione della lega: è necessaria una certa percentuale di vanadio per ottenere grani più piccoli di 5 $nm$. Le caratteristiche di pompaggio sono invece legate alla morfologia superficiale e agli elementi presenti in lega; film rugosi, porosi e con strutture superficiali simili al $TiZrV$ hanno *sticking probability* e capacità superficiali elevate.

POLITECNICO DI MILANO

# *Sommario Esteso*

Nuclear Engineering
Energy Department

Master of Science in Nuclear Engineering

**Non-Evaporable Getter Thin Film Coatings for Vacuum Applications**

by Chiara Barcellini

Tra i requisiti più stringenti da soddisfare nella costruzione di un acceleratore di particelle o di un sincrotrone, c'è sicuramente il raggiungimento di condizioni di ultra alto vuoto (UHV). Durante gli anni diverse soluzioni sono state proposte per un pompaggio efficace di tubi con piccole conduttanze, dove il degasaggio spontaneo e indotto delle pareti metalliche rappresenta un limite per il raggiungimento del livello di vuoto desiderato. Tra le soluzioni, il rivestimento delle camere con film sottili di materiali *Non-Evaporable Getter* (NEG) è sicuramente quella attualmente più usata.
I NEG sono delle leghe metalliche in grado di chemi-adsorbire le più comuni molecole di gas presenti nelle camere da vuoto; possono essere depositati sulle pareti interne delle camere da vuoto in modo tale da trasformare queste ultime da sorgenti di gas a pompe chimiche. Tali materiali presentano alcuni vantaggi se paragonati alle pompe tradizionali: riducono il degasaggio termico, riducono il degasaggio indotto da ioni, abbassano la pressione minima ottenibile in una camera da vuoto, semplificano il progetto dei sistemi da vuoto ed, infine, riducono l'emissione di elettroni secondari.
La loro superficie attiva può essere creata durante il *bake-out* delle camere stesse per mezzo della diffusione termica dell'ossigeno contenuto nello strato di ossido superficiale nel *bulk* del materiale; tale processo lascia la superficie pulita e reattiva. La diffusione è termodinamicamente permessa ad una temperatura che prende il nome di temperatura di attivazione. Per un'applicazione efficace dei film sottili di NEG è necessario che quest'ultima sia compatibile con la temperatura di *bake-out* dei materiali strutturali della camere da vuoto.

L'acceleratore di particelle presente al CERN di Ginevra, il *Large Hadron Collider* (LHC), fa uso dei NEG: circa sei chilometri di camere da vuoto sono rivestiti di un film sottile di $Ti_{30}Zr_{30}V_{40}$. Tali camere sono state recentemente soggette a manutenzione e altri interventi sono programmati in vista dei lavori per l'aumento della luminosità d LHC.

Poichè durante i lavori le camere rivestiste sono esposte all'atmosfera del tunnel, è necessario sapere se essa influenzi le proprietà di pompaggio dei film sottili. Per questo motivo, è stato deciso al CERN di intraprendere uno studio sistematico degli effetti provocati dall'esposizione all'atmosfera dei tunnel di LHC sui film sottili di NEG, in modo tale da sapere come comportarsi in caso di apertura delle camere. In caso di danni gravi, potrebbe essere, infatti, necessario la sigillatura di tali camere da vuoto in atmosfera secca di azoto. Nella prima parte di questo lavoro saranno presentati presentati i risultati ottenuti fino ad ora in questo studio.
La campagna è stata organizzata rivestendo sei camere da vuoto di acciaio inossidabile con diametro di 10 $cm$ e lunghe 50 $cm$ con un film sottile di $Ti_{30}Zr_{30}V_{40}$; quattro di esse sono poi state esposte all'aria di due diversi punti di LHC per periodi differenti, una è stata usata come riferimento (non è stata esposta), mentre l'ultima è stata sigillata con azoto. Per tutte le camere è stata misurata la velocità di pompaggio per l'idrogeno e la capacità superficiale per il monossido di carbonio. Le misure sono state effettuate con un duomo di Fischer-Mommsen.
I risultati ottenuti suggeriscono che l'esposizione all'atmosfere del tunnel di LHC delle camere da vuoto rivestite con film sottili di NEG non danneggi le proferiteà di pompaggio. Tuttavia durante l'attivazione di alcune camere sono stati riscontrati problemi dovuti all'apparato sperimentale. Per questo motivo ulteriori indagini dovrebbero essere effettuate.

A seguito del loro utilizzo nella costruzione di LHC, i materiali NEG hanno ottenuto l'attenzione della comunità scientifica, in quanto è chiaro che essi sono la soluzione alla maggior parte dei problemi legati al raggiungimento delle condizioni di UHV. Uno studio sistematico di questi materiali risulta necessario all'ottenimento di una maggiore compressione delle loro proprietà e del meccanismo di attivazione. L'obbiettivo di questo studio è la ricerca di regole per l'individuazione di regole per la selezione di nuove leghe con basse temperature di attivazione e proprietà di pompaggio paragonabili a quelle del già noto $Ti_{30}Zr_{30}V_{40}$.
È noto che gli elementi del quarto gruppo della tavola periodica posseggono delle proprietà, quali un'alta solubilità per l'ossigeno e una buona diffusività, che li rendono ottimi candidati. Sfortunatamente, le temperature di attivazione dei loro film sottili non sono compatibili con le temperature di *bake-out* delle più comuni camere da vuoto. Nel presente lavoro si è studiato se possibile abbassare tali temperature aggiungendo nel film una certa percentuale di vanadio. Tre leghe sono state testate: $ZrV$, $HfV$ e $TiZrHfV$. Lo studio sistematico è stato organizzato rivestendo più di trenta tubi di acciaio inossidabile (10 $cm$ di diametro e lunghe 50 $cm$) con composizioni variabili delle leghe suddette. Misure di *sticking probability*, desorbimento indotto da elettroni e velocità di pompaggio sono state effettuate per caratterizzare le proprietà di pompaggio

dei film, mentre sono state fatte analisi microscopiche per il monitoraggio del processo di attivazione (XPS), della morfologia superficiale (SEM) e della cristallinità (XRD).
Si è verificato che la temperatura di attivazione è legata alla cristallinià dei campioni testati: solo film con grani, le cui immersioni sono minori di 5 $nm$, hanno temperature di attivazione al di sotto dei 200 °C. Le dimensioni dei dominii cristallini sono, invece, influenzate dalla composizione; per tutte le leghe testate è necessaria la presenza di una certa percentuale di vanadio per avere film nano-cristallini. Le propretà di pompaggio sono invece legate alla morfologia superficiale, che deve essere rugosa e porosa in modo da offrire grandi aree di interazione film-gas e da favorire le collisioni multiple, le quali aumentano la probabilità che una particella di gas interagisca efficacemente con il NEG.
Tra le testate quelle di $HfV$ risultano essere le meno performanti, mentre invece esistono composizioni di $ZrV$ e $TiZrHfV$ con proprietà che le rendono adatte all'applicazione nelle camere da vuoto. In particolare, si è osservato in due campioni di $TiZrVHfV$ un interessante comportamento a basse temperature, che suggerisce la possibilià che la loro temperatura di attivazione sia inferiore a quella del $Ti_{30}Zr_{30}V_{40}$. Ulteriori indagini sono però necessarie.

# *Acknowledgements*

This thesis is the result of a whole year of work, spent at the *Conseil Européen pour la Recherche Nucléaire* (CERN) as a technical student. I really enjoyed this experience mostly because of the people I met. Every one of them taught me something very valuable that increased my cultural baggage.

I am heartily grateful to Paolo Chiggiato, my CERN supervisor, for giving to me the possibility of working in a stimulating environment, where I confronted myself with the real scientific world and I put what I have studied in books in practice.

A special thank goes to Professore Marco Beghi, who has been my link between the CERN and the *Politecnico di Milano.* He helped me in the final steps of this thesis writing with a lot of precious suggestions.

I am also very grateful to my ex colleagues: Ivo, Tony, Chiara, Philippe and Gonzalo. They taught me what I now now about vacuum systems and helped me during my researches in various ways. The friendly working environment established by them was one of the reasons why waking up early in the morning was not so bad.

I cannot forget to thank the amazing people I met at CERN. They were able to transform *Genève* from a boring city into a place where I was glad to live. I will not forget all the dinners together, the trip around Italy and the cheerful moments spent together. I would like to list all of you but a page would not be enough, so I cite only the most important one: thank you Andrea.

Finally, a huge thank goes to my family. They always support me in all my decisions and encourage me every time I was not confident. I would not be here without them. I hope they are proud of me as much as I am happy to be part of this beautiful family.

# Contents


**Abstract** **i**

**Sommario** **ii**

**SommarioEsteso** **iii**

**Acknowledgements** **vi**

**Contents** **vii**

**List of Figures** **x**

**List of Tables** **xiv**

**Abbreviations** **xv**

**Physical Constants** **xvi**

**Symbols** **xvii**

**1 Evolution of Non Evaporable Getters Thin Films** **1**
- 1.1 Introduction . . . 1
- 1.2 From Pumping Strips to Thin Films Coatings . . . 3
- 1.3 NEG Thin Films First Application: ESRF Al-alloy vacuum Chamber . . . 6
- 1.4 The Large Hadron Collider . . . 7
- 1.5 Purpose of this study . . . 10

**2 General Properties of Non-Evaporable Getter Thin Films** **12**
- 2.1 General Considerations . . . 12
- 2.2 Selection of Getter Materials . . . 15
- 2.3 General Properties of $TiZrV$ films . . . 19
- 2.4 Vacuum Properties of $TiZrV$ films . . . 23

**3 Experimental Set-Up Characterization Methods** **28**
- 3.1 Pumping Speed Measurement . . . 28

3.1.1 Vacuum System Characteristic Quantities . . . . . . . . . . . . . . . 28
3.1.2 Fischer-Mommsen Dome . . . . . . . . . . . . . . . . . . . . . . . . . 34
3.1.3 Pumping Speed System Set-Up . . . . . . . . . . . . . . . . . . . . . 36
3.2 NEG Coated Chambers Preparation . . . . . . . . . . . . . . . . . . . . . . 38
3.2.1 Magnetron Sputtering . . . . . . . . . . . . . . . . . . . . . . . . . . 38
3.2.2 Sample Mounting . . . . . . . . . . . . . . . . . . . . . . . . . . . . 42
3.2.3 Deposition System Set-Up . . . . . . . . . . . . . . . . . . . . . . . . 45
3.3 Characterization Methods . . . . . . . . . . . . . . . . . . . . . . . . . . 46
3.3.1 Sticking Probability Evaluation . . . . . . . . . . . . . . . . . . . . . 47
3.3.2 Electron Stimulated Desorption . . . . . . . . . . . . . . . . . . . . . 49
3.3.3 ESD System Set-Up . . . . . . . . . . . . . . . . . . . . . . . . . . . 50
3.3.4 Scanning Electron Microscopy . . . . . . . . . . . . . . . . . . . . . . 52
3.3.5 X-Ray Photoelectron Spectroscopy . . . . . . . . . . . . . . . . . . . 55
3.3.6 X-Ray Diffraction . . . . . . . . . . . . . . . . . . . . . . . . . . . . 56

**4 Experimental Results 59**
4.1 Ageing Campaign . . . . . . . . . . . . . . . . . . . . . . . . . . . . . . . 59
4.1.1 Exposure Points . . . . . . . . . . . . . . . . . . . . . . . . . . . . . 60
4.1.2 Bake-out/Activation Procedure . . . . . . . . . . . . . . . . . . . . . 61
4.1.3 Experimental Results . . . . . . . . . . . . . . . . . . . . . . . . . . 63
4.2 Coating Campaign . . . . . . . . . . . . . . . . . . . . . . . . . . . . . . . 66
4.2.1 Reference Sample: $Ti_{29}Zr_{31}V_{40}$ . . . . . . . . . . . . . . . . . . . . . 67
4.2.2 $ZrV$ Campaign . . . . . . . . . . . . . . . . . . . . . . . . . . . . . 71
4.2.3 $HfV$ Campaign . . . . . . . . . . . . . . . . . . . . . . . . . . . . . 77
4.2.4 $TiZrHfV$ Campaign . . . . . . . . . . . . . . . . . . . . . . . . . . 84

**5 Discussion of the results 93**
5.1 Ageing Campaign: Influence of the LHC tunnel atmosphere . . . . . . . . 93
5.2 Coating Campaign: Influence of Vanadium on the $IV$ Group Elements . . 95

**6 Conclusions 103**

**A Pumping Speed Measurements Procedure 106**
A.1 Pumping Speed Measurement Procedure for the Ageing Campaign Samples 106
A.2 Pumping Speed Measurement Procedure for the Coating Campaign Samples 109

**B Coating Procedure 112**
B.1 Stainless Steel Tubes Cleaning Procedure . . . . . . . . . . . . . . . . . . 112
B.2 Stainless Steel Tubes Coating Procedure . . . . . . . . . . . . . . . . . . . 113

**C Sticking Probability and ESD Measurement Procedure 115**
C.1 Mounting and Dismounting Samples . . . . . . . . . . . . . . . . . . . . . 116
C.1.1 Dismounting Samples . . . . . . . . . . . . . . . . . . . . . . . . . . 116
C.1.2 Mounting Samples . . . . . . . . . . . . . . . . . . . . . . . . . . . . 117
C.1.3 Leak Detection . . . . . . . . . . . . . . . . . . . . . . . . . . . . . . 117
C.1.3.1 Procedure 1 . . . . . . . . . . . . . . . . . . . . . . . . . . 118
C.1.3.2 Procedure 2 . . . . . . . . . . . . . . . . . . . . . . . . . . 118

C.2 Bake-out Procedure . . . 119
C.2.1 Full Bake-out . . . 119
C.2.2 Partial Bake-out . . . 121
C.3 Activation Procedure . . . 122
C.4 Sticking Probability Measurements . . . 125
C.5 Electron Stimulated Desorption Measurements . . . 127

**Bibliography** **129**

# List of Figures

1.1 In the map are located all the facilities currently using NEG thin films (red points) and the ones under construction where the are going to be used (green points). . . . 3
1.2 Design of the cross-section of a LEP vacuum chamber[1] . . . 4
1.3 First prototype of the LEP dipole beam pipe with the St101 NEG strip in the antechamber (1983). . . . 4
1.4 NEG total pump. . . . 5
1.5 Cross section of the $TiZrV$ coated ESRF vacuum chamber. . . . 7
1.6 Conceptual scheme of the CERN accelerator complex. . . . 8
1.7 A stock of NEG coated vacuum chamber ready to be installed in the LHC tunnel. . . . 9

2.1 Results of the ESD measurements performed with an applied voltage of 500 $V$ and a current through the electron source of 1 $mA$. . . . 16
2.2 Results of the ESD measurements for the $V$ group elements, performed with an applied voltage of 500 $V$ and a current through the electron source of 1 $mA$. . . . 17
2.3 Comparison between the ESD results for Stainless Steel, $TiZr$ and $TiZrV$, performed with an applied voltage of 500 $V$ and a current through the electron source of 1 $mA$[2]. . . . 18
2.4 XPS measurements performed with a SPECS EA10P hemispherical analyzer using a non-monochromatic $Al$ $K_\alpha$ radiation as excitation source[2]. 18
2.5 Ultimate pressure as a function of the heating temperature for a 50 $mm$ inner diameter chamber coated with $Ti_{30}Zr_{20}V_{50}$. . . . 19
2.6 Composition maps for $TiZrV$ thin films[3]. . . . 20
2.7 Influence of the substrate nature on the coating roughness[4]. . . . 21
2.8 SEM imagines of $TiZrV$ thin film sputtered on different type of copper substrates; all the films in the left column are deposited on smooth copper, meanwhile the ones in the right on rough copper [5]. . . . 22
2.9 Sticking probability for $H_2$ (red points) and $CO$ (blue points) as a function of the heating temperature. The measurements are performed after two hour of heating at different temperatures (see **Chapter 3** for the measurement procedure). . . . 24
2.10 Variation of the effective molecular desorption yield as a function of the beam and photon dose measured on a $TiZrV$ coated stainless steel vacuum chamber installed on a beam line at ESRF (Grenoble)[6]. . . . 26

3.1 Schematic representation of the simplest geometry for the conductance calculation. . . . 31

3.2 Schematic drawing of a gas flow restriction of conductance $C$ interposed between a pump of pumping speed $S$ and a vacuum vessel. . . . . . . . . 32
3.3 Capture probability in faction of the sticking probability for a DN100 stainless steel tubes 50 $cm$ long. . . . . . . . . . . . . . . . . . . . . . . . . . 33
3.4 Schematic representation of a Fischer-Mommsen dome[7]. . . . . . . . . . 34
3.5 Sketch of the pumping speed system used for testing the NEG coated vacuum chambers. . . . . . . . . . . . . . . . . . . . . . . . . . . . . . . . 36
3.6 Schematic representation of the magnetron sputtering configuration used for the realization of the sample tested. . . . . . . . . . . . . . . . . . . . 39
3.7 Examples of some of the cathodes used for the realization of the NEG thin film coatings tested. . . . . . . . . . . . . . . . . . . . . . . . . . . . . 43
3.8 Pictures of the main coating tower components. . . . . . . . . . . . . . . . 44
3.9 Scheme of the deposition system used for the production of all the NEG thin films tested. . . . . . . . . . . . . . . . . . . . . . . . . . . . . . . . . 45
3.10 Pictures of the deposition system. . . . . . . . . . . . . . . . . . . . . . . . . 46
3.11 $R$ parameter in function of the sticking probability for the ESD system obtained by a Monte Carlo simulation. . . . . . . . . . . . . . . . . . . . . . 48
3.12 Picture of the electron source used for the electron stimulated desorption measurement. . . . . . . . . . . . . . . . . . . . . . . . . . . . . . . . . . . 50
3.13 ESD system: it has been used for performing both the sticking probability and the electron stimulated desorption measurements. . . . . . . . . . . . 50
3.14 Example of the samples used for the SEM measurement. In this case the two copper substrate are coated with $Ti_{30}Zr_{30}V_{40}$. . . . . . . . . . . . . . . 53
3.15 Examples of SEM imagines of a $Ti_{30}Zr_{30}V_{40}$ surface. . . . . . . . . . . . . 53
3.16 ESD spectrum of $Ti_{30}Zr_{30}V_{40}$ top sample. . . . . . . . . . . . . . . . . . . 54
3.17 Scheme of the experimental apparatus needed for performing a XPS measurement. . . . . . . . . . . . . . . . . . . . . . . . . . . . . . . . . . . . 55
3.18 Representation of diffraction process. . . . . . . . . . . . . . . . . . . . . . . 57

4.1 Exposure Points. . . . . . . . . . . . . . . . . . . . . . . . . . . . . . . . . 60
4.2 Bake-out/Activation procedure. . . . . . . . . . . . . . . . . . . . . . . . . 62
4.3 Comparison between the $CO$ saturation measurements performed on sample **LSS3_1** after the second activation (blu curve) and the air exposure (magenta curve). . . . . . . . . . . . . . . . . . . . . . . . . . . . . . . . . 64
4.4 Pressure during the bake-out/activation procedure of sample **LSS1_1**. . 65
4.5 SEM profile of $Ti_{29}Zr_{31}V_{40}$ top: scale 200 $nm$, EHT 5 $kV$ and magnification 30 K X. . . . . . . . . . . . . . . . . . . . . . . . . . . . . . . . . . 68
4.6 SEM imagines of $Ti_{29}Zr_{31}V_{40}$. . . . . . . . . . . . . . . . . . . . . . . . . 68
4.7 Not smoothened XRD spectrum of $Ti_{29}Zr_{31}V_{40}$: $Cu$ K$\alpha$ source, $2\Theta$ from 25°to 145°, step size $0,01°$, step lasting 3 $s$. . . . . . . . . . . . . . . . . . 69
4.8 Sticking probability and ESD measurements for $Ti_{29}Zr_{31}V_{40}$. . . . . . . . 70
4.9 Results of the ESD measurements performed with an applied voltage of 500 $V$ and a current through the electron source of 1 $mA$ for the $ZrV$ samples tested. . . . . . . . . . . . . . . . . . . . . . . . . . . . . . . . . . 71
4.10 Surface morphology of $Zr_{91}V_9$ and $Ti_{29}Zr_{31}V_{40}$. . . . . . . . . . . . . . . . 72
4.11 Comparison between the $H_2$ and $CO$ sticking probability of sample $Zr_{99}V_9$ and $Ti_{29}Zr_{31}V_{40}$. . . . . . . . . . . . . . . . . . . . . . . . . . . . . . . . . 72

4.12 Results of the ESD measurements performed with an applied voltage of 500 $V$ and a current through the electron source of 1 $mA$ for $Zr_{99}V_9$ (blu squares) compared with $Ti_{29}Zr_{31}V_{40}$ (red dots). . . . . 73
4.13 Comparison between the $H_2$ and $CO$ sticking probability of sample $Zr_{72}V_{28}$, $Zr_{68}V_{32}$, $Zr_{69}V_{31}$ (magenta stars) and $Ti_{29}Zr_{31}V_{40}$. . . . . 74
4.14 Results of the ESD measurements performed with an applied voltage of 500 $V$ and a current through the electron source of 1 $mA$ for $Zr_{72}V_{28}$ (blu squares) and $Zr_{68}V_{32}$ (green triangles), $Zr_{69}V_{31}$ (magenta stars) compared with $Ti_{29}Zr_{31}V_{40}$ (red dots). . . . . 75
4.15 Surface morphology of $Zr_{72}V_{28}$ and $Zr_{67}V_{33}$. . . . . 75
4.16 Comparison between the XPS spectra of $Zr_{12}V_{88}$ for all the heating temperatures (photon energy 1253, 6 $eV$, time per step 50 $s$, sweep 16.) . . . 76
4.17 Comparison between the $H_2$ and $CO$ sticking probability of sample $Zr_{12}V_{88}$, $Zr_{36}V_{64}$ and $Ti_{29}Zr_{31}V_{40}$. . . . . 77
4.18 Surface morphology of $Zr_{12}V_{88}$ and $Zr_{13}V_{87}$. . . . . 77
4.19 Results of the ESD measurements performed with an applied voltage of 500 $V$ and a current through the electron source of 1 $mA$ for the $HfV$ samples tested. . . . . 78
4.20 Details of $Hf_{95}V_5$ XPS spectrum: . . . . . 79
4.21 Surface morphology of $Hf_{95}V_5$ and $Ti_{29}Zr_{31}V_{40}$. . . . . 79
4.22 Comparison between the ESD results of results of $Hf_{95}V_5$ (blu squares) and $Ti_{29}Zr_{31}V_{40}$ (red dots). The measurements have been performed with an applied voltage of 500 $V$ and a current through the electron source of 1 $mA$. . . . . 80
4.23 Details of XPS spectra for $Hf_{70}V_{30}$ and $Hf_{65}V_{35}$. . . . . 81
4.24 SEM imagines of the $HfV$ samples . . . . . 82
4.25 XPS and ESD results for samples $Hf_{45}V_{55}$, $Hf_{40}V_{60}$ and $Hf_{45}V_{55}$ . . . . . 83
4.26 SEM imagines of the $HfV$ samples . . . . . 83
4.27 Results of the ESD measurements performed with an applied voltage of 500 $V$ and a current through the electron source of 1 $mA$ for the $TiZrHfV$ samples tested. . . . . 84
4.28 $H_2$ and $CO$ sticking probabilities for $Ti_{23}Zr_{13}Hf_{39}V_{25}$ and $Ti_{22}Zr_3Hf_{44}V_{31}$ compared with the results obtained for $Ti_{29}Zr_{31}V_{40}$. . . . . 85
4.29 Results of the ESD measurements for $Ti_{29}Zr_{31}V_{40}$ (red dots), $Ti_{23}Zr_{13}Hf_{39}V_{25}$ (blu squares) and $Ti_{22}Zr_3Hf_{44}V_{31}$ (green triangles) as a function of the heating temperature (500 $V$, 1 $mA$ and 100 $s$). . . . . 86
4.30 SEM imagines of surfaces and profiles of $Ti_{23}Zr_{13}Hf_{39}V_{25}$ and $Ti_{22}Zr_3Hf_{44}V_{31}$. 87
4.31 Not smoothed XRD spectrum of $Ti_{22}Zr_3Hf_{44}V_{31}$: $Cu$ K$\alpha$ source, $2\Theta$ form 25°to 145°, step size 0, 01°and step lasting 3 $s$. . . . . 87
4.32 Decrease of the $O1s$ area as a function of the heating temperature for $Ti_{23}Zr_{13}Hf_{39}V_{25}$ (blu squares) and $Ti_{22}Zr_3Hf_{44}V_{31}$ (green triangles). . . 88
4.33 $H_2$ and $CO$ sticking probabilities for $Ti_{25}Zr_{23}Hf_{40}V_{12}$ and $Ti_{13}Zr_{12}Hf_{55}V_{20}$ compared with the results obtained for $Ti_{29}Zr_{31}V_{40}$. . . . . 88
4.34 $Ti_{17}Zr_{29}Hf_{30}V_{24}$ $CO$ pumping speed in function of the total number of $CO$ molecules injected in the Fisher-Mommsen dome. . . . . 89
4.35 SEM imagines of $Ti_{17}Zr_{29}Hf_{30}V_{24}$. . . . . 90

4.36 $H_2$ pumping speed in function of the activation time for $Ti_{31}Zr_{29}V_{40}$ (red dots), $Ti_{13}Zr_{24}Hf_{41}V_{21}$ (blue squares) and $Ti_3Zr_3Hf_{19}V_{76}$ (green triangles). . . . . 91

5.1 Grain size in function of the vanadium atomic percentage fir all the NEG materials tested. . . . . 94
5.2 Comparison between the CO saturation measurements of the samples tested in the ageing campaign. . . . . 95
5.3 $H_2$ sticking probability and grain size for all the $ZrV$ sample tested. . . . 97
5.4 $H_2$ sticking probability and grain size for all the $HfV$ sample tested. . . . 99
5.5 Characteristic surface structures found in some $HfV$ samples. . . . . . 100
5.6 Grain size in function of the vanadium atomic percentage fir all the NEG materials tested. . . . . 101
5.7 $H_2$ sticking probability in function of the vanadium percentage in the film for all the three alloys tested. . . . . 102

C.1 ESD system: it has been used for performing both the sticking probability and the electron stimulated desorption measurements. . . . . 115
C.2 ESD system particular of the injection line used for the sticking probability measurementszs. . . . . 116

# List of Tables

1.1 Maximun heating temperature allowed for the structural material of particle accelerators vacuum chambers. . . . . 6
1.2 Main coating parameters used for the realization of the LSSs LHC beam pipes. . . . . 9

2.1 Numerical values of the diffusion length (L) for oxygen for 2 $h$ of heating at 300 °C and of the oxygen solubility limit at 300 °C [5]. . . . . 14

3.1 Pumping speed system main characteristics. . . . . 38
3.2 Sputtering threshold values for suitable NEG materials bombarded with $Kr$. . . . . 40
3.3 Sputtering yield for the materials used bombarded with $Kr$ at 500 $V$. . . . 42
3.4 Materials used for the cathodes fabrication. . . . . 44
3.5 Example of the EDS results for a $TiZrV$ NEG thin film. . . . . 54

4.1 List of the samples with the respective point and duration of the exposure. 60
4.2 Bake-out and Activation Procedure for the samples. . . . . 61
4.3 Summary of the experimental results obtained. . . . . 63
4.4 Coating parameters. . . . . 66
4.5 $Ti_{29}Zr_{31}V_{40}$ cathode composition. . . . . 67
4.6 Composition of the coating in atomic percentage. . . . . 67
4.7 Coating thickness. . . . . 68
4.8 Sticking factor for $H_2$ and $CO$ and variation of the total pressure afte the electron bombardment for sample $Ti_{29}Zr_{31}V_{40}$. . . . . 69
4.9 XPS acceptance requirements for $Ti_{23}Zr_{13}Hf_{39}V_{25}$ and $Ti_{22}Zr_3Hf_{44}V_{31}$ 88
4.10 $H_2$ pumping speed for the $TiZrHfV$ sample tested. . . . . 91

5.1 $H_2$ capture probability and sticking probability for the samples tested in the ageing campaign. . . . . 94
5.2 Main information of the $ZrV$ samples tested. In the cathode column the equivalent diameter of the wires used is reported for $Zr$ and $V$ respectively. 96
5.3 Main information of the $HfV$ samples tested. In the cathode column the equivalent diameter of the wires used is reported for $Hf$ and $V$ respectively. 98
5.4 Main information of the $TiZrHfV$ samples tested. In the cathode column the equivalent diameter of the wires used is reported for $Ti$, $Zr$, $Hf$ and $V$ respectively. . . . . 100

C.1 Heating temperatures of a full bake-out of the ESD system. . . . . 122
C.2 Heating temperatures of a partial bake-out of the ESD system. . . . . 123
C.3 Steps of the ESD activation procedure. . . . . 125

# Abbreviations

| | |
|---|---|
| **bcc** | **b**ody-**c**entered **c**ubic |
| **EDS** | **E**nergy **D**ispersive X-rays **S**pectroscopy |
| **ESD** | **E**lectron **S**timulated **D**esorption |
| **fcc** | **f**ace-**c**entered **c**ubic |
| **hcp** | **h**exagonal-**c**losed **p**acked |
| **LEP** | **L**arge **E**lectron **P**roton collider |
| **LHC** | **L**arge **H**adron **C**ollider |
| **LS1** | **L**ong **S**hut-down **1** |
| **LSS** | **L**ong **S**traight **S**esction |
| **NEG** | **N**on-**E**vaporable **G**etter |
| **SEY** | **S**econdary **E**electron **Y**ield |
| **UHV** | **U**ltra **H**igh **V**acuum |
| **XPS** | **X**-Rays **P**hotoelectron **S**pectroscopy |

# Physical Constants

| | | | |
|---|---|---|---|
| Boltzmann Constant | $k_B$ | = | $1,386488(13)\ 10^{-23}$ J $K^{-1}$ |
| Avogadro number | $N_A$ | = | $6,02214129(27)\ 10^{23}$ $mol^{-1}$ |
| Molar Gas Constant | R | = | $8,314$ J $K^{-1}$ $mol^{-1}$ |

# Symbols

| | | |
|---|---|---|
| A | area | $m^2$ |
| BE | binding energy | eV |
| C | conductance | $l\ s^{-1}$ |
| C′ | conductance per unit surface | $l\ s^{-1}\ m^{-2}$ |
| D | diffusivity | $m\ s^{-1}$ |
| G | Gibbs free energy | J |
| H | enthalpy | J |
| $K_n$ | Knudsen number | 1 |
| L | diffusion length | nm |
| m | mass | kg |
| N | number of molecules | 1 |
| n | number of molecules per unit volume | $m^{-3}$ |
| P | pressure | Torr |
| $\dot{Q}$ | gas flow | $Pa\ m^3\ s^{-1}$ |
| $Q_p$ | pump throughput | $Pa\ m^3\ s^{-1}$ |
| S | pumping speed | $l\ s^{-1}$ |
| S | entropy | $J\ K^{-1}$ |
| $S_{eff}$ | effective pumping speed | $l\ s^{-1}$ |
| T | temperature | K |
| t | time | s |
| V | volume | $m^3$ |
| $x_0$ | solubility limit | 1 |
| | | |
| $\alpha$ | sticking probability | 1 |
| $\bar{\lambda}$ | mean free path | m |

| | | |
|---|---|---|
| $\sigma$ | capture probability | 1 |
| $\tau$ | sojourn time | s |
| $\phi$ | molecular impingement rate | $m^{-2}$ $s^{-1}$ |
| $\omega$ | grain size | nm |

*a nonno Francesco...*

# Chapter 1

# Evolution of Non Evaporable Getters Thin Films

## 1.1 Introduction

There are currently more than 30000 accelerators in operation around the world[8], which are doing a variety of jobs; most of them are used for industrial porpoises (ion implantation and sterilization), others for the production of radioactive isotopes for medical treatments, and other for condensed matter (synchrotrons) or particles physics (colliders) studies.
A constantly deeper knowledge of the structure of the matter requests machine with higher particles energy and beam intensities. Therefore, accelerators, in particular synchrotrons and colliders, need new technological solutions for reaching these two goals. A massive effort is required in order to satisfy all the requirements and often the chosen solutions are a trade-off between incompatible features.
Among the most challenging requisites there are the creation of electric and magnetic fields for accelerating and bending the particles, the reaching of cryogenic temperatures, the design and realization of particles detectors and the reaching of Ultra High Vacuum (UHV) conditions.

Ultra High Vacuum (UHV) is needed in particles accelerators in order to

- reduce the gas-beam scattering;

- reduce the risk of high voltage discharge;

- to improve the thermal insulation.

The level of vacuum required depends on the degree of beam degradation which can be tolerated during the passage through the machine[9]. Geometrical degradations, intensity losses by both Coulomb and nuclear scattering with the residual gases and energy losses through molecular excitations and Bremsstrahlung are expected.
The presence of gases inside the vacuum chambers is, therefore, one of the limiting causes of the accelerator performance and solutions for lowering it as much as possible are looked for. The pressure inside the machines is mainly due to the outgassing of their walls (static pressure) and to their beam dependent degassing; the beam ions or the synchrotron radiation may, in fact, stimulate the gas desorption of the inner surface of the vacuum chambers.
Vacuum chambers are designed in order to keep the pressure of the machine at the required level. A standard UHV vacuum system consists of an all-metal chamber to which one or many pumps are connected by means of flanges[10]. This standard configuration works until the 70's, when the progressive reduction of the vacuum chambers aperture (thus of the conductance) and the increasing of machine length, both due to the necessity of more energetic beams, makes this pumping approach very impractical, particularly in the presence of strong degassing induced by synchrotron radiation.

During the years many solutions were proposed in order to obtain a distributed and continuous pumping which is preferable in the case of the new type of vacuum chambers needed for the the large accelerators; one of them makes use of Non Evaporable Getter materials. They are metal alloys able to chemically react with gas molecules in order to form stable compounds; their active surface is obtained by thermal diffusion of the surfaces contaminants into the bulk of the material itself[5].
A study on the ultra-high vacuum behavior of NEG, lasted about 20 year at CERN, resulted in the evolution from standard vacuum system configuration to the total NEG pump solution. It consisted in completely covering of the inner surface of a vacuum chamber with St707 strips. This evolution not only helps to improve the vacuum characteristic of the getters, but also move the pumps progressively closer to the vacuum chambers walls.

The total NEG pumps allow to have larger pumping speed and smaller pump dimensions, but do not solve the problem of gas load. A substantial decrease of it could be reached if the NEG pumps is tightly joined to the vacuum chamber walls, as could be achieved by coating the whole chamber surface with a NEG thin film.
Vacuum chambers coated with a NEG thin film may be transformed from a gas source into a pump by activating the getter coating during a standard *in situ* bake-out.

NEG thin films were developed and studied at CERN between 1995 and 2002 becoming

the winning solution for vacuum systems of high-energy physics and synchrotron radiation facilities. By far the most significant benchmark for such films is the Large Hadron Collider (LHC) at CERN, where about 6 $km$ of beam pipes are coated with $TiZrV$ thin films[11].

The 1200 coated vacuum chambers of LHC Long Straight Sections (LSSs) are not the arrival point of the NEG thin films story but the starting point for new researches aimed to improve the NEG vacuum properties in order to satisfy the incoming requests of the UHV users.

In **Figure 1.1** all the facilities using NEG thin film coating are individuate; it could be seen that the NEG thin films have reached a world wide success.

FIGURE 1.1: In the map are located all the facilities currently using NEG thin films (red points) and the ones under construction where the are going to be used (green points).

In the following sections of this chapter a brief story of the development of NEG thin film coatings at CERN is reported.

## 1.2 From Pumping Strips to Thin Films Coatings

Getter materials have been used as passive pumps in the accelerators since long time. The Large Electron Proton collider (LEP) was one of the first machines where the integrated linear pumping involving NEG materials appeared to be an appropriate solution to the new geometrical constraints. A linear Non-Evaporable Getter pump was preferred to the integrated sputter-ion pumps, since it does not need a magnetic field for operation. Sputter-ion pumps, in fact, make use of the accelerator dipole magnetic field, which in case of LEP was only $2 \cdot 10^{-2}$ $T$ at the injection energy, therefore too close to the pump ignition threshold[12].

In **Figure 1.2** the cross-section of the LEP dipole beam pipe is shown, meanwhile in **Figure 1.3** a picture of the prototype chamber is reported. It could be seen in both figures that the St101 NEG strip needed a dedicated pumping channel parallel to the beam chamber.

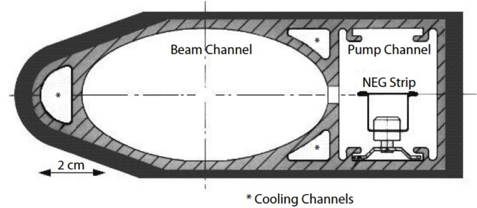


FIGURE 1.2: Design of the cross-section of a LEP vacuum chamber[1]

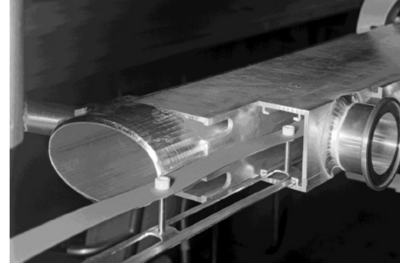

FIGURE 1.3: First prototype of the LEP dipole beam pipe with the St101 NEG strip in the antechamber (1983).

The adopted NEG pumping solution covered about 23 $km$ of the 27 $km$ of the LEP machine. It consisted in a 30 $mm$ wide constantan strips coated both sides with 100 $\mu m$ thick layer of $Zr_{84}Al_{16}$ (weight percentage) powder, which can be clearly seen in **Figure 1.3**. This strip provided a pumping speed for $H_2$ of about 2000 $l \cdot s^{-1} \cdot m^{-1}$; the ultimate pressure which they could produce was limited by the outgassing of $CH_4$ and $Ar$, gasses not pumped by NEGs[12].
After air exposure the active surface of a NEG pump must be obtained by heating; the activation of St101 NEG requires heating at 750 °C for half an hour, which was done for LEP by means of a 90 $A$ current passing through the strips. Ohmic heating needs electrical feedthroughts and electrical insulation, which limits the amount of strips that can be installed in a given volume, therefore the maximum pumping speed.
A problem met during the development of the NEG pumping system for LEP was the inner walls vacuum chambers degassing induced by synchrotron radiation; it causes not only a much higher pressure in the machine beam pipes, but also a progressive decrease of the pumping speed, due to the room temperature chemisorption of $CO$ and $CO_2$, which remained stuck on the NEG surface inhibiting further gas adsorptions. A study of the decreasing of the pumping speed as a function of the quantity and the nature of the gasses showed that porosity plays a dominant role in defining the room temperature NEG performance. The increased porosity of the NEG strips used for LEP (from 7% to 13%) allowed to minimize the frequency of the heating cycles needed for diffusing the pumped gasses into the bulk material restoring, therefore, the pumping speed.

The necessity of heating cycles for restoring the pumping speed was a huge problem to overcome, since the heating was not feasible during the LEP operation. Other pumping solutions had to be found for the upgrade of the machine.

Lowering the activation temperature of the NEG may allow a passive activation of the strips during the bake-out of the vacuum chambers. This can be achieved using the NEG Strips St707 ($Zr_{70}V_{24,6}Fe_{5,4}$ weight percentage), whose activation temperature is around 400 °C compatible with stainless steel vacuum chamber bake-out temperature.The already mentioned total NEG pump relies on this kind of strips and allows to pumping speed larger than $10^4\ l \cdot s^{-1} \cdot m^{-1}$ and pressure in the $10^{-14}\ Torr$ range[13].

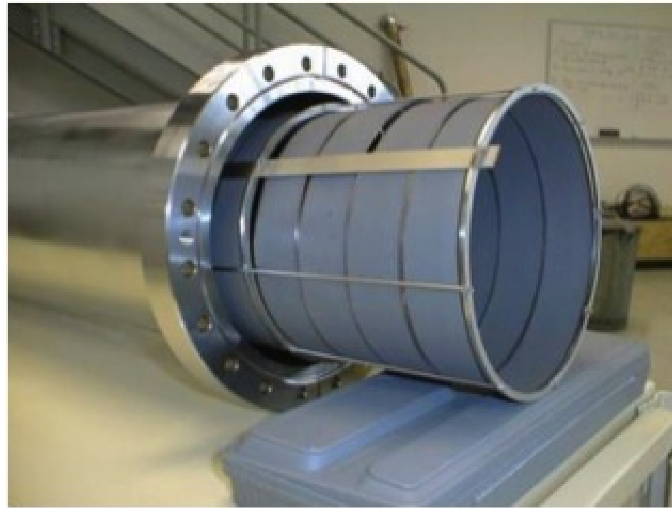

FIGURE 1.4: NEG total pump.

Completely covering the inner surface of a vacuum chamber with St707 strips (as it is shown in **Figure 1.4**) improve both the pumping efficiency, since the pump is closer to the wall, and increase the applied pumping speed, since there is no need of electrical insulation and feedthroughts, but do not affect the outgassing of the chamber walls nor solve the space constraint problems. The ideal solution to the problem would consist in coating *ex situ* the whole inner vacuum chamber surface with a thin film of non evaporable getter material, providing a low activation temperature in order to allow its activation by *in situ* baking: the coating non only transform the walls into a pump, but also prevent the outgassing[2].

Cristoforo Benvenuti in the early 80's had the first idea of coating the inner wall of a vacuum chamber with NEG materials: he tried to sputter St101 strip in a LEP chamber, obtaining en excellent ultimate pressure. The only problem was the impossibility of re-activation after air exposure. Other materials were sputtered and their desorption yield were measured. A systematic study of the feasibility of NEG thin film coatings was launched at CERN at the end of 1995. It was immediately clear that the suitable material for a NEG thin film coating should have had vacuum properties close to the ones of NEG strips and an activation temperature compatible with the baking temperature of the vacuum chambers most common materials. In **Table 1.1** the heating limits of these materials are reported.

TABLE 1.1: Maximun heating temperature allowed for the structural material of particle accelerators vacuum chambers.

| **Material** | **Maximum Heating Temperature** |
|---|---|
| Stainless Steel | 350 |
| Copper Alloys | 250 |
| Aluminium Alloys | 200 |
| Beryllium | 200 |

The study reached its goal: the NEG material, with vacuum properties close to the one of the strips was found to be $Ti_{30}Zr_{30}V_{40}$ (atomic percentage). This material can be *ex-situ* sputtered on the whole inner surface of vacuum chambers. With this solution the transition from bulk getter materials to thin film getter coating happened.
Around 2000 the non-evaporable getter thin films were used for the first time in a machine in order to solve some design problems.

## 1.3 NEG Thin Films First Application: ESRF Al-alloy vacuum Chamber

The European Synchrotron Radiation Facility (ESRF) in Grenoble was the first accelerator where the non-evaporable getter thin films were used to solve design problems; in fact, between 2000 and 2002 eleven NEG coated vacuum chambers, with different cross-section and made of different materials, have been installed[14].
The NEG coating was found to be a relatively low-cost solution for the issues related to the installation in a straight section of a narrow-gap vacuum chamber. This chamber affected the storage ring operation manly for two reasons: high outgassing, which increased the pressure in the ring reducing the lifetime of the circulating beam, and high amount of bremsstrahlung radiation, which made the induced radioactivity no longer in the european radio-protection limits.
The NEG thin film coatings studied at CERN seemed to be a solution, since after the activation not only they makes the vacuum chamber walls to become a pump, increasing the system pumping speed per meter, but make them also a very clean surface with a lower photo-desorption yield[15].
The first chamber which have been tested is shown in **Figure 1.5**[16]; it is a low-gap, extruded-aluminum vacuum chamber with a $Ti_{30}Zr_{30}V_{40}$ coating, performed at CERN. It has been activated 5 times and vented 6 without noticeable degradation in its performances.

The vacuum chambers installed at the ESRF showed no liming machine issued related to the presence of the NEG material: the resistive-wall impedance was very marginally

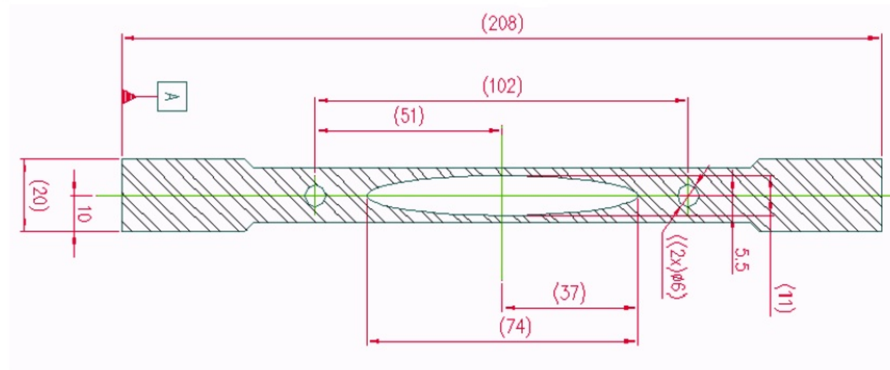


FIGURE 1.5: Cross section of the $TiZrV$ coated ESRF vacuum chamber.

affected and no generation of dust or peeling-off had been observed.
The chambers installed at the ESRF proved that non only the NEG thin film coating were feasible, but also that NEG coated vacuum chambers could become the standard for UHV vacuum systems.

In the meantime at CERN it was planned to make a massive use of these thin films in the new machine under construction, the Large Hadron Collider (LHC).

## 1.4 The Large Hadron Collider

The most significant application of non-evaporable getter thin films are by far the Large Hadron Collider (LHC) at the *Conseil Européen pour la Recherche Nucléaire* (CERN) where about 6 $km$ of beam pipes are coated with NEG.

The Large Hadron Collider, whose construction was approved in 1994, is a machine for accelerating hadrons and making them collide; in particular, it is used to accelerate protons and heavy ions of lead. It is the last element of the CERN accelerator complex shown in **Figure 1.6**. Each machine of the complex injects the particle beam into the next one, which takes over to bring the beam to an even higher energy and so on.

LHC is the last and the biggest accelerator of the complex: it has circumference of 27 $km$ and it is able to accelerate protons to 7 $TeV$ and gives to lead ions a collision energy of 1150 $TeV$. It is composed of arcs, where the superconducting magnets bend the beams and Long Straight Sections (LSSs), where the two beams are accelerated, or injected, or extracted or monitored. In four points of the LSSs are placed the CERN biggest experiments where the two circulating beams collide: CMS, ATLAS, ALICE and LHCb.
With the first start-up in 2008, the LHC become the biggest operational vacuum system in the world with 104 $km$ of piping under vacuum. It is divided into three different

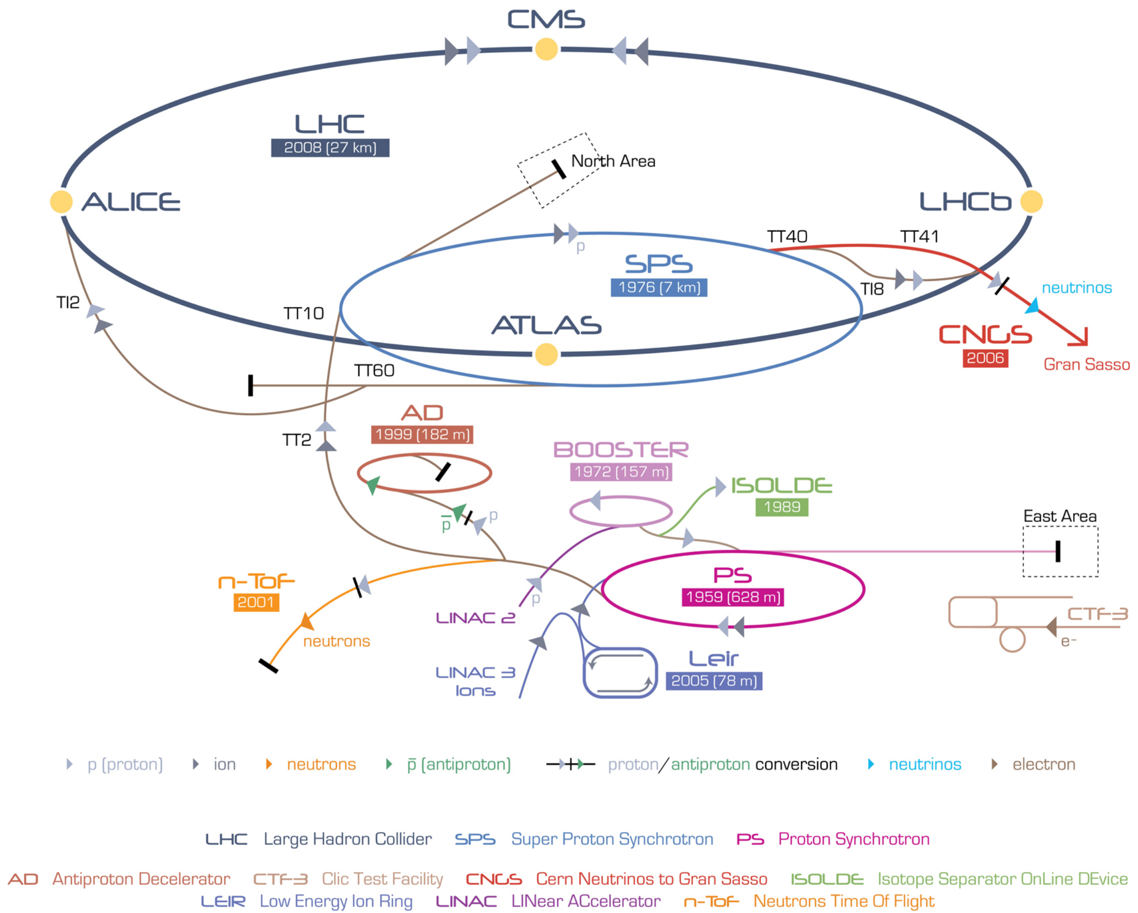


FIGURE 1.6: Conceptual scheme of the CERN accelerator complex.

systems each of them is designed to reach certain goals. One system is used for insulating the cryogenically cooled magnets, one for insulating the helium distribution line and one for the 54 $km$ of pipes, where the beams travel. The last one, where a pressure in the order of $10^{-10}$ to $10^{-11}$ $mbar$ is needed, consists in:

- 48 $km$ of arc sections kept at $1,9$ $K$ and pumped by cryogenic pumps;
- 6 $km$ of straight sections (LSSs) kept at room temperature, pumped by 780 ion pumps and coated with NEG thin films.

In the LHC are, thus, installed 1200 vacuum chambers coated with $Ti_{30}Zr_{30}V_{40}$ in order to provide a distributed pumping speed and a low Secondary Electron Yield (SEY). In order to produce all the NEG coated vacuum chambers needed for LHC a dedicated facility was built at CERN. It consists in three cylindrical magnetron sputtering systems, which allow coating vacuum chambers with different diameters, lengths and geometries. The cathodes were composed of three inter-twisted wires of $Ti$, $Zr$ and $V$ with the same diameter; this configuration was chosen instead of a single cathode of the desired alloy composition since it is much cheaper than it. If a simple cylindrical geometry had to be

coated a single cathode was used, meanwhile for more complex geometries (like elliptical chambers or converging pipes) more than one cathode was needed.
In order to realize a lasting NEG film it was mandatory to chemically treating the internal walls of the vacuum chambers that have to be coated; in fact, without an adequate surface treatment the films ruin themselves and it can happen that they peel-off.

The coating facility assured an average production rate of 20 chambers per week, demonstrating that NEG coated vacuum chambers can be produced on a large scale. In **Figures 1.7** a pictures of the LHC beam pipes ready of the installation is reported; the chambers are made of OFS copper with welded 316LN stainless steel flanges.

FIGURE 1.7: A stock of NEG coated vacuum chamber ready to be installed in the LHC tunnel.

In **Table 1.2** the main coating parameters used for the 1200 long straight sections beam pipes are reported.

TABLE 1.2: Main coating parameters used for the realization of the LSSs LHC beam pipes.

| | |
|---|---|
| Discharge Gas | $Kr$ |
| Gas Pressure | $10^{-2}\ Torr$ |
| Magnetic Field | $3 \cdot 10^{-2}\ T$ |
| Ion Current Density | $6 \cdot 10^{-2} \div 1,9 \cdot 10^{-2}\ Am^{-1}$ |
| Cathode Potential | $-500\ V$ |
| Cathode Power | $1,5\ kW$ (DC) |
| Chamber Coating Temperature | 100 °C |

To ensure the quality of the production after every run characterization measurements were performed on a copper sample coated simultaneously with one of the chambers: the

elemental composition was checked by EDS, the coating thickness was measured with SEM and the activation behavior was tested with XPS. The pumping speed performance of the NEG film were checked too.

## 1.5 Purpose of this study

The present study could be divided into two different parts: the first one linked to issues related to LHC, the second is continuation of the NEG material study began in 1995 and temporarily stopped when a composition with good pumping properties and activation temperature compatible with the bake-out temperatures of the most common vacuum chamber structural materials was found: $Ti_{30}Zr_{30}V_{40}$ .

The NEG coated vacuum chambers already installed in many accelerators and synchrotron facilities may be subject of maintenance. In the LHC, for example, a Long Shutdown (LS1) ended in June 2014 and others are planned in order to high the machine luminosity. Since LS1 the NEG re-activation, after the exposure to the LHC atmosphere, presented problems in some cases, it has been decided to study in details if the exposure to tunnel atmosphere for long periods may affect the pumping properties of a NEG coated vacuum chamber. An ageing campaign has, therefore, been planned: knowing in advance how to behave in front of the opening of NEG coated vacuum chamber is desirable in order to avoid additional cost due to bad maintenance (coating again a damaged vacuum chamber costs). In the present work the results obtained so far will be presented in details.

After the application in the LHC, the NEG materials obtained the attention of the scientific world, since it was clear that they are the solution for most of the ultra high vacuum issues. Systematic studies of their properties are needed in order to provide a better understanding of the activation mechanism; it could allow us to find out rules for the selection of new alloys, maybe with lower activation temperature and better pumping properties.
In this work the results obtained testing three different types of NEG materials are presented: $ZrV$, $HfV$ and $TiZrHfV$. They have been chosen considering the results obtained for $TiZrV$ alloys; for them the presence of vanadium is needed in order to decrease the film grain dimension. This parameter is linked for $TiZrV$ to the activation temperature: nano-crystalline films have low activation temperature. The aim of the coating campaign is, therefore, to check if vanadium has the same effects on the remaining materials of the $IV$ group, zirconium and hafnium. $TiV$ alloys have not been tested since CERN previous works indicate that they do not own good vacuum properties. Moreover, a quaternary alloy composed by all the $IV$ group elements with the adding

of vanadium has been studied too. Not ably the activation process has been studied, but also the pumping performance; it is expected that they are linked to the surface morphology, as for $TiZrV$. Pumping speed and sticking probability measurements have been performed and the surface samples structures have been observed using SEM.

# Chapter 2

# General Properties of Non-Evaporable Getter Thin Films

## 2.1 General Considerations

The Non-Evaporable Getter materials are capture pumps, which means materials able to remove molecules from the gas phase by fixing them into an internal surface.
Capture pumps are usually characterized by a sojourn time, define as the time spent by a captured molecule on the surface of the pump:

$$\tau = \tau_0 exp\left\{\frac{BE}{k_B T}\right\},$$

where $\tau_0$ is a constant and $BE$ is the molecules binding energy on the material surface. It is needed that the sojourn time is long enough to guarantee that the molecules are sticked on the material surface for whole duration of the experiments.
Getters are materials able to chemically react with the most of the gases present in a vacuum system; they form with them stable chemical compounds at room temperature. Because of the binding energy is so high, they have a sojourn time suitable for vacuum application.

In order to allow the reaction between the surface particles of the getters and the gases in the vacuum chamber, the surface must be free of contamination and free of the native oxide layer. This layer is due to the air exposition and for a NEG material is eliminated by heating in situ the surface; this procedure, called activation, allows the diffusion of the oxygen into the bulk of the material leaving a very reactive and clean surface.

The dissolution of the native oxide layer (oxygen reduction reaction) is possible only if the transfer of oxygen in the solid solution[1] is thermodynamically allowed and the oxygen diffusion rate in the film is sufficiently fast (temperature dependence of both the process)[11].
The oxygen reduction in the NEG material takes place at constant pressure and temperature, therefore it can be studied using the Gibbs free energy variation[5].

$$\Delta G_{ox} = \Delta H_{ox} - T\Delta S_{ox}; \tag{2.1}$$

$$\Delta G_{ss} = \Delta H_{ss} - T\Delta S_{ss}; \tag{2.2}$$

where **Eq. 2.1** defines the variation of the Gibbs free energy during the oxide formation, meanwhile **Eq. 2.2** the one for the solid solution.
The oxygen dissolution into the bulk is allowed when the total variation of the Gibbs free energy is negative:

$$\Delta G_{tot} = \Delta G_{ss} - \Delta G_{ox} < 0;$$

$$\Delta H_{ss} - \Delta H_{ox} < T(\Delta S_{ss} - \Delta S_{ox}). \tag{2.3}$$

Since the entropic term is alway negative, the reaction can take place in two different occasions:

1. $$\Delta H_{ss} > \Delta H_{ox} :$$

   this is the case of the $IV$ group metals $Ti$, $Zr$ and $Hf$, for whom the reaction is, therefore, allowed at all temperatures;

2. $$\Delta H_{ss} < \Delta H_{ox} :$$

   temperatures exist for whom the entropic term is higher than the enthalpic one, therefore the reaction as a threshold temperature. This is the case of $V$ group metal $V$, $Nb$ and $Ta$.

For application also reaction kinetics aspects should be studied; therefore diffusivity and solubility limit have to be taken into account.
The diffusivity takes into account how fast is the oxygen diffusion from the surface to the bulk of the material, since it is the proportionality constant between the flux due to the molecular diffusion and the concentration of the species gradient, which is the

[1] A solid solution is a solid-state mixture of one or more solutes in a solvant. It is not considered a compound when the crystal structure of the solvant remain unchanged by the addition of the solutes and when this mixture remains in a homogeneous phase.

driving force of a mass diffusion process. In the case of solid materials the temperature dependence of this coefficient can be very well described by the Arrhenius equation:

$$D(T) = D_i exp\Big\{-\frac{E_i}{RT}\Big\},$$

where $D_i$ $[m \cdot s^{-1}]$ is the maximum diffusion coefficient and $E_i$ $[J \cdot mol^{-1}]$ the activation energy for the diffusion of the element $i$.
In case of getter material is of great importance the diffusivity for oxygen, since it determines how fast is the activation process, and the diffusivity of hydrogen, nitrogen and carbon, because they are the main elements that a NEG thin film has to pump in a vacuum chamber.
An interesting parameter, strictly linked with the diffusivity, is the diffusion length, which provides a measure of how far the concentration has propagated in a certain direction in a certain amount of time:

$$L = \sqrt{D(T) \cdot t}. \tag{2.4}$$

The diffusion length can be used to evaluate when the grain boundaries play an important role in the oxygen diffusion process. Called $\omega$ the grain size, there are two possible situations:

- when $L < \omega$ the diffusion occurs at the grain boundaries but also within the grains;
- when $L > \omega$ the diffusion occurs mainly at the grain boundaries.

The solubility limit, $x_0$, is defined as the equilibrium concentration of the element $i$ in the solid solution; it is thus calculated when the Gibbs free energy for the oxide formation is equal to the one of the solid solution: $\Delta G_{ox} = \Delta G_{ss}$. This parameter takes into account the amount of moles of a solute that a solvent can hold.
In **Table 2.1** the values of the diffusion length and solubility limit for some interesting elements are reported. The reported data refer to the case of a single crystal. It must

TABLE 2.1: Numerical values of the diffusion length (L) for oxygen for 2 $h$ of heating at 300 °C and of the oxygen solubility limit at 300 °C [5].

| | *IV* Group | | | *V* Group | | |
|---|---|---|---|---|---|---|
| | Ti | Zr | Hf | V | Nb | Ta |
| L $[nm]$ | 0,4 | 0,9 | 0,1 | 300 | 650 | 800 |
| $x_0$ | 35 | 29 | 17 | 5 | 0,01 | 0,4 |

be noted that both the parameters increase in the presence of poly-crystals[2].

[2]Poly-crystals are material composed by a huge number of single crystals hold together by amorphous solid.

The diffusion length and the solubility limit differences between the metals of the $IV$ and $V$ groups are due to the different crystal lattices. $Ti$, $Zr$ and $Hf$ own a hexagonal close-packed (hcp) crystalline structure which being dense does not promote the diffusion into the bulk, but has a huge oxygen storage capacity; the contrary can be said for the body-centered cubic (bcc) lattice of the $V$ group elements.

## 2.2 Selection of Getter Materials

Considering what has been said in **Section 2.1**, among all the materials those suitable for becoming a getter are the metals of the periodic table transition group. The key parameters for the choice of NEG materials are[2]:

- large enthalpies of adsorption for all the gases which are usually present inside vacuum system (i.e. $H_2$, $CO$, $CO_2$ and $N_2$);
- hydride phase with low dissociation pressure, in order to ensure pumping capacity for $H_2$ at room temperature and under UHV
- diffusivity for $O_2$, required to guarantee a low activation temperature;
- solubility limit for $O_2$, to allow many activation-air exposure cycles.

Other essential features which the getter material should also provide are:

- good adhesion to the substrate;
- high mechanical resistance;
- high melting point.

In he case of coatings for use in particle accelerators the material should be non-magnetic and present a low photoelectric secondary yield to reduce electron emission and avoid multipactoring.

The element of the $IV$ group ($Ti$, $Zr$ and $Hf$) fulfill all these requirements; in particular, they show an exceptionally high ability to dissolve oxygen attaining values of concentration up to 30 at. % (a solubility limit of at least 10 at. % is desirable); in the nearby groups the solubility limit drops to values below 1 at. % at temperatures lower than 400 °C (except for $V$ and $Sc$). Meanwhile they have a low diffusivity due to their lattice.

In 1996 single wires of these elements have been used as a starting point for the NEG coating feasibility campaign. DN100 stainless steel tube were coated using magnetron sputtering (see **Chapter 3.2.1**), then tested in order to characterize their vacuum properties. In **Figure 2.1(a)** the results of the Electron Stimulated Desorption measure-

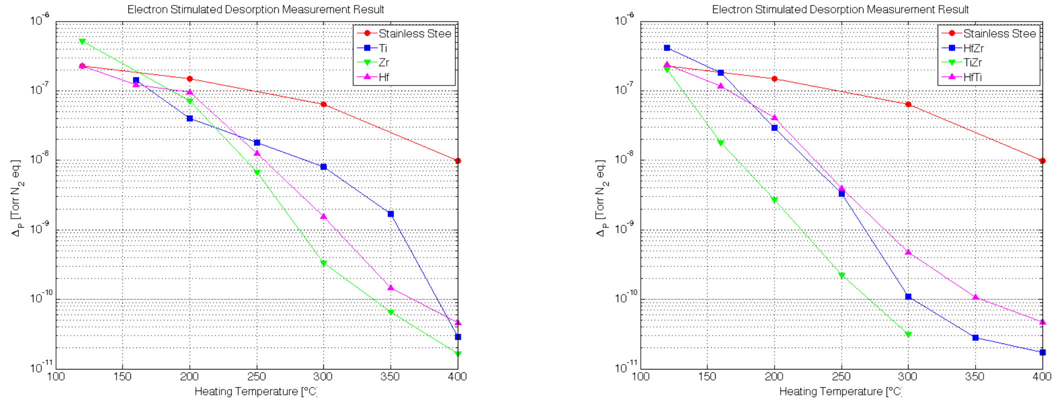


(a) $IV$ group elements[17].

(b) $IV$ group binary alloys[2].

FIGURE 2.1: Results of the ESD measurements performed with an applied voltage of 500 $V$ and a current through the electron source of 1 $mA$.

ments (ESD, see **Section 3.3.2**) for the $IV$ group elements are reported. It can be seen that the samples with the inner walls coated with $IV$ group elements have a much higher drop in the pressure after the electron bombardment in respect of the bare stainless steel sample. $Hf$ and $Zr$ are poorer at the beginning but then the activation process begins at lower temperature, around 200 °C, while for $Ti$ is around 300 °C. These two elements are, therefore, adequate for coating stainless steel chamber, but are completely useless if the a baking temperature of 200 °C cannot be exceeded, as the case of copper of aluminum alloys vacuum chambers.

Stainless steel samples coated with quasi-equiatomic binary alloys of the $IV$ group elements were produced and tested too. Instead of the using single rod of the alloys wanted to be sputtered, the cathodes were braids composed of single elements wires (see **Figure 3.7**). This kind of cathodes are less expensive and easier to produce than a single alloy rod, but the coating composition can be changed only in a discontinuous way by changing the wires diameters.

In **Figure 2.1(b)** are reported the ESD measurements results, from which it can be seen that the alloys display, in general, a lower activation temperature, the lowest being that of $TiZr$. The binary alloys of these two elements were studied in details[17]. The coatings of variable composition were obtained by twisting together wires of different diameter; the real alloy compositions were checked after the coating by means of EDS measurements (see **Section 3.3.4**). The lowest activation temperature was measured

for equiatomic $TiZr$ compounds; it is about 250 °C for 2 $h$ heating and about 200 °C if the heating is extended to 24 $h$[17].

As already said in the previous section, the elements of the $V$ group present a much higher oxygen diffusivity than $IV$ group elements. Since this parameter is fundamental for guaranteeing a low activation temperature, these elements were studied too. The ESD results are reported in **Figure 2.2** The differences in pressure reached are not as

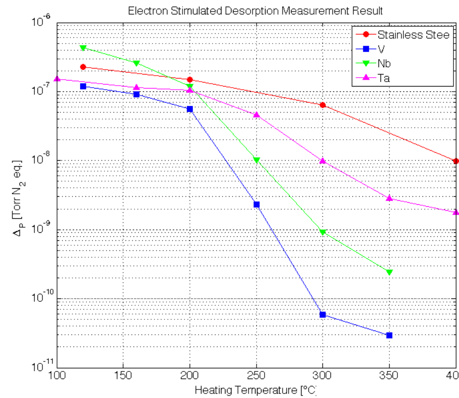


FIGURE 2.2: Results of the ESD measurements for the $V$ group elements, performed with an applied voltage of 500 $V$ and a current through the electron source of 1 $mA$.

good as the ones of the $IV$ group elements, except for Vanadium. Therefore, it was thought in 1997 to add a wire of $V$ to the $TiZr$ braid; this addition may both enlarge the lattice space, with an increase in the bulk diffusivity, or may reduce the grain size, increasing the transport of oxygen through the grain boundaries. The first $TiZrV$ film analyzed was realized with 1 $mm$ of each elements and the results indicated that the research was going in the right direction.

In **Figure 2.3** a comparison between bare stainless steel, $TiZr$ and $TiZrV$ is shown; it can be noticed that the two coated stainless steel samples behave in the same way at the beginning and at the end of the activation cycle, whereas the $TiZrV$ coating has better pumping properties between 160 °C and 200 °C. Moreover the degassing minimum is reached already at 250 °C.

Since activation is completed when the oxygen surface content reaches a minimum, surface analyses were performed in order to conform the good results obtained by ESD. **Figure 2.4(a)** shows a comparison between the $Zr$ 3$d$ doublet for $TiZr$ (spectrum b) and $TiZrV$ (spectrum c) after the same heating cycle: 2 $h$ at 250 °C. Spectrum c correspond to the as-received $TiZr$ sample. Comparing spectra a and b it can be immediately noticed the shift at lower binding energy in the $Zr$ 3$d$ peaks, which indicates the $Zr$ reduction. This effect is more pronounced for the $TiZrV$ film (spectrum b), proving direct evidence if its lower activation temperature. In **Figure 2.4(b)** the reduction of the $V$ 2$p$ doublet for the $TiZrV$ film is shown. The presence of oxygen on the sample

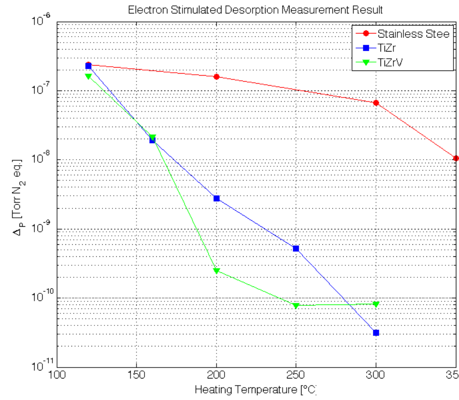


FIGURE 2.3: Comparison between the ESD results for Stainless Steel, $TiZr$ and $TiZrV$, performed with an applied voltage of 500 $V$ and a current through the electron source of 1 $mA$[2].

surface is visible only in the spectrum a: the disappearance of this peak after 2 $h$ of heating at 250 °C indicates that the oxygen diffuses into the bulk and can be considered a prove of the sample activation.

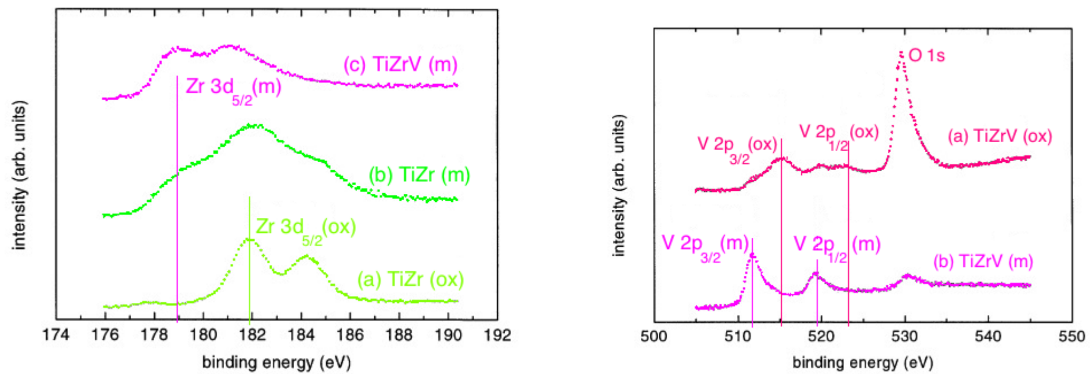


(a) XPS spectra of oxidized $TiZr$ (a), metallic $TiZr$ (b) and metallic $TiZrV$ (c).

(b) XPS spectra of oxidized $TiZrV$ (a) and metallic $TiZrV$ (b).

FIGURE 2.4: XPS measurements performed with a SPECS EA10P hemispherical analyzer using a non-monochromatic $Al\ K_\alpha$ radiation as excitation source[2].

This results suggest that this kind of ternary alloys, $TiZrV$, have a lower activation temperature then the binary alloys of $TiZr$, therefore it was decided to full characterized them before starting the testing other alloys.
In the following of the section are reported the main results obtained for $TiZrV$ alloys, which led to the optimization of them for applications in particles accelerators. In particular, it has been proved that the full activation of $Ti_{30}Zr_{30}V_{40}$ can be obtained after 24 $h$ of baking at 180 °C[4]. As it can be seen from **Figure 2.5** the pressure inside the chamber reaches its minimum at 180 °C: increasing further the baking temperature does not change the pressure, which it means that the activation is fully completed at

180 °C. This result makes the *in-situ* activation of $TiZrV$ film compatible with all the substrate materials used in vacuum technology.

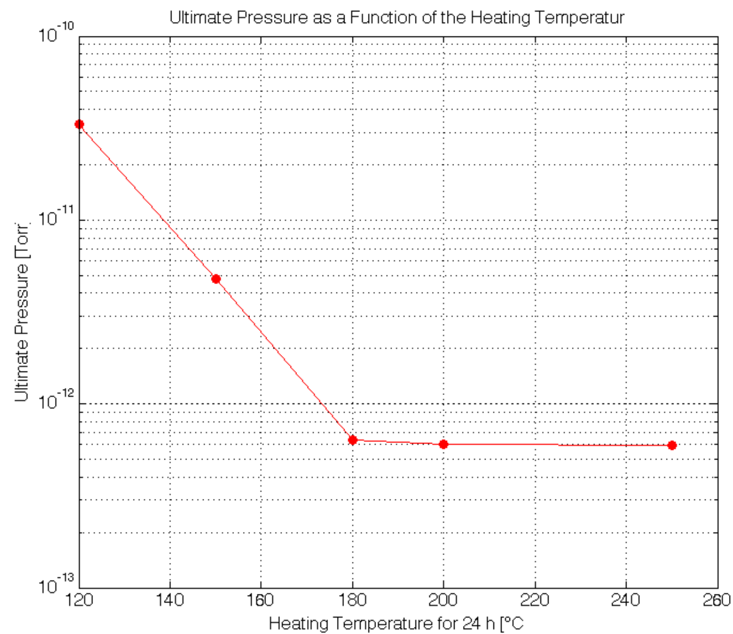


FIGURE 2.5: Ultimate pressure as a function of the heating temperature for a 50 $mm$ inner diameter chamber coated with $Ti_{30}Zr_{20}V_{50}$.

## 2.3 General Properties of $TiZrV$ films

Detailed studies of $TiZrV$ alloys have been made to understand their vacuum properties and to improve them. Different samples were prepared using magnetron sputtering coating techniques with inter-twisted cathodes. The effects on the thin films microscopic characteristics provoked by the changing of the following parameters were studied:

- elemental atomic percentage in the alloy;
- substrate material;
- substrate temperature during the coating;
- substrate surface treatment before the coating;
- discharge gas used for the coating.

In the following the effects related to the variation of these parameters are going to be discussed in details.

The concentration of the three elements inside the film can be varied changing the diameter and the number of wires in the cathode used for the sputtering (see **Section 3.2.2** for more details). It has been proved that the alloy composition affect the activation temperature of the NEG film[3]. In order to check the activation behavior samples deposited on stainless steel 316 LN have been analyzed using Auger Electron Spectroscopy (AES). It has been decided that a good indicator for the activation is the changing in the MNV Auger peak of $Zr$ after heating at different temperature, since the metallic $Zr$ (at 147 $eV$) peak increases while the oxidized $Zr$ peak (141 $eV$) decreased with the increasing of the temperature. Two samples reach the same level of activation when their relative increase of these peaks are the same. $R$ is called the ration between the intensity of these two peaks and is a parameter that allows the classification of the samples into two categories: sample with low activation temperature (red dots in **Figure 2.6(a)**) and samples with high activation temperature (blu dots in **Figure 2.6(a)**).

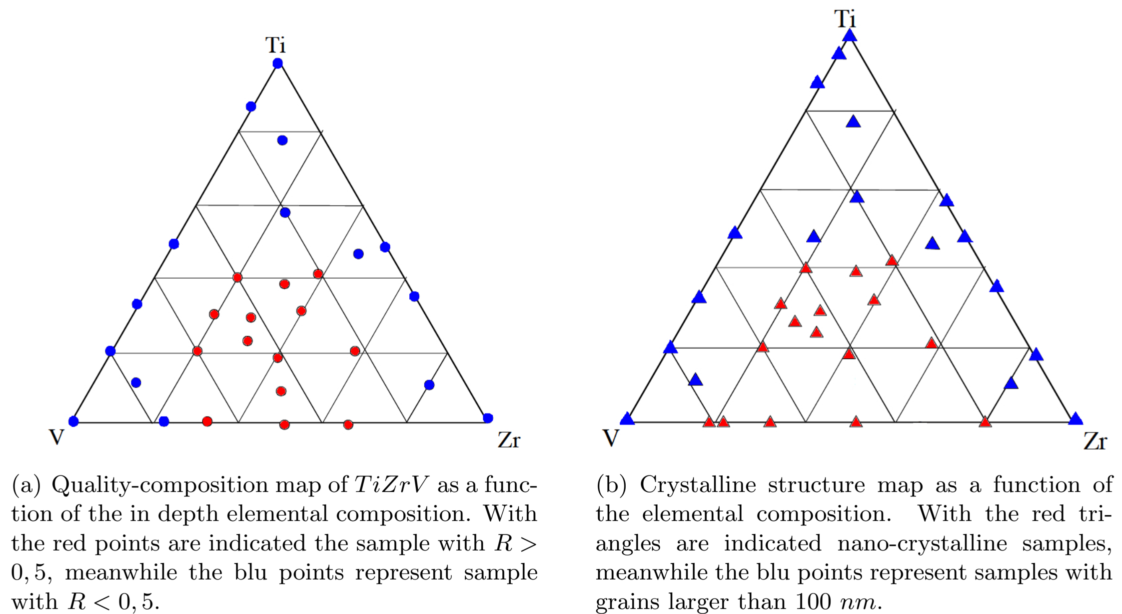


(a) Quality-composition map of $TiZrV$ as a function of the in depth elemental composition. With the red points are indicated the sample with $R > 0,5$, meanwhile the blu points represent sample with $R < 0,5$.

(b) Crystalline structure map as a function of the elemental composition. With the red triangles are indicated nano-crystalline samples, meanwhile the blu points represent samples with grains larger than 100 $nm$.

FIGURE 2.6: Composition maps for $TiZrV$ thin films[3].

Looking at **Figure 2.6(b)**, it seems that a ternary alloy is necessary in order to obtain film with small grain sizes[3]. XRD measurements suggest that films nanocrystal morphology is affected by the concentration of the three elements: films with a low atomic percentage of $Ti$ and an almost equal percentage of $Zr$ and $V$ (central area of **Figure 2.6(b)**) present grain sizes smaller than 5 $nm$. It seems to be likely that nanocrystal samples represent a metastable phase due to their deposition by sputtering, since the alloy phase diagram at room temperature predicts the existence of two phase [5]: a bcc $\beta$-phase containing $Ti$, $Zr$ and $V$ and a bcc $\delta$-phase containing $Zr$ dissolved in $V$.
Comparing **Figure 2.6(a)** and **Figure 2.6(b)** a clear connect between composition,

nano-crystallinity and activation temperature can be noticed: samples with low activation temperature are ternary nanocrystal film of $TiZrV$. The decrease of the activation temperature is due to the vanadium addition; thanks to this element the film grains are smaller, therefore there are a lot of grain boundaries where the diffusion process can take place at room temperature. A noteworthy exception are the equi-atomic film of $ZrV$, which are discussed in details in **Chaper 4**.
For large scale applications, it is important to point out that the composition of the film is not a critical parameter to control during deposition, since films with a low activation temperature can be obtain in a wide range of composition. This characteristic of $TiZrV$ makes it suitable for industrial application where a high precision on the film composition cannot be obtained easily.

The effects of the coating parameters on the vacuum performances of the $TiZrV$ thin film coatings have been studied, in order to optimize the coating parameters.
Roughness and porosity are fundamental characteristics of a NEG thin film. It has been found that they not only depend on the substrate but also on the coating parameter, in particular on the substrate coating temperature. In **Figure 2.7** are shown SEM imagines of the $TiZrV$ coating surface in case of deposition of stainless steel (**Figure 2.7(a)**) and aluminum (**Figure 2.7(b)**). It can be noticed an appreciable increase in the surface roughness in the case of deposition on aluminum in respect to the deposition on stainless steel.

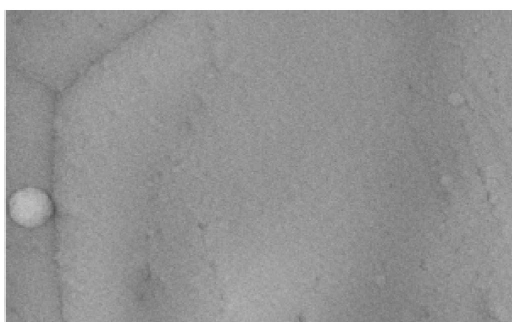

(a) SEM imagines of the $TiZrV$ deposited on stainless steel.

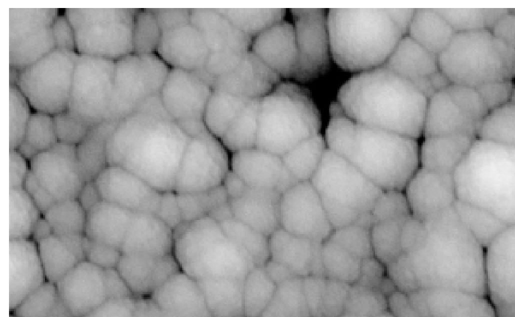

(b) SEM imagines of the $TiZrV$ deposited on aluminum

Figure 2.7: Influence of the substrate nature on the coating roughness[4].

The roughness can be also enhanced increasing the temperature at which the substrate is kept during the sputtering procedure, as can be seen in **Figure 2.8**. Meanwhile, SEM imagines of the $TiZrV$ coating profile show that the for the same substrate temperature and material the roughness can be increased using a substrate chemically treated before the coating. It can be concluded that the morphology of the film may be controlled to a large extent.

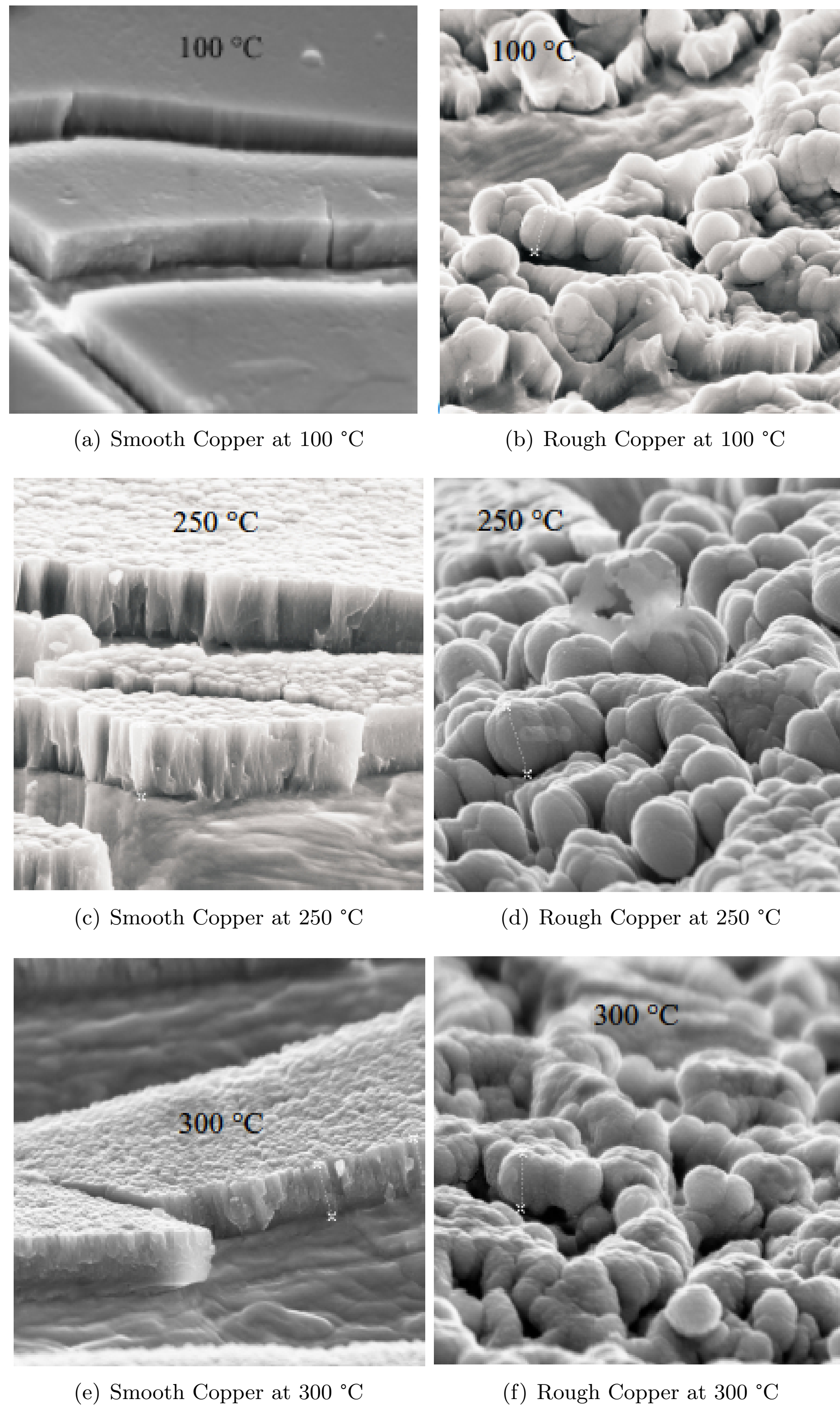


(a) Smooth Copper at 100 °C (b) Rough Copper at 100 °C

(c) Smooth Copper at 250 °C (d) Rough Copper at 250 °C

(e) Smooth Copper at 300 °C (f) Rough Copper at 300 °C

FIGURE 2.8: SEM imagines of $TiZrV$ thin film sputtered on different type of copper substrates; all the films in the left column are deposited on smooth copper, meanwhile the ones in the right on rough copper [5].

Kripton has been chosen as the discharge gas during the sputtering procedure, since it reduces the gas released during the operating cycle[18]. During the sputter procedure

used for deposited in UHV metallic thin film the energetic discharge gas neutrals may be implanted in the growing film and released after. Since rare gases are not pumped by NEG materials, the release have to be minimize to not spoil the vacuum obtained in the coated chambers. In first approximation the gas trapping depends on the momentum exchanged at cathode impact (when the discharge gas may bounces back toward the substrate with enough energy to be implanted) and in the film crystal structure. It has been proved that in case of $TiZrV$ coating produced by magnetron sputtering an $Ar$ content of about 3500 $ppm$ has been measured, meanwhile the content of $Kr$ is two orders of magnitude lower[18].

## 2.4 Vacuum Properties of $TiZrV$ films

The vacuum performance of a getter after the activation can be evaluated using the following parameters:

- pumping speed, $S$ in $[l \cdot s^{-1}]$, or sticking probability, $\alpha$;
- surface capacity, $Q$ in number of particles or $[Torr \cdot l]$;
- ultimate pressure, $p$ in $[Torr]$.

In case of applications in particles accelerators, other important parameters, which should be studied, are:

- induced desorption;
- secondary electron yield;
- performance deterioration (ageing).

In the following all these parameters are going to be discussed in details.

The pumping speed can be defined as the derivative of the pump throughput (pumped gas flow), $Q_p$, with respect to the pump inlet pressure, $p$:

$$S = \frac{\partial Q_p}{\partial p}. \tag{2.5}$$

The sticking probability, $\alpha$, is defined as the ratio between the rate of chemically adsorbed molecules and the total rate of molecules incident on the surface[11]. It is a very important parameter for a pump because it is not related to the pump geometry,

therefore it can be used to compare the performances of different kind of pumps.
The pumping speed and the sticking probability are linked by the following relation:

$$S = \alpha \cdot C, \tag{2.6}$$

where $C$ is the conductance in $[ls^{-1}cm^{-2}]$[19].
NEG materials present a pumping speed for the gases present in UHV systems ($H_2$, $CO$, $CO_2$, $H_2O$, $N_2$ and $O_2$), except for noble gases. This is due to the fact that this type of gases do not chemically react with other elements. A negligible pumping speed is also provided for $CH_4$, because of the high dissociation energy of this molecules at metal surfaces. The sticking probability depends on the gas species, on the surface

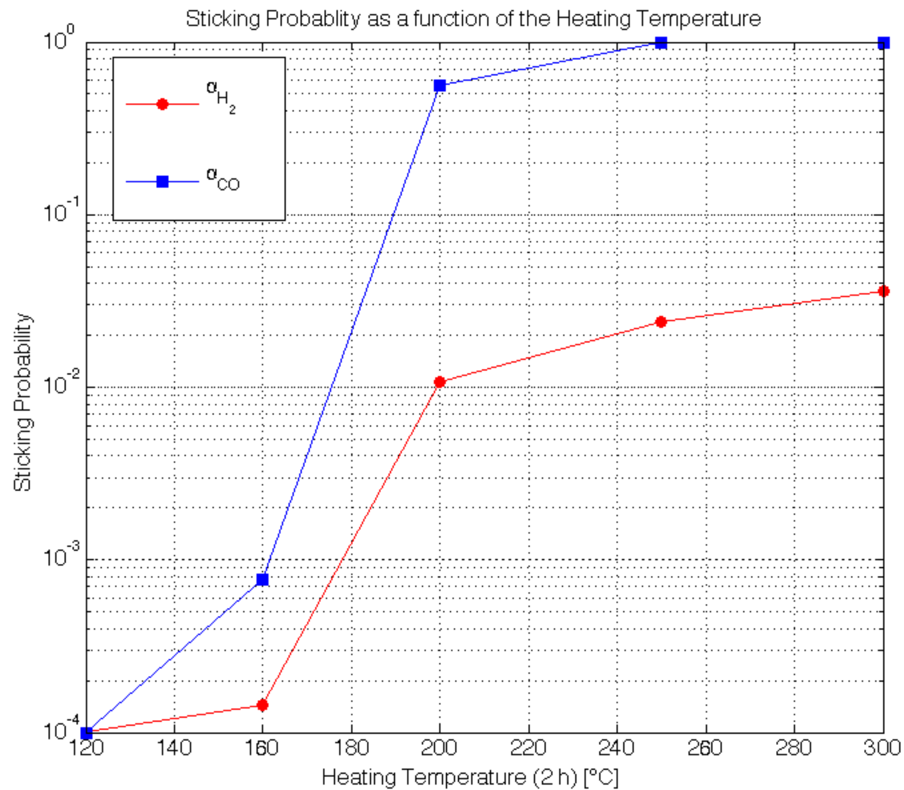


FIGURE 2.9: Sticking probability for $H_2$ (red points) and $CO$ (blue points) as a function of the heating temperature. The measurements are performed after two hour of heating at different temperatures (see **Chapter 3** for the measurement procedure).

coverage and on the film surface roughness. In **Figure 2.9** the behavior of the sticking probability for $H_2$ and $CO$ with the activation temperature is shown. The sticking probability increases with the activation temperature until the film full activation is reached. For all the heating temperature the $H_2$ sticking probability is about two order of magnitude lower that the one for $CO$; this behavior can be explained considering that two adsorbing sites are need for the sticking of $H_2$ and one for $CO$ (the probability of

finding two close adsorbing site is low).
The pumping speed of all the gases decrease as the coverage of the same gas increases; the only exception is $H_2$ since it can diffuse at room temperature into the bulk material after being pumped leaving the surface free of capture another molecule. This is also the reason why the presence of $H_2$ does not influence the pumping of another gas, meanwhile the presence of other gases influence the film pumping speed for other gas[20], since they remain stick on the surface instead of diffusing into the bulk.

In the previous section it has been discussed the possibility of enhance the surface roughness of the NEG thin film increasing the roughness of the substrate and the coating temperature. This parameter is strictly linked with the vacuum performances of the films since it affects both the surface gas capacity (larger surface area) and the the sticking probability (possibility of multiple collisions of the impinging molecules inside the surface); therefore a high surface roughness is desirable. However, it must be taken into account that film sputtered at 300 °C (very rough film) have large grain sizes, therefore high activation temperature, and also that roughness implies larger quantity of oxygen adsorbed during the air venting (worsening of the performances as a function of the air-venting/activation cycles)[21]. Therefore, a low coating temperature (100 °C) is preferred if the sputtered film is meant to be vented and activated a lot of times.

The ultimate pressure is the lower total pressure that can be produced and measured reproducibly at room temperature after baking in a vacuum system[22]. It has been proved that no intrinsic limitations of the ultimate pressure for a NEG coated vacuum chamber exists[23]; the lowest pressure measured is around $10^{-13}$ $Torr$ and it is an instrumental artefact due to the measuring gauge degassing.
The film characteristic which can limit the ultimate pressure is the outgassing of discharge gas and $CH_4$, gases not pumped by the film. Both these characteristics do not affect the reachable pressure, since the $Kr$ outgassing is negligible at all the interesting temperatures and the $CH_4$ outgassed by the vacuum chambers materials can be pumped with an auxiliary pump with a very low $CH_4$ pumping speed because of the low outgassing rate for this gas.

It has already been said that in case of particle accelerators applications a fundamental characteristic of the NEG thin film coating is the low induced desorption yield. In fact, in case of particle accelerators there are two sources of gases: the thermal outgassing and the desorption induced by the beam particles bombardment (photons, electrons and ions). In both case the source of the gas load may be the oxide layer. Since an activated NEG thin film coating lacks of this layer, it is expected that the desorption yield is lower than the one of a non coated chamber. This expectation is confirmed by

the experimental results: the measured electron desorption yield for $H_2$ and $CO$ is at least 10 times lower than those for stainless steel.

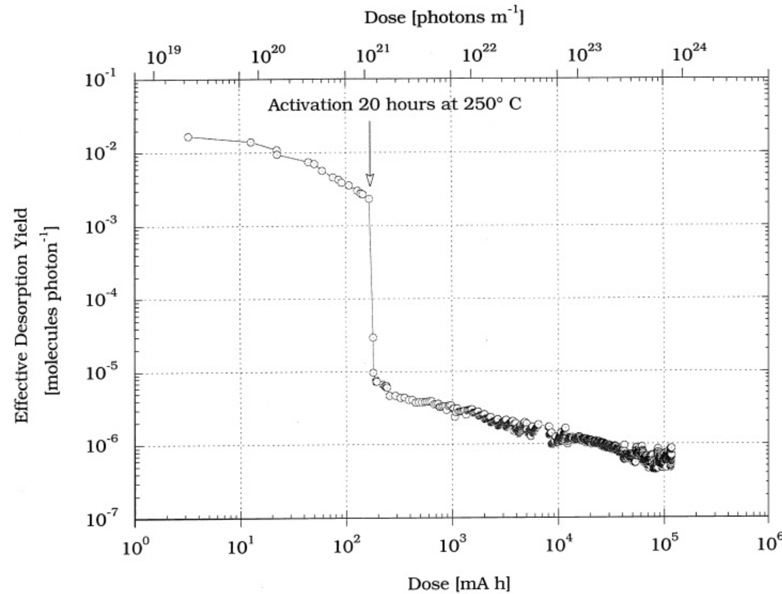


Figure 2.10: Variation of the effective molecular desorption yield as a function of the beam and photon dose measured on a $TiZrV$ coated stainless steel vacuum chamber installed on a beam line at ESRF (Grenoble)[6].

The low Secondary Electron Yield (SEY) of NEG thin films is one of their advantages since it reduces the risk of resonant electron multiplication (multipacting). In particular, a positive feedback process may rise if the SEY and the frequency of the accelerated particle bunches are higher than a well defined threshold. Multipacting has to be avoided in accelerators because it provokes localized pressure bumps which are detrimental for the beam life time, luminosity and thermal load. As can be seen in **Figure 2.10** an activated NEG coating may considerably reduce the chamber SEY. This reduction is expected since, as the case of induced desorption, the source of the secondary electrons is the oxide layer, which is dissolved into the bulk material after the activation[6].

In several application the NEG thin film coating may be subjected to many venting-activation cycles with a consequent deterioration of its pumping properties. This worsening is due to the fact that during the activation procedure the oxygen, which during the air exposure remains sticked on the film surface, is dissolved into the bulk. Since the film has a thickness in the range of nanometers, each venting-activation cycles increase in a non-negligible way the film oxygen concentration. Ageing test have been performed in a $TiZrV$ coated vacuum chamber[4]. The variation of the sticking probability after each venting-activation cycle has been monitored, proving that the deterioration of the

pumping properties of the film may be counteracted by increasing the activation temperature after each air exposure.

In conclusion it can be said that NEG thin films not only are suitable for applications in particle accelerators, but also present many advantages in respect to the standard vacuum chambers design; the first and most important is that they transform the internal surface of a vacuum chamber from a gas source into a pump, allowing to reach the extreme UHV condition requested by the modern accelerators.

# Chapter 3

# Experimental Set-Up Characterization Methods

In this chapter the experimental set-ups of all the machine used is described together with the characterization measurements performed on all the sample tested. In particular **Section 3.1** is dedicated to the description of the experimental set-up and of the measurements procedure used for testing the ageing campaign samples. Meanwhile **Sections 3.2** and **3.3** describe the preparation and the characterization of the samples tested in the coating campaign.

## 3.1 Pumping Speed Measurement

In the following section the pumping speed measurement are described in details. A brief introduction about the vacuum system, given in order to better understand how to measure the pumping speed a pumping speed, is followed by the description of the Fischer-Mommsen dome, which is the standard system for measuring the pumping speed. In the end of the section the system used for the measurements is described in details, together with the measure procedure.

### 3.1.1 Vacuum System Characteristic Quantities

The gas inside a vacuum system is rarefied gas in equilibrium, which can be described as an ideal gas: a set of randomly moving, non interacting point particles[24].

The classical ideal gas equation of state allows to obtain all the thermodynamic properties of the system. This equation can be written as follows:

$$PV = Nk_BT, \tag{3.1}$$

where $P$ is the gas pressure, $V$ is the gas volume, $N$ is the number of molecules, $k_B$ is the Boltzmann constant $(1,3810^{-23}\ JK^{-1})$ and $T$ is the gas temperature.
The kinetic of a classical ideal gas is described by the Maxwell-Boltzmann distribution function:

$$f(v)dv = 4\pi\left(\frac{m}{2\pi k_BT}\right)^{(3/2)} v^2 \exp\left\{\frac{mv^2}{2k_BT}\right\}dv, \tag{3.2}$$

where $f(v)dv$ is the probability of finding a particle whose velocity is included between $v$ and $v + dv$.
This distribution function allows to calculate some important quantities for vacuum systems. One of these quantities is the molecules mean velocity of the ideal gas; it can be calculated as the first momentum of the Maxwell-Boltzmann distribution function:

$$< v >= \int_{-\infty}^{+\infty} vf(v)dv = \left(\frac{8k_BT}{\pi m}\right)^{(1/2)} = \left(\frac{8k_BT}{\pi m}\right)^{(1/2)}. \tag{3.3}$$

where $m$ the mass of the molecule.
Another interesting quantity is the rate at which the molecules of an ideal gas hit a unit surface area exposed to the ideal gas: molecular impingement rate $(m^{-2}s^{-1})$. In the hypothesis of a uniform density of molecules in the volume of the vacuum system it can be shown [1] that the molecular impingement rate has the following expression:

$$\phi = \frac{1}{4}n < v >= \frac{1}{4}n\left(\frac{8k_BT}{\pi m}\right)^{(1/2)}, \tag{3.4}$$

where $n$ is the density of molecules inside the vacuum system and the last equality has been obtained substituting into **Eq. 3.4** the expression for the mean velocity (**Eq. 3.3**).

The flow dynamics inside the vacuum system is determinated by the type of interaction affecting the molecules of the ideal gas[22]. During their motion inside the vessel they can interact both with other molecules and the walls of the vacuum vessel. We can characterize the type of motion in the vacuum system introducing the characteristic length for the molecules interactions; this length is called *mean free path*, $\bar{\lambda}$ and is defined as the mean distance travelled by a molecule before interaction with another molecule. This parameter is inversely proportional to the density of the molecules and

[1] We can obtain the molecular impingement rate in **Eq. 3.4** if the molecular flux across a plane surface element is given by the cosine law formula

the cross section of the collision:

$$\bar{\lambda} = \frac{1}{\sqrt{2}n\sigma_c}. \tag{3.5}$$

We can distinguish three types of dynamics inside the vacuum system comparing the molecules mean free path with the characteristic dimension of the system. When the mean free path is greater then the system characteristic dimension we are allowed to neglect the collision between molecules in the description of the flow dynamics, otherwise we have to take into account collisions between molecules.

The *Knudsen number* is a parameter allowing us to quantify these considerations. It is define as the ration between the ration between the mean free path and the characteristic dimension:

$$K_n = \frac{\bar{\lambda}}{d}. \tag{3.6}$$

As we have just pointed out, we can distinguish three different situations:

- if $K_n > 0,5$, then the mean free path is big enough to neglect the collision between molecules. We call this kind of dynamics *molecular flow*;
- if $K_n < 0,01$, then the collision between molecules are important in the description of the dynamics. This regime is called *viscous flow*;
- if $0,01 \leqslant K_n \leqslant 0,5$, then the regime is called *transitional flow.*

Considering the thermodynamics properties and the dimension of a typical vacuum system we often deal with ideal gas in the molecular flow regime.

In many situation it is of fundamental importance knowing the net gas flow, i.e. the quantity of gas molecules flowing from a point to another in the vacuum system. In molecular flow regime it (in the SI units $Pam^3s^{-1}$), $Q$, is proportional to the pressure difference between the two points considered:

$$\dot{Q} = C(P_1 - P_2), \tag{3.7}$$

where $C$ is the proportionality constant, called gas conductance (usually expressed in $ls^{-1}$).

The conductance can be determined very easily in the case of the simple geometry shown in **Figure 3.1**: a vacuum system split into two parts by a small wall slot at a surface area $A$ and infinitesimal thickness. The net flow of molecules from one volume to the other can be calculated using the molecular impingement rate, $\phi$, in the following way; we call $\phi_{12}$ the impingement rate for the molecules moving from the right part of the system to the left and $\phi_{21}$ the impingement rate for molecules from left to right. We can express these two quantity using **Eq. 3.4**. If no temperature differences exist in the

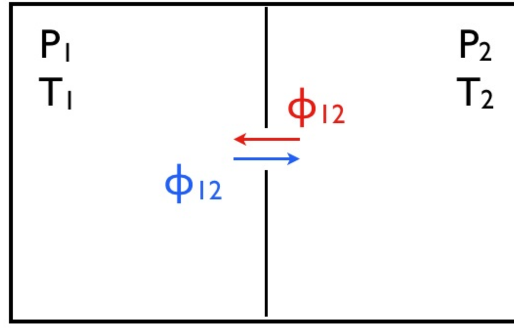


FIGURE 3.1: Schematic representation of the simplest geometry for the conductance calculation.

system, therefore the mean velocity of the molecules is the same. We can thus write the difference between the impingement rate as follows:

$$\Delta\phi = \phi_{12} - \phi_{21} = \frac{< v >}{4} A(n_1 - n_2). \tag{3.8}$$

We can express the density of the molecules using the **Eq. 3.1**

$$\begin{cases} \Delta\phi = \dfrac{< v >}{4} A(n_1 - n_2) \\ n = \dfrac{N}{V} = \dfrac{P}{k_B T}; \end{cases} \tag{3.9}$$

therefore from **Eq. 3.9** we obtain:

$$\Delta\phi = \frac{< v >}{4 k_B t T} A(P_1 - P_2). \tag{3.10}$$

Considering that

$$\dot{Q} = \Delta\phi k_B T \tag{3.11}$$

we obtain the following result:

$$\dot{Q} = \frac{A < v >}{4} (P_1 - P_2). \tag{3.12}$$

Compering **Eq. 3.12** with **Eq. 3.7**, we obtain the following expression for the system conductance:

$$C = \frac{A}{4} < v >= \frac{A}{4} \left( \frac{8 k_B T}{\pi m} \right)^{(1/2)}, \tag{3.13}$$

where we have used **Eq. 3.3** in order to obtain the last equality.
For more complex geometries we have to introduce in the description of the system the transmission probability: the probability that a molecule is transmitted from one part of the system to the other without coming back.

In vacuum technology a pump is defined as any object that removes molecules from

the gas phase[25]. A vacuum pump is characterized by its pumping speed, S in $ls^{-1}$ or $m^3s^{-1}$, which can be define as the derivative of the pump throughput with respect to the pump inlet pressure:

$$S = \frac{\partial Q_p}{\partial P}. \tag{3.14}$$

If the pressure is constant and the volumetric flow rate is due to the pump, **Eq. 3.14** becomes:

$$S = \frac{Q_p}{P}. \tag{3.15}$$

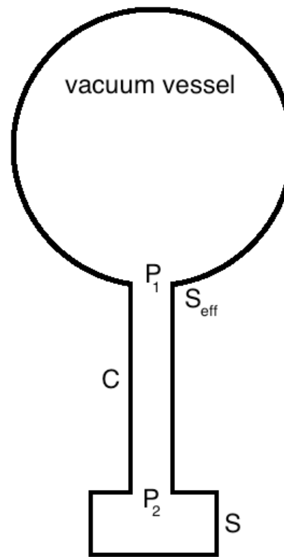


FIGURE 3.2: Schematic drawing of a gas flow restriction of conductance $C$ interposed between a pump of pumping speed $S$ and a vacuum vessel.

In a standard vacuum system (a sketch is shown in **Figure 3.2**) it often happen that the pump is connected to vessel through a restriction, flanges, tubes, or bellows, with a certain conductance. Because of this conductance the pumping speed acting in the vacuum vessel is different from the pumping speed at the pump inlet. The pumping speed at the entrance of the vessel is called effective pumping speed and can be calculated in steady state conditions considering the gas flow from the vessel and the pump:

$$\dot{Q} = C(P_1 - P_2) = SP_2 = S_{eff}P_1; \tag{3.16}$$

solving in respect of $S_eff$, it can be obtained the following expression:

$$\frac{1}{S_{eff}} = \frac{1}{S} + \frac{1}{C}. \tag{3.17}$$

**Eq. 3.17** suggests that the effective pumping speed does not depend on the installed pump if the conductance of the interposed connection is very low.

The pumping speed can be expressed using an important parameter for a pump, that is the capture probability; it is defined as the probability for a molecule that enters the pump to be definitively removed and never more re-appear in the gas base of the vacuum system. The pumping speed and the capture probability can be related considering that the pump throughput is given by the only molecules entering the pump inlet without coming back in the vacuum system, which means:

$$Q_p = \phi A \sigma, \tag{3.18}$$

where $\sigma$ is the capture probability.
Combining **Eq. 3.15** and **Eq. 3.18**, the following expression for the pumping speed is obtained:

$$S = C' A \sigma, \tag{3.19}$$

where $C'$ is the conductance for unit surface in $ls^{-1}m^{-2}$.
The maximum theoretical pumping speed for any pump is obtained when the capture probability is equal to one; this maximum pumping speed is, therefore, the conductance of the pump inlet cross section.
It has to be said that the capture probability depends on the pump geometry, therefore it cannot be used to compere the performances of pumps with different design. The only pump parameter that can be used for a comparison is the sticking probability, since it is independent from the geometry.

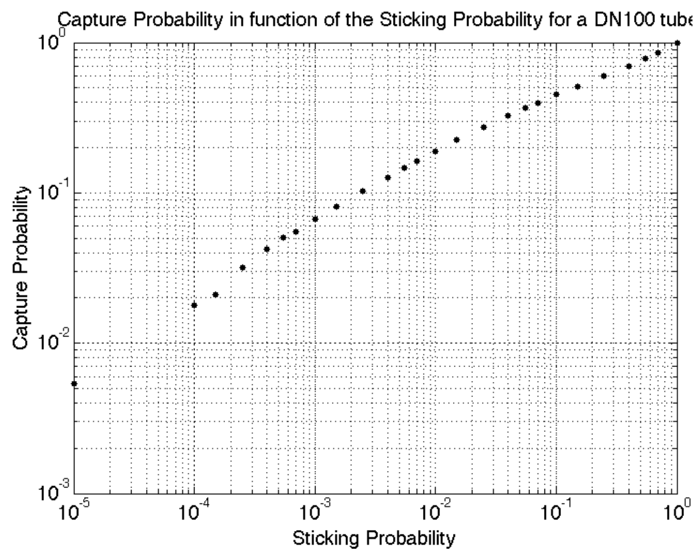


FIGURE 3.3: Capture probability in faction of the sticking probability for a DN100 stainless steel tubes 50 $cm$ long.

The sticking probably for a NEG pump has been defined in **Section 2.4** and unfortunately cannot be measured in direct way; the only way to calculate it is through a Monte Carlo simulation once the capture probability is known. In **Figure 3.3** the result of a Monte Carlo simulation, realized with MolFlow+ is reported. This plot can be used to obtain the sticking probability of a DN100 chamber once its capture probability is know.

### 3.1.2 Fischer-Mommsen Dome

A NEG coated tube works like a common pump, therefore it can be characterized with the pumping speed defined by **Eq. 3.15**.

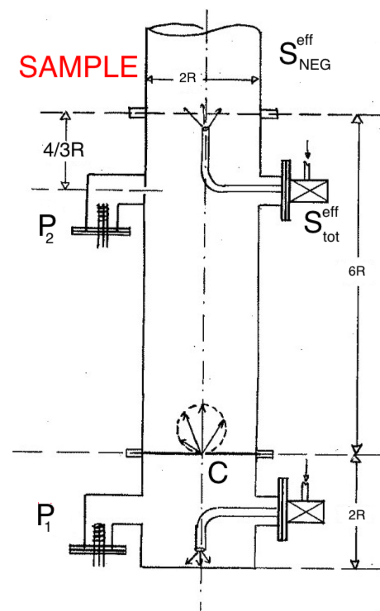


FIGURE 3.4: Schematic representation of a Fischer-Mommsen dome[7].

The most used system for the measurement of the pumping speed of a certain pump is the Fisher-Mommsen Dome; the idea is measuring the pumping speed thanks to the pressure difference between two parts of a system separated by a know conductance after the injection of a certain quantity of a gas (usually $H_2$). In **Figure 3.4** it is shown a generic Fisher-Mommsen dome; gas is injected from the bottom inlet, passes through the known conductance $C$, arrives in the upper part of the system where the pump to be tested is connected. The pressure read by the gauge 1, $P_1$, is proportional to the number of gas molecules injected in the system, instead the pressure read by gauge 2, $P_2$, is proportional to the number of gas molecules pumped by the pumps connected to the measuring dome. In the steady state condition the pump throughput is equal to the

flux injected, therefore

$$\begin{cases} Q_{1\to 2} = C(P_1 - P_2); \\ Q_p = P_2 \cdot S^{tot}_{eff}. \end{cases} \tag{3.20}$$

In stationary state the two fluxes are equal therefore:

$$P_2 S^{eff}_{tot} = C(P_1 - P_2), \tag{3.21}$$

where $S^{eff}_{tot}$ is the total effective pumping speed (defined in **3.1.1**) due to the sample and to other pumps connected to the system.
The pumping speed can be calculated solving **Eq. 3.21**:

$$\begin{cases} S^{eff}_{tot} = C\left(\frac{P_1}{P_2} - 1\right); \\ S^{eff}_{tot} = S^{eff}_{NEG} + S^{eff}_{p}. \end{cases} \tag{3.22}$$

Solving **Eq. 3.22** we obtain the following formula for the calculation of the NEG coated tube pumping speed:

$$S^{eff}_{NEG} = C\left(\frac{P_1}{P_2} - 1\right) - S^{eff}_{p}. \tag{3.23}$$

Pumping speed measurements with a tubular test dome implies some errors on the evaluation of the pumping speed because **Eq. 3.23** is valid if the pump were connected by its flanges directly to a volume which is large compered to the pump diameter and if the gauge were sufficiently far away from the pump.
The peculiar characteristic of the Fisher-Mommsen Dome is that it has been built in such a way that its geometry, its dimension and the position of its gauges allow us to measure the pumping speed as defined in **Eq. 3.23**; it can be shown using a Monte Carlo simulation that exist a gauges position such that the pumping speed measured in the dome is equal to the pumping speed measured in an ideal system [7].
Knowing the pumping speed of the sample, the capture probability can be calculated using **Eq. 3.19**. Using this equation and considering that the maximum pumping speed measurable is the conductance for the $H_2$ (is the gas with the lower mass, therefore with maximum pumping speed) at the entrance of the sample the capture probability can be calculated with the following expression:

$$\sigma = \frac{S}{S_{msx}} = \frac{S}{C_{H_2}}. \tag{3.24}$$

The capture probability is fundamental in order to obtain the sticking probability of the tested sample, which is the only parameter that can be used to compere the performance of the chamber tested with other types of pumps.

### 3.1.3 Pumping Speed System Set-Up

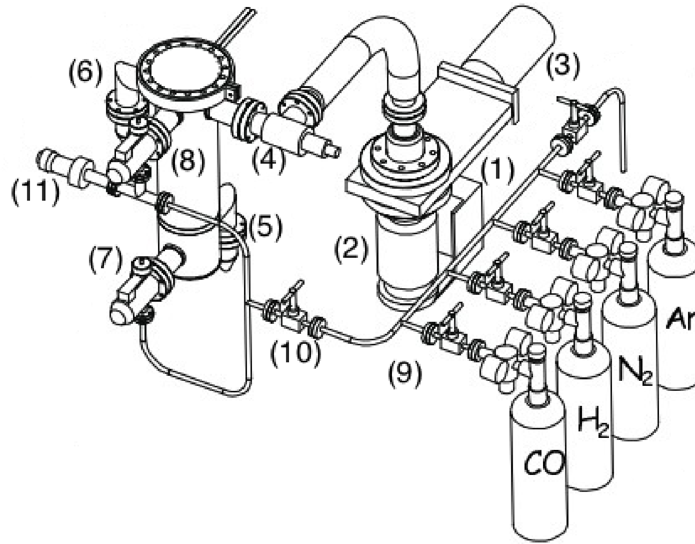


FIGURE 3.5: Sketch of the pumping speed system used for testing the NEG coated vacuum chambers.

In this section the pumping speed system used for the measurements performed is described in details.

In **Figure 3.5** a schematic representation of the pumping speed system is shown. It is composed by the following components:

- two primary pumps (oil sealed rotary pumps): one is needed to reach the condition of molecular flow inside the system (1), the other one to pump the injection line during its cleaning. Using this kind of pumps a pressure in the range of $10^3$ $mbar$ to $5 \cdot 10^{-2}$ $mbar$ can be reached ;
- turbo-molecular pump (TMP): it is a mechanical pump needed to reach pressure around $10^{-8}$ $Pa$ (2). It has an effective pumping speed ad the entrance of the vessel of 8 $l \cdot s^{-1}$ for hydrogen and $4,37$ $l \cdot s^{-1}$ for $CO$;
- pneumatic valve: it is the valve connecting the dome to the TMP (3);
- Fisher-Mommsen dome (see 3.1.2) featured a DN100 aperture for the connection of the samples. It is composed by:
  - an internal aperture which divides the bottom and the upper part of the dome. The aperture conductance for hydrogen is 34 $l \cdot s^{-1}$;
  - one cold-cathode gauge (4): it is able to measure the pressure in the range $10^{-2}$ $Torr$ to $10^{-9}$ $Torr$ and it is used for monitoring the pressure starting from the pump down to the measurements;

  - two hot-cathode gauges (5) (6): they are able to measure pressure in the range from $10^{-3}$ $Torr$ to $10^{-14}$ $Torr$ and they are used for measuring the pressure during the pumping speed measurement;
  - two needle valves (7) (8): they allow the injection of certain amount of gases into the Fisher- Mommsen dome;

- an injection line (9): it allows to inject different type of gas from the bottom or from the top part of the dome. It can be isolated through a valve (10);
- one cold-cathode gauge (11) needed to check the pressure in the injection line;
- a cryo-trap (not shown in **Figure 3.5**): it is connected between a primary pump and the injection line in order to make faster the pumping of the injection line during its cleaning. It is connected through a valve to the injection line and through another to the primary pump.

The pumping speed measurement procedure used for testing the NEG coated vacuum chambers consists in a full bake-out for 24 $h$ of the whole system while the sample is kept at a low temperature (the values depends on the type of sample) in order to not activate the NEG thin film coating. When the system reaches the degassing temperature the film is activated following the suitable activation procedure. At the end of the activation the two hot-cathode gauges are degassed for 30 $min$ each (before the degassing the two needle valves (7) (8) are closed). The last step of the bake-out/activation procedure is the cool down.
Before the beginning of a pumping speed measurement the injection line is cleaned in order to be sure that the injected gas is as pure as possible. The cleaning consists in isolating the line from the system and filling it with the desired gas; when it is full, the gas is pumped out by the cryo-trap and the primary. This procedure is repeated three times; after it the line is filled with the gas that has to be injected.
The pumping speed measurement consists in injecting a certain amount of gas from the bottom needle valve (7) and taking note of the pressure read by the two hot-cathode gauges at the end on each injection. The sample pumping speed is calculated using **Eq. 3.23**:

$$S_{NEG}^{eff} = C\left(\frac{\Delta P_1}{\Delta P_2} - 1\right) - S_p^{eff}, \tag{3.25}$$

where $\Delta P_1$ and $\Delta P_2$ are the pressures read by the gauges minus the pressure values before the injection already corrected for the gauges calibration factors.
The maximum pumping speed measurable for hydrogen is 3456 $l \cdot s^{-1}$, meanwhile for $CO$ is 924 $l \cdot s^{-1}$. A summary of the pumping speed system characteristics is reported in **Table 3.1**: The calibration factors for the two gauges are $c_1$ and $c_2$, respectively from gauge (7) and (8). Their values change since two calibrations of the system have been

TABLE 3.1: Pumping speed system main characteristics.

| | $H_2$ | $CO$ |
|---|---|---|
| $S_{eff}^{TMP}$ | $8\ l \cdot s^{-1}$ | $4,37\ l \cdot s^{-1}$ |
| $S_{eff}^{NEG}$ max | $3456\ l \cdot s^{-1}$ | $924\ l \cdot s^{-1}$ |
| $C$ | $34\ l \cdot s^{-1}$ | $6,5\ l \cdot s^{-1}$ |
| $c_1$ | $1,89$ | $0,612$ |
| | $0,22$ | $0,52$ |
| | $0,22$ | $0,58$ |
| $c_2$ | $1,44$ | $0,473$ |
| | $0,2$ | $0,47$ |
| | $0,20$ | $0,48$ |

performed. In particular, the values of the first row have been used for the reference sample of the ageing campaign and for LSS3_1, those of the second row for LSS3_2 and LSS1_1. The last values reported have been used for the pumping speed measurements of the NEG coated tubes of the coating campaign.

For more details about the measurement procedure see **Appendix A**.

## 3.2 NEG Coated Chambers Preparation

In the following the procedure used for the preparation of all the NEG coated chambers tested is presented in details. In particular, the coating technique used, the magnetron sputtering, is described in order to underline its advantages with respect to the other techniques. Moreover, both the technique used for the cathodes production and the experimental set-up are illustrated.

### 3.2.1 Magnetron Sputtering

A sputtering technique consists in bombarding a material with ions in order to transfer as much energy as possible to the its atoms. If the energy is equal or higher than the sputtering threshold, the atoms can leave the surface and can deposit on surrounding surfaces forming a thin film coating. This technique does not require additional thermal energy, since it involves direct momentum transfer from bombarding ions to the target atoms of the cathode. This deposition technique presents some advantages if compared with other:

- the sputtering ions have enough energy to break chemical bonds, therefore any material can be sputtered;

- alloys and compound can be sputtered without changing their composition;
- higher density of nucleation islands can be obtained (smaller dimensions of grains);
- the film desorption rate can be made uniform over a very large areas (uniform composition and thickness);
- safe production of NEG coatings from stable materials;
- the energies implied are lower enough to guarantee no subsurface damage, but higher enough to favor a high adhesion of the coating on the substrate.

Because of all these advantages the sputtering techniques has been chosen for NEG deposition at CERN.
Between the sputtering techniques the Magnetron Sputtering has been chosen for coating the stainless steel tubes used as samples. In the following this techniques is described referring to the particular system used for the coating, represented in **Figure 3.6**. The

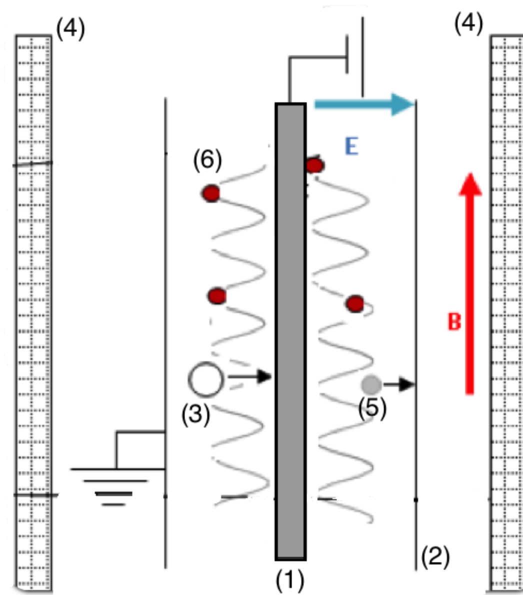


FIGURE 3.6: Schematic representation of the magnetron sputtering configuration used for the realization of the sample tested.

main elements of the coating tower are a cathode (1), composed by the material we want to sputter, an anode, represented by the wall of the stainless steel tubes (2), and a inert gas (3), which in the present case is $Kr$, needed to sputter the cathode material. The deposition is performed in a vacuum chamber filled with $Kr$ with a certain pressure and in the presence of a radial electric field, due to the tension applied between the anode and the cathode, and a axial magnetic field, generate by a current flowing in a cylindrical solenoid (4). The $Kr$ ion are obtained from the gas applying a negative voltage to the cathode that starts to emit electrons (5) which are accelerated toward the substrate,

therefore can undergo collisions with the $Kr$ atoms filling the vacuum chamber; these collisions may results in the production of a new electron, if the electron energy is higher than the $Kr$ ionization energy, which is about 14 $eV$ for $Kr$:

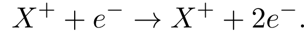

$$X^{+} + e^{-} \rightarrow X^{+} + 2e^{-}.$$

Both the electrons are affected by the electric field: they can collide with other $Kr$ atoms during their journey toward the anode, so that a cascade of electrons and ions occurs. This mechanism gives start to a gas breakdown: the gas filling the chamber, a mixture of electrons and ions, is a low-pressure, diffused plasma, known as glow discharge. This glow is principally ignited and sustained thanks to the electron generation by gas-phase ionization.
The positive $Kr$ ions are accelerated by the electric field toward the cathode; they interact with its surface atoms transferring to them part of their momentum. If the energy transferred to the cathode atoms is higher than the sputtering threshold (reported in **Table 3.2** for the interesting materials), these atoms can leave the cathode surface as neutral particles (6) and they may reach the anode surface where they remain sticked forming a thin film.

TABLE 3.2: Sputtering threshold values for suitable NEG materials bombarded with $Kr$.

| Target Material | Sputtering Threshold $[ev]$ |
|---|---|
| $Ti$ | 17 |
| $V$ | 25 |
| $Zr$ | 18 |
| $Hf$ | |

Since the sputtered material has to pass through the plasma to reach the anode, it could lose energy interacting with its particles. To minimize these interactions, which can affect the adhesion of the film, the distance between the cathode and the anode should be grater than the mean free path of electrons for the working gas pressure. Because of the high working pressure the mean free path is too short, if only an electric field was applied to the system. In order to minimize this effect a magnetic field is applied: it reduces the minimum self-sustaining plasma pressure and it increases the electron path. The charged particles of the plasma are affected by the Lorentz's force:

$$\mathbf{F} = q(\mathbf{E} + \mathbf{v} \times \mathbf{B}).$$

Solving the motion equation in the case of the a uniform and constant electric and magnetic field, as in the present case, we obtain that the electrons (and the ions too) follow

a cycloid-like trajectory, that increase their mean free path: the electron-sputtered material collision are, therefore, less.
The two most important parameters that affect the growing film morphology are the discharge pressure and the ratio between the temperature of the substrate and the melting temperature of the target material. A model exists to predict the microstructure of the metal coatings deposited by sputtering using a cylindrical magneton source as a function of these two parameters: Structure Zone Model.
The details of this model are beyond the aim of this thesis, but it has to be mentioned in order to take into account the heating of the substrate during the deposition. In particular, at the pressure ($4,5 \cdot 10^{-3}\ Torr$) and temperature (100 °C) used, all the coatings belong to the same Transition Zone in the structure zone model: the microstructure of the film is controlled by surface diffusion and is characterized by a dense fibrous structure with a smooth highly reflective surface.
During the deposition attention must be payed to the vapor pressure of the elements composing the cathode because the cathode is not cooled: a vapor pressure contribution may add to the deposition rate.
The deposition rate is define as the quantity of matter deposited on the substrate (the anode) per unit time. It depends on the:

- distance between the substrate and the cathode;
- geometry of the deposition system;
- sputtering yield, defined as the the number of target atoms or particles ejected per incident ion.

This phenomenon is particularly relevant for high power applied to the cathode, because the temperature of the cathode depends on the current flowing in it. The deposition rate of material with high vapor pressure is higher than the deposition rate for other material and this preferential vaporization effect must be take into account in the calculation of the deposition rate needed for a certain film composition.
The calculation of the deposition rate is important because allows us to calculate the thickness of the film during its deposition, therefore the amount of time needed for having a 1 $\mu m$ of NEG coating.
The sputtering yield for the materials used is need for the calculation of the coating thickness. It depend on many factors:

- the mass;
- the energy (applied voltage);

- the angle of incidence;
- the chemical nature of the incident ion;
- the total pressure of the vacuum system;
- the crystallographic structure of the target (the cathode);
- the temperature of the target (the cathode).

TABLE 3.3: Sputtering yield for the materials used bombarded with $Kr$ at 500 $V$.

| Target Material | Sputtering Yield |
|---|---|
| $Ti$ | $0,5$ |
| $V$ | $0,6$ |
| $Zr$ | $0,5$ |
| $Hf$ | $0,9$ |

For its calculation the formula proposed by Yamamura has been used [26]. In **Table 3.3** the sputtering yields for the elements used are reported. This values have been used not only for calculating the time needed for growing a thin film of 1 $\mu m$, but also for predicting the composition of the films, as it will be explained in details in the following section.

### 3.2.2 Sample Mounting

A fundamental part of the coating system is the cathode. There are various kind of cathodes; among them there is the composite one. It is consists in several bulk materials that allow the deposition of alloys or compounds starting from available material without preparing a bulk target of the desired composition.
This type of cathode, shown in **Figure 3.7**, can be made of inter-twisted wires and has the disadvantage that the composition of the coating can only be changed in a discontinuous way by varying the number and/or the diameter of the wire of each element of the cathode, but they are cheaper than a bulk target. For this reason they have been chosen as cathodes for the production of the NEG thin film coatings of the LSSs becoming the standard cathode for the production of $TiZrV$ films.
The differences between the films produced using a bulk cathode and a composite one have been recently studied [27]. It has been proved that film composition is identical to the composition of the $TiZrV$ alloy target, meanwhile using a three wires twisted target the composition is not the same as the one predicted but it is very close to it.
The film composition is predicted calculating a total diameter and a total sputtering yield for the cathode chosen. The first parameter is the sum of diameters of the wires

FIGURE 3.7: Examples of some of the cathodes used for the realization of the NEG thin film coatings tested.

used, meanwhile the second is the sum of the the element sputtering yield weighted for their relative diameter:

$$y_{TOT} = \frac{d_{Ti}}{d_{TOT}} y_{Ti} + \frac{d_V}{d_{TOT}} y_V + \frac{d_{Zr}}{d_{TOT}} y_{Zr} + \frac{d_{Hf}}{d_{TOT}} y_{Hf},$$

in the case of a cathode composed by four elements.
The atomic percentage in the film is then estimated as a product between the relative diameter and the relative sputtering yield:

$$i[\%] = \frac{d_i}{d_{TOT}} \cdot \frac{y_i}{y_{TOT}}.$$

Even if a lot of approximations have been used in order to arrive to the element atomic percentage (for example, it has not been taken into account that some parts of wires are hidden behind other wires), the predicted values are not so different from those measured. In fact, for each sample the composition is checked after the coating through the energy dispersive spectroscopy.
Once the film composition is chosen the cathode is prepared inter twisting the wires needed for having the desired composition, as can be seen in **Figure 3.8(a)**, where the machine use is shown. In **Table 3.4** the materials used for the the cathodes production are listened.
Before the cathode fabrication, all the wires are chemically degreased (see B for the details). The cathode is then fixed to the upper part of the coating tower, as can be seen from **Figure 3.8(b)**.
The DN100 stainless steel tubes 50 *cm* long, which will be coated with the NEG thin

TABLE 3.4: Materials used for the cathodes fabrication.

| Element | Purity |
|---|---|
| Titanium | 99, 99+% |
| Vanadium | 99, 8% |
| Zirconium | 99, 2% |
| Hafnium | 97% (main impurity *Zr*) |

(a) Picture of the machine used for cathodes production.

(b) Picture of the upper part of the coating tower.

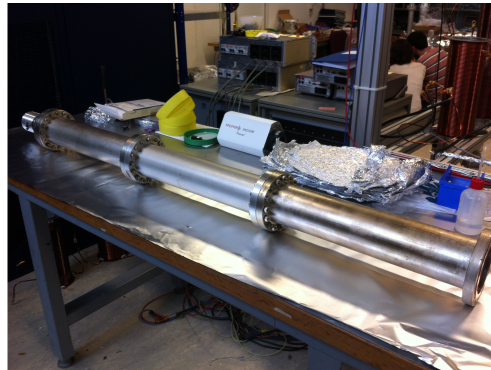

(c) Picture of the mounted coating tower.

FIGURE 3.8: Pictures of the main coating tower components.

film, is mounted in between two stainless steel tubes of the same dimensions working as extensions, as can be see in **Figure 3.8(c)**, where the whole coating tower mounted is shown. The two extensions are need in order to avoid edge effects: the magnetic filed and the plasma must be as uniform and stable as possible.
The chamber used as sample are cleaned before the coating with a cleaning procedure developed at CERN, Net Inox, whose details are reported in **Appendix B**.
In order to have samples of the film deposited with a suitable size for the microscopic measurements (XPS, SEM, XRD and EDS), two copper strips are inserted into the coating tower: one in the bottom part of the upper extension, the other in the upper part of the bottom extension. The strips are located in the two extension tubes and not in the sample, since it is important that its extremities are coated with the NEG thin

film, especially for the transmission measurements.

### 3.2.3 Deposition System Set-Up

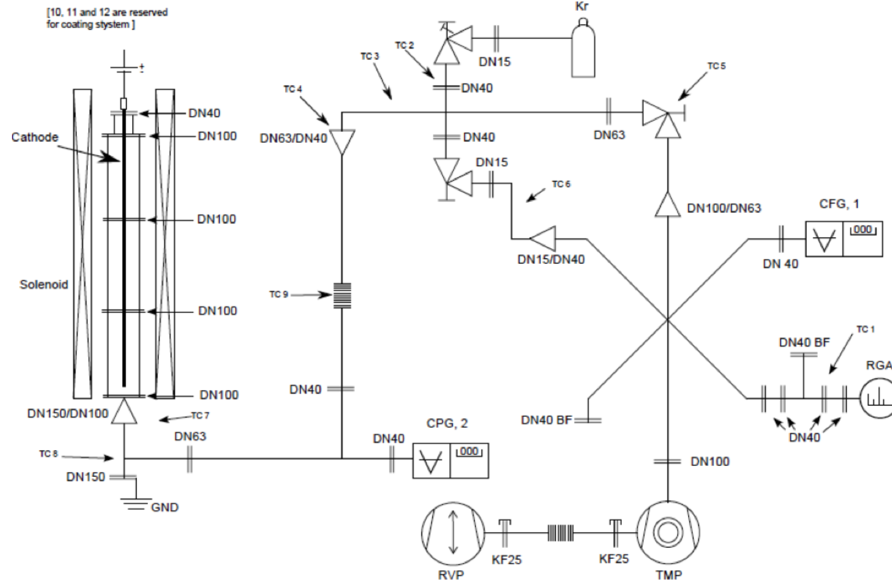


FIGURE 3.9: Scheme of the deposition system used for the production of all the NEG thin films tested.

In **Figure 3.9** a scheme of magnetron sputtering apparatus is reported. It can be see that the coating tower is connect to the rest of the system through a bellow. A needle valve put into communication the $Kr$ injection line and the system. The system is pumped by a pumping group composed by a turbo-molecular pump ($S_{N2} = 355\ l \cdot s^{-1}$) connected to a rotary vane pump. This group is connected to the system through a main valve, which remain closed during the coating when the system is pumped by the TMP through a smaller conductance (the connection is realized by a bypass valve). Above the pump a compact full range gauge ($9 \cdot 10^{-7}$ to $10^5\ Pa$) and a residual gas analyzer are connected. Meanwhile, at the bottom of the coating tower a compact process ion gauge ($2 \cdot 10^{-4}$ to $10^5\ Pa$) is connected in order to read the pressure during the deposition. The deposition system is, also, featured by two DC power supplies, one for the cathode and one for the magnet. In **Figure 3.10**, the pictures of the deposition system before and during the coating are shown. It can be seen how the magnet can be lowered over the tower for the production of the axial magnetic field. This magnet has been produced at CERN using Kapton insulated copper wires wrapped around a hallow iron core.

After the mounting and the leak detection, the deposition system is put under vacuum and then baked for 24 $h$: all its parts are heated at 150 °C with the exception of the coating tower which is baked at 250 °C. The two filaments of the RGA are degassed at the end of the bake-out for 45 $min$ each. When the whole system is at room temperature

an RGA scan is taken in order to checked the composition of the atmosphere inside the tower: it should be as pure as possible in order to avoid film contamination.

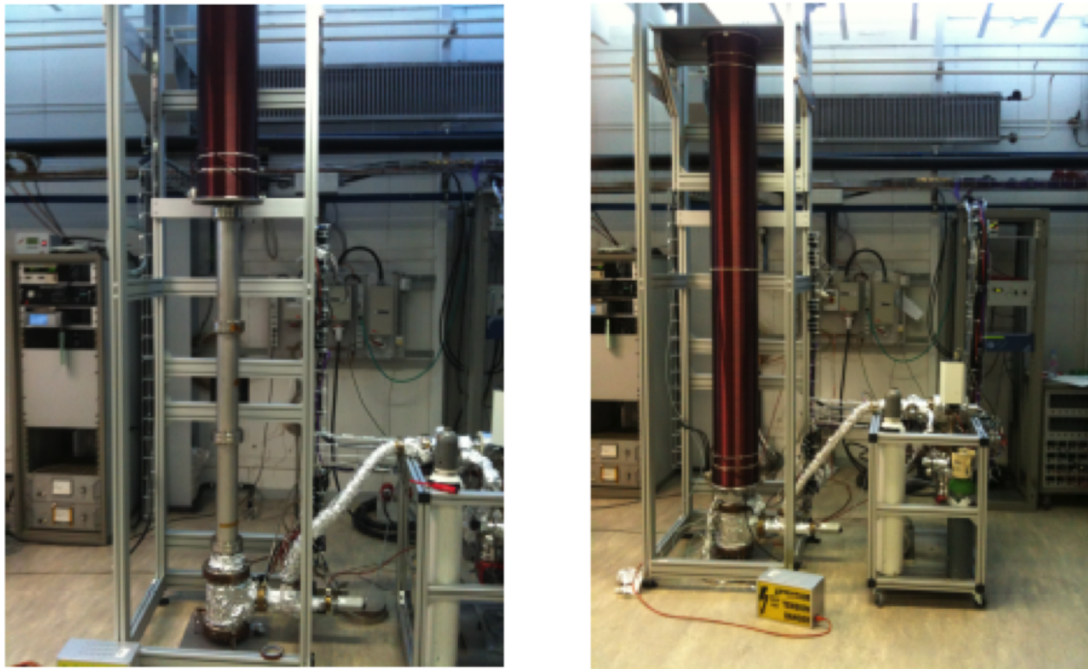

(a) Deposition system before the coating when the magnet is above the tower.

(b) Deposition system during the coating when the magnet is lower over the tower.

FIGURE 3.10: Pictures of the deposition system.

During the film deposition the tower is kept at 100 °C in order to enhanced the film roughness, as already explained in **Chaper 2**. The deposition is performed with the main valve closed and the bypass opened in order to not waste to much $Kr$. Once the desired thickness of the NEG film is reached, the magnetic and the electric field are switched off and the system cool down.

The stainless steel DN100 NEG coated chamber is used for the pumping speed measurements (sticking probability, electron stimulated desorption and pumping speed), meanwhile pieces of the two copper strips are cut and used for the microscopic measurements (XPS, SEM, XRD and EDS).

## 3.3 Characterization Methods

Since the activation of a NEG thin film is completed when the oxygen surface content reaches a minimum and the pumping speed its maximum value, both surface elemental analysis and pumping speed measurements are needed to monitor the activation process. Different, but self-consistent with the pumping speed measurements, possible methods to test the pumping properties of a tubes are performing electron stimulated desorption

measurement (ESD) and sticking probability measurements (SP) (both techniques described in this section).
It has been decided to perform for each sample only ESD and SP measurements; only for few sample, pumping speed measurements have been performed.
Other characterization measurements are needed since the pumping properties are linked with the morphology of the sample, meanwhile the activation temperature to the grains dimensions. Moreover, the thickness and the bulk composition have been checked.
In conclusion, for all the samples the performed measurements can be divided as follows:

- macroscopic measurements, needed to tested their pumping properties:
  - sticking probability for $H_2$ and $CO$ measurements;
  - electron stimulated desorption (ESD) measurements.
  - pumping speed measurements;
- microscopic measurements:
  - scanning electron microscopy (SEM), for the surface morphology;
  - energy dispersive spectroscopy (EDS), for the bulk composition;
  - x-rays photoelectron spectroscopy (XPS), for the surface elemental analysis;
  - x-rays diffraction measurements (XRD), for the grain dimension.

In this section the characterization methods used are described in some details.

### 3.3.1 Sticking Probability Evaluation

The sticking probability, $\alpha$, is defined as the ratio between the rate of chemically adsorbed molecules and the total number of molecules incident to the surface. As already said, it is the only parameter that can be used for pumping performance comparisons, since it is not related to the pump geometry. Unfortunately it is not possible to design an experiment to direct measure this parameter, since the geometry of a pump always affects the experiment.
A Monte Carlo simulation provides a way to link the pressure change measured during a transmission experiment to the sticking probability thanks to the parameter $R$ which can both be simulated and measured.
The parameter $R$ is defined as the ratio between the system pressure when there is no

NEG pump and the one when the NEG pump is present:

$$R = \frac{\frac{Q_{in}}{S_{TMP}}}{\frac{Q_{in}}{S_{TMP} + S_{eff}^{NEG}}}. \tag{3.26}$$

Using the definition of sticking probability the pumping speed of a NEG coated tubes can be written as

$$S = \alpha C' A, \tag{3.27}$$

where $C'$ is conductance in $l \cdot s^{-1} \cdot m^{-2}$ and $A$ is the cross section of the sample in $m^2$. It can be proved that the $R$ value is related to the sticking probability of the sample as follows:

$$R = 1 + \frac{CA}{S_{TMP}} \alpha. \tag{3.28}$$

Knowing, therefore, the sticking probability of the tested pump $R$ can be calculated. It is possible to design a Monte Carlo simulation where the sticking probability is assigned to the sample; a known quantity of gas injection is simulated and the $R$ parameter estimated. The simulation is repeated for many values of $\alpha$ and the curve, shown in **Figure 3.11**, with the variation of $R$ in function of the sticking probability is determined.

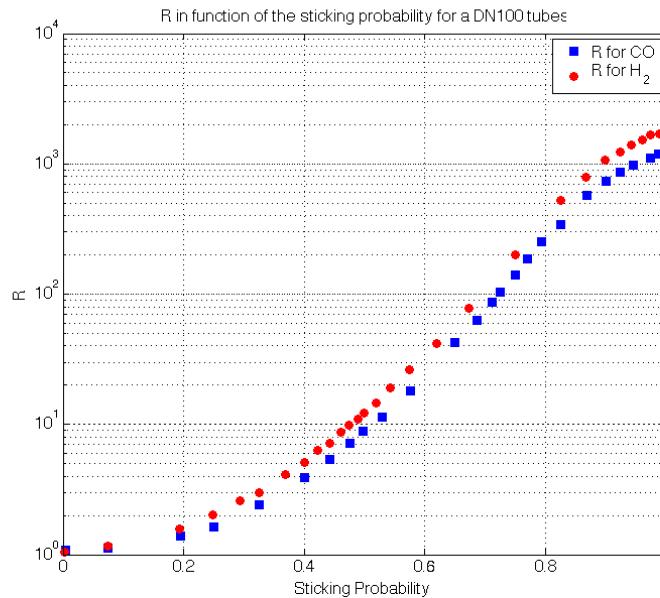


FIGURE 3.11: $R$ parameter in function of the sticking probability for the ESD system obtained by a Monte Carlo simulation.

The $R$ parameter for the tested sample can be calculated using a transmission measurements; a constant amount of gas is injected, as in the simulation, into the sample while the system pressure is record by an RGA located on the other side of the sample. The ratio between the pressure measured when the NEG is not activated (at 120 °C in

the procedure used) and that measured when it is activated (heating temperature x in **Eq.3.29**) is equal to the $R$ defined by **Eq. 3.26**:

$$R = \frac{P(120\,^{\circ}C) - P_{res}(120\,^{\circ}C)}{P(x) - P_{res}(x)}. \tag{3.29}$$

The sticking probability is linked with the reactivity and the cleanness of the NEG surface, therefore it can be used for monitoring the activation process: high sticking probability are expected for completely activated samples.

### 3.3.2 Electron Stimulated Desorption

The impingement on a solid surface of an electron of energy higher than a few $eV$ may result in the desorption of gas molecules and ions. The number of molecules desorbed per particles impinging on the surface is called desorption yield; it depends on the nature of the particle, the material, the number of particles that have already impinged on the surface and the cleanliness. It has been proved that the ESD yields is strongly affected by the impinging electron energy up to 500 $eV$, while in the range of $2 - 15$ $KeV$ that can be considered as a constant. Most of the desorbed molecules are neutral, however ions are also desorbed to a much lower extent.
The desorbed molecules are ejected with energy of a few $eV$ up to 10 $eV$. Since the their energy is so high, the direct momentum transfer is not the dominant process in ESD. The ESD, in fact, can be treated as an isolated interaction between an electron and an adsorbate where electronic energy transfers has to be considered, as one of the earliest ESD model, proposed by Menzel, Gomer and Redheah (MGR model) do[2].

This phenomenon can be used to monitor the activation of NEG coated vacuum chambers. The surface of a NEG becomes clean with the activation, therefore when a decrease of the desorption yield is expected. Moreover the NEG surface is also reactive, thus a certain probability that a desorbed molecule is re-adsorbed exists.
In the present work the internal surface of NEG coated DN100 stainless steel tubes has been bombarded with the electrons produced by the electron source shown in **Figure 3.12** after each steps of a heating cycle. When the NEG is not activated the degassing induced by electron is high because the oxide layer. Therefore, the difference between the pressure before and during the bombardment is high. When the NEG is, instead, active the oxide layer is no more present on the surface (the oxygen in now in the bulk

[2]The theory behind the electron stimulated desorption is beyond the aim of the present work, therefore, for more detailed dissertation see [28], [29] and [30]

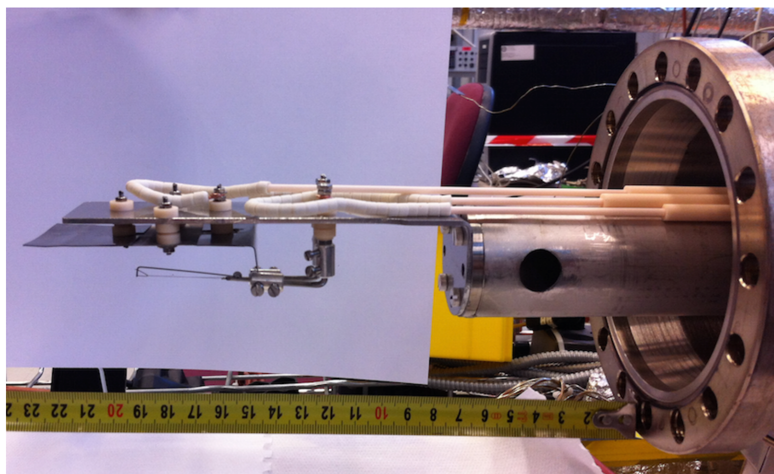

FIGURE 3.12: Picture of the electron source used for the electron stimulated desorption measurement.

of the material), which is not only clean but also very reactive. In this case, the pressure difference is small. Conventionally, a NEG thin film is fully activated when this difference is around $10^{-10}$ $Torr$.

### 3.3.3 ESD System Set-Up

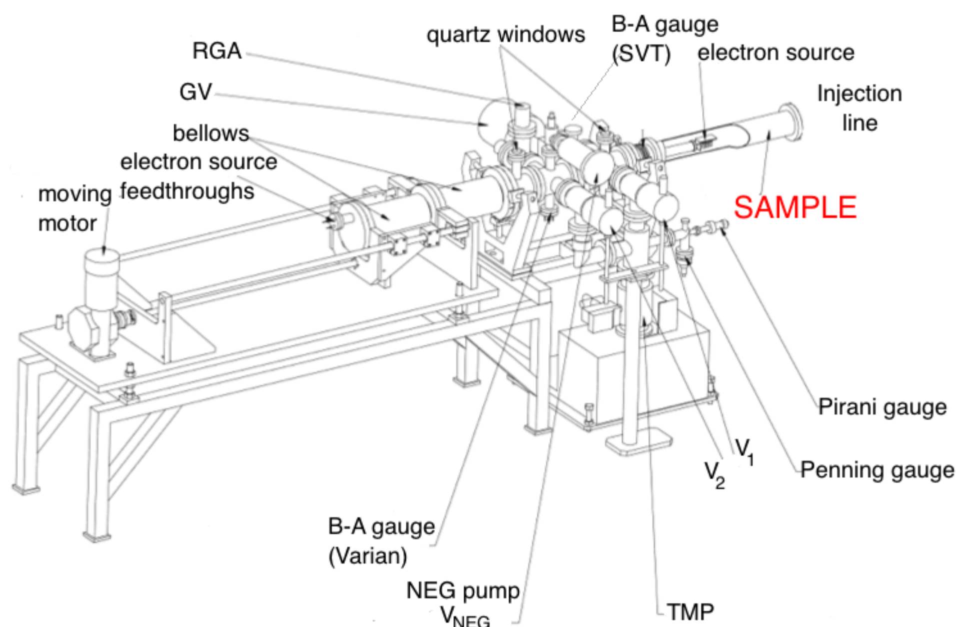


FIGURE 3.13: ESD system: it has been used for performing both the sticking probability and the electron stimulated desorption measurements.

Both the sticking probability and the ESD measurements are performed on the same machine, shown in **Figure 3.13**. It is composed by two vacuum systems which can be isolated one from the other by means of a gate valve. On the left extremity of the

system there is a long bellow kept under vacuum where the electron source is housed, meanwhile to the right extremity is attached to an injection provided by two calibrated leaks, one for $H_2$ ($\dot{Q} = 2,31 \cdot 10^{-7}$ $Torr \cdot l \cdot s^{-1}$) the other for $CO$ ($\dot{Q} = 3,19 \cdot 10^{-6}$ $Torr \cdot l \cdot s^{-1}$). The injection line is pumped by its one pumping group, since it is usually isolated from the rest of the system and communicates with it only during the sticking probability measurements.

The sample (DN100 stainless steel tube 50 $cm$ long) is located between the bellow and the injection linen (in **Figure 3.13** the position of the sample is highlighted, meanwhile the injection line is missed). Both the sample and electron source are pumped using a common pumping group (a TMP with $S_{N_2} = 355$ $l \cdot s^{-1}$ connected to a rotary vane pump); these sections could be isolated as required using two pneumatic valves and a gate valve; the pneumatics valves allow the isolation of system sample part or the electron source part from the pumping group, meanwhile the gate valve allows the isolation of the electron source part from the sample part. In **Figure 3.13** the electron source is shown inside the sample, but through an automatic motor it can be extracted from the sample ad located beyond the gate valve. Thank to the valve it is, therefore possible to keep under vacuum the left side of the system during the samples mounting and dismounting. A NEG strip pump is installed on the electron source side, in order to keep it always under dynamic vacuum, even when this section isolated form the pumping group.

The system is also provided by some pressure gauges: a cold cathode gauge, two Bayard-Alpert gauges and an residual gas analyzer, whose positions are indicated in **Figure 3.13**. These gauges cover different ranges of pressure and are used to cross check the values read by the RGA during the measurements.

The ESD system can be baked in two different way: a total bake-out can be performed which involves the whole system and a partial bake-out involving only the sample side of the system (injection line included). The last type is needed every time a new sample is mounted on the system since this part is vented during the dismounting and mounting operations. It is performed with the gate valve closed, therefore the RGA does not have to be dismounted and degassed (its position is beyond the gate valve on the electron source side), meanwhile the Bayard-Alpert gauge on the sample side has to be degassed. If a total bake-out is needed (too high pressure in the electron source side), the whole ESD is heated and all the gauges degassed, even the electron source is degassed in this case.

When the system is at the degassing temperature (150 °C) the first heating step of the sticking probability and ESD measurement procedure is performed: sample heated at 120 °C for 2 $h$ (during the bake-out the sample is kept at 80 °C). After the cool down the sticking probability measurement is performed. A selection of masses are followed using the RGA; a residual value for the pressure is registered before starting the $H_2$ injection. When the equilibrium is reached a new pressure value is taken. This procedure is followed

also for $CO$. At this heating temperature the sticking probability for both the gases is conventionally taken equal to $10^{-4}$: the NEG thin film is not activated therefore does not pump. The measurement at this temperature is used as reference temperature for all the other temperatures measurements (see **Eq. 3.29**).
The ESD measurements at 120 °C follows; the electron source is inserted into the sample by means of the bellow compression. Using a high voltage power supply the sample is charged to $-550\ V$, the plate to $-100\ V$ and the tungsten filament to $+50\ V$. The RGA starts to follow the masses before the switching on of the electron source and, as in the case of the sticking probability, a residual pressure is taken. The electron source is turned on (1 $mA$ of current flows in the filament) and the sample is bombarded with electrons for 100 $s$, when another pressure value is taken. The system total pressure variation is also recorded; the gauge used for monitoring this pressure is the Bayard-Alpert located near the RGA (called SVT gauge).
At the end of the measurements at 120 °C the second step of the heating cycle starts: sample heated at 160 °C for 2 $h$. The procedure is composed by five steps: 120 °C, 160 °C, 200 °C, 250 °C, 300 °C. All the steps last 2 $h$ and at the end of each, when the sample reach the room temperature, the two types of measurements are performed.

For all the details about the measurement procedure see **Appendix C**.

### 3.3.4 Scanning Electron Microscopy

Imagines of a sample, like that show in **Figure 3.15**, can be produced by scanning the sample with a focused beam of the electrons. This is the principle behind the scanning electro microscope. The electron beam is generally scanned in a raster scan pattern, and the beam position is combined with the detected signal to produce an image.
When a focused beam of electrons hit a surface a number of detectable signals are produced; the most common are:

- secondary electrons;
- backscattered electrons;
- X-rays.

For morphology analysis secondary electrons detection has been used, meanwhile for the quantitative information about the composition X-rays have been used (Energy Dispersive X-rays Spectroscopy, EDS). In particular, in the present work, scanning electron microscopy has been used for the evaluation of:

- morphology;

- thickness;

- bulk composition.

The machine used at CERN for testing all the NEG sample produced is Sigma ZEISS SmartSEM equipped with 50 $mm^2$ X Max EDS detector (Oxford instruments), calibrated with Silicon, meanwhile Stratagem software has been used for the thickness measurement.
Electrons thermionically emitted from a cathode filament are drawn to an anode and focused by two successive electromagnetic lenses into a beam with a very fine spot size that is typically 10 $\AA$ in diameter. Pairs of scanning coils located at the objective lens deflect the beam either linearly or in raster fashion over a rectangular area of the specimen surface. Electron beams having energies ranging from a few $keV$ to 50 $keV$ with a common value of 30 $keV$ are used.

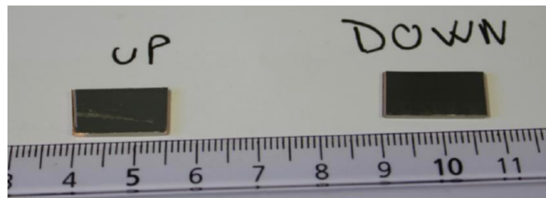


FIGURE 3.14: Example of the samples used for the SEM measurement. In this case the two copper substrate are coated with $Ti_{30}Zr_{30}V_{40}$.

The samples consist in small pieces (shown in **Figure 3.14**) of the two copper strips coated withe the NEG, as explained in **Section 3.2.2**. It has been decided to prepare two sample, one coming from the upper part of the coating tower, the other from the bottom, in oder to check the uniformity of the film deposited. In the example reported

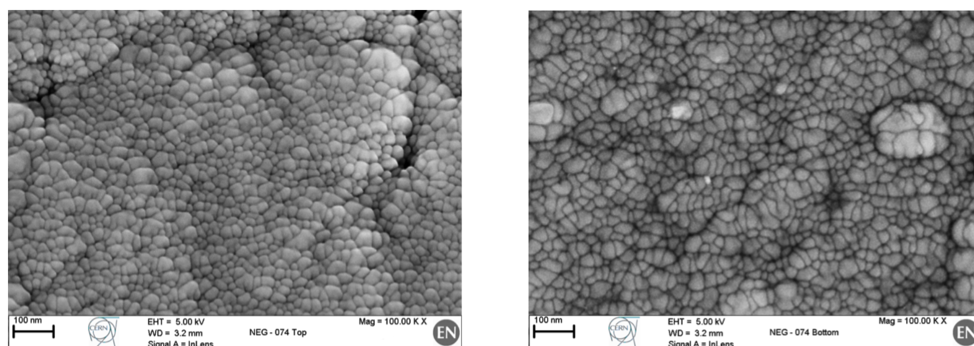


(a) SEM imagine of $TiZrV$ top surface: scale 100 $nm$, EHT 5 $kV$ and magnification 50 KX.

(b) SEM imagine of $TiZrV$ bottom surface: scale 100 $nm$, EHT 5 $kV$ and magnification 50 KX.

FIGURE 3.15: Examples of SEM imagines of a $Ti_{30}Zr_{30}V_{40}$ surface.

(**Figure 3.15**), only slightly differences can be observed in the morphology: the typical cauliflower structures can be individuated in both the surfaces.
The thickness of a NEG sample can be calculated in two different ways: peeling off the coating from the substrate and using the electron beam for estimating the thickness, thanks to a program which calculate the k ratio (intensity of the $i$ sample element over intensity of the standard). The first method is not always applicable since the peeling off of the film is problematic and the electron beam should be perpendicular to the sample profile in order to obtain a reliable measurement. The second method makes use of the dependence of excited sample volume on the accelerating voltage; measuring in the same sample place the composition for different accelerating voltage allows to estimate the thickness.

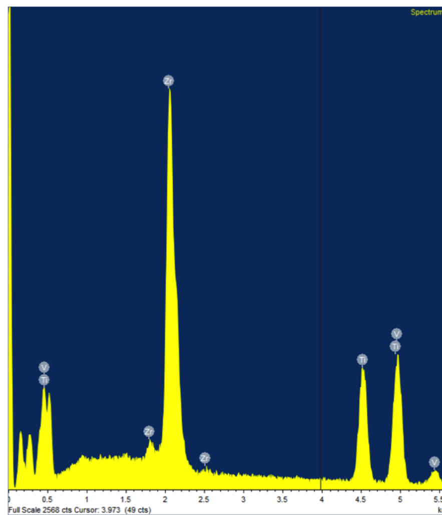


FIGURE 3.16: ESD spectrum of $Ti_{30}Zr_{30}V_{40}$ top sample.

The composition analysis relies on the detection of the X-rays emitted by the sample when in an atom a vacancy, left by a kicked out electron, is filled by an outer electron which during the transition emits X-rays characteristic of the energy levels. The X-rays emitted are collected and transformed into a voltage signal, whose intensity is proportional to the number of atoms present in the surface. In **Figure 3.16** the ESD spectrum of the $Ti_{30}Zr_{30}V_{40}$ sample is shown as example. The atomic composition for both samples (top and bottom) is always an average of three or four measurements. For the sample used as example, the average composition is reported in **Table 3.5**

TABLE 3.5: Example of the EDS results for a $TiZrV$ NEG thin film.

| Element | Average [at. %] | Standard Deviation |
|---|---|---|
| $Ti$ | $29,9$ | $0,24$ |
| $Zr$ | $29,8$ | $0,21$ |
| $V$ | $40,4$ | $0,35$ |

### 3.3.5 X-Ray Photoelectron Spectroscopy

X-ray photoelectron spectroscopy (XPS) is a surface-sensitive quantitative spectroscopic technique which makes us of a photon beam of a specific energy for exciting the electronic states below the surface of a sample. Electrons, thanks to what is called photoelectric effect, may leave the atom at which they were bound and escape from the sample surface with an energy proportional to their binding energy. They are then filtered, on the basis of their energy via a hemispherical energy analyzer, before the intensity for a defined energy is recored by a detector. The scheme of the measurement equipment is shown in **Figure 3.17**. Even if the photons can penetrate deep into the sample, the XPS is

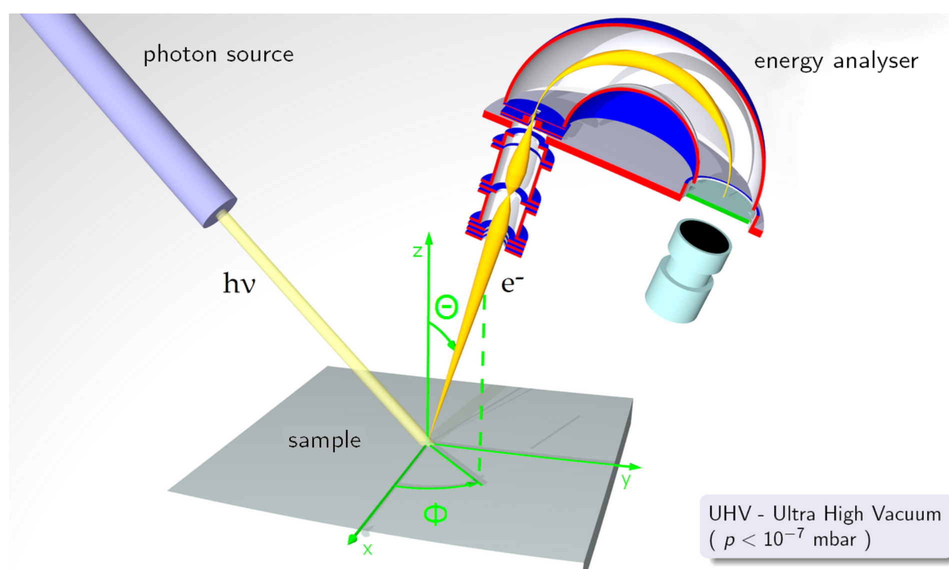


FIGURE 3.17: Scheme of the experimental apparatus needed for performing a XPS measurement.

a surface-sensitive technique, since the escape depth of the ejected electrons is limited: electrons from depths grater than 10 $nm$ have a low probability of leaving the surface without undergoing an energy loss event.

In the present work the XPS is used in order to check surface metallic composition and to monitor the activation process through the change in the surface chemical composition. It is know that the binding energy is affected by the oxidation state of the atom: electrons coming from an atom with a high oxidation number own a higher binding energy than those from an atom with low oxidation number. This phenomenon is known as chemical shift.

In case of NEG thin film, therefore, a shift at lower binding energy in the XPS peaks for metallic elements is expected after the activation, since during this process the metals are reduced. Another observable effect is the decrease of the $O1s$ peaks, because during the activation the oxygen diffuses from the surface into the bulk of the NEG material.

At CERN a procedure for evaluating the good qualities of a NEG sample has been developed [31]. The tests have been designed for testing $TiZrV$ film, but in the present work have been used for NEG thin film with other types compositions ($HfV$, $ZrV$ and $TiZrHfV$).
The test consists in the acquisition of survey and multiplex spectra of a small sample, coated withe the vacuum chamber (NEG thin film coated on a copper strip as explained in **Section 3.2.2**), after the following steps:

- as received sample at room temperature (the samples are wrapped in aluminum foil after the deposition);
- 1 $h$ of *in situ* heating at 160 °C;
- 1 $h$ of *in situ* heating at 200 °C;
- 1 $h$ of *in situ* heating at 250 °C;

The photons source is $MgK_\alpha$ (1254 $eV$) and the emission angle is 45°. The analyzer pass energy is 89 $eV$ in the case of survey spectra and 35 $eV$ in case of multiplex spectra. For other details see [31].

Following the CERN standard, a NEG film is acceptable when:

$$\begin{cases} \Delta O_{1s} = \dfrac{O_{1s}(RT) - O_{1s}(250)}{O_{1s}(RT)} \cdot 100 > 66\%; \\ \Delta C_{1s} = \dfrac{C_{1s}(RT) - C_{1s}(250)}{C_{1s}(RT)} \cdot 100 \lesssim 50\%; \\ \text{Carbon transformation in carbide} = \dfrac{C_{carbide}(250)}{C_{1s}(250)} \cdot 100; \\ \text{C surface percentage on the as received sample} < 40\%. \end{cases} \tag{3.30}$$

The initial carbon concentration is an indication of the cleanliness of the as received surface and therefore of the deposited layer. The transformation of carbon, initially present in form of hydrocarbons, in carbide is an indication of the chemical reactivity of the surface. The decrease of the amount of oxygen on the surface shows that the oxygen from the oxide is dissolved into the bulk, making the surface metallic and therefore active.

### 3.3.6 X-Ray Diffraction

Crystalline structure and grain size are investigated by X-Ray Diffraction (XRD). This technique is based on the Bragg's law:

$$n\lambda = 2dsin\theta, \tag{3.31}$$

where $\lambda$ is the wavelength of the incident x-rays, $\theta$ is the Bragg's angle and $d$ the spacing between two parallel lattice planes, as can be seen in **Figure 3.18**.
For all the tested NEG samples the measurements have been performed in the $\theta - 2\theta$ configuration, which is the one shown in textbfFigure 3.18. The width of a given

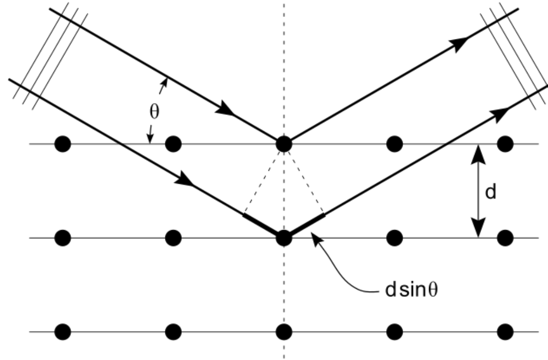


FIGURE 3.18: Representation of diffraction process.

diffraction peak is due mainly to the dimension of the coherently diffracting crystalline domains (crystallites) and to the imperfections of the crystal lattice[32]. There is, thus, a relation between the width of the peak and the grain size, that under the assumption of a single homogeneous phase can be described by the Scherrer equation:

$$\omega = \frac{k \cdot \lambda}{FWHM(2\theta) \cdot cos(\theta)}, \tag{3.32}$$

where $\theta$ is the measured diffraction angle, $FWHM(\theta)$ the peak broadening and $k$ is a constant named shape factor, which is related both to the way in which $\theta$ and $FWHM(\theta)$ are defined and to the crystallite shape and structure. This constant has been determined to vary between $0,89$ and $1,42$; for a crystal with a cubic crystalline structure and cubic geometric shape $k = 0,94$. The NEG sample can be approximate as crystal with a cubic crystalline structure and cubic geometric shape, therefore $k = 0,94$ has been used for the calculation.
The X-ray diffraction data have been recorded using a Siemens D500 diffractometer, whose x-ray source is $Cu\ K_\alpha$ ($\lambda = 154\ nm$). Usually $2\theta$ scans from 25°to 145°, with a step size of $0,01$°and a step duration of 3 $s$. The smallest grain size that can be evaluated precisely with this technique is 5 $nm$. Samples with this grain size are called nacrystalline.

Under the assumption that the film coating is made up of a single phase, the position of the diffraction peaks can be predicted using the Vegard's law; it states that the lattice parameter of solid solution is an average of the lattice parameters of the constituting elements weighted by the respective atomic concentration:

$$d_{TiZrHfV} = x_{Ti}d_{Ti} + x_{Zr}d_{Zr} + x_{Hf}d_{Hf} + x_V d_V, \tag{3.33}$$

where $d_i$ represents the distance between two lattice planes of the single elements in the chosen direction[3].

Known the lattice plane distance, the position of the NEG peak on the diffraction spectrum can be calculated using the Bragg relation:

$$\theta_{TiZrHfV} = arcsin\left(\frac{n\lambda}{2d_{TiZrHfV}}\right). \tag{3.34}$$

Comparing the predicted angle and the measured one, it can be seen that for the samples tested they do not differer too much, which it means that the assumption done are not far from the real situation for a NEG thin film.

[3]The NEG peak is calculated for a direction which is equivalent for the hpc and bcc lattices, using namely $< 002 >$ for elements with a hpc lattice and $< 110 >$ for bcc.

# Chapter 4

# Experimental Results

In the following chapter the main results obtained in two different campaigns are reported. The chapter is, thus, divided into two main sections: ageing campaign (**Section 4.1**) and coating campaign (**Section 4.2**).

## 4.1 Ageing Campaign

This campaign has been started in order to have a deeper knowledge of the effects that the tunnel air exposure has on the NEG coated vacuum chambers of the Long Straight Sections.

During the Long Shutdown 1 (LS1), started in February 2013, some of the NEG coated vacuum chambers were exposed to the air of the LHC tunnel because of maintenance. The re-activation of the NEG film presented problems in some cases; therefore it has been decided to study in details if the exposure to tunnel atmosphere for long periods affects the pumping properties of them.

Other shutdowns are planned at CERN therefore it is better to know in advance how to behave in front of the opening of the NEG coated vacuum chambers; there are two possibilities: leave them exposed to the air and change the ones damaged (if there will be) or put them under static vacuum during the maintenance operations. Both solutions have a costs; the costs of the first one is the cost of making new chambers to substitute those ruined, if any, the costs of the second solution is the one of sealed all the chambers with $N_2$ during maintenance.

If the present study will show that there are no serious damages to the pumping characteristics of the NEG coatings due to tunnel air exposure the first option will be taken into consideration as a possible solution.

### 4.1.1 Exposure Points

In order to evaluate the characteristics of the NEG thin film aging tests have been performed. Six stainless steel DN100 tubes have been coated together. The type of NEG coating and the coating technique are the standard used for coating the Long Straight Sections (LSS) of LHC: $Ti_{30}Zr_{30}V_{40}$ deposited with Magnetron Sputtering. All the tubes were cleaned before the coating with Net Inox.

TABLE 4.1: List of the samples with the respective point and duration of the exposure.

| Name of the sample | Point of exposure | Duration of the exposure |
|---|---|---|
| Reference | none | 0 month |
| LSS3_1 | Point 3 | 1 month |
| LSS3_2 | Point 3 | 3 months |
| LSS1_1 | Point 1 | 9 months |
| LSS1_2 | Point 1 | |
| $N_2$ sealed | none | none |

As **Table** 4.1 shows, one tube has been used as reference, therefore has been tested right after the NEG film deposition. Four tubes have been stocked in two different points of the LHC tunnel: two in Point 3 (near Crozet) and two in Point 1 (near Meyrin). The last tube was sealed with $N_2$ and stocked in the CERN laboratory where alle the measurements have been performed.

In **Figure** 4.1(a) it can be seen the position on the map of the two exposure points: *Point 1* is where the ATLAS experiment is located, meanwhile in *Point 3* there is a cleaning facility for the beam. **Figure** 4.1(b) shows the two chambers exposed in Point 3.

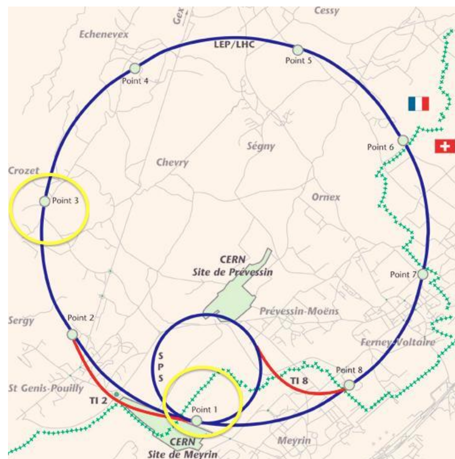


(a) Map of the LHC tunnel with the exposure points positions (yellow circles). It can be see that the ring lays both on swiss and french territory.

(b) Picture of the two chambers exposed in Point 3.

FIGURE 4.1: Exposure Points.

### 4.1.2 Bake-out/Activation Procedure

A bake-out/activation procedure has followed the exposure. All the sample have been put under vacuum as soon as they have been taken out of the tunnel in order to avoid contamination.
It has been decided to perform the same procedure used for the Long Straight Section according to [33].
The procedure is divided into two main parts: in the first part all the measurements system components are baked, meanwhile in the second part, when the degassing temperature is reached by the system, the sample is activated.

TABLE 4.2: Bake-out and Activation Procedure for the samples.

| | Step 1 | Step 2 | Step 3 |
|---|---|---|---|
| Ramp Rate [°C/ h] | 75 | 75 | 80 |
| Temperature [°C] | 120 | 230 | 20 |
| Duration [h] | 24 | 24 | 24 |

In **Table 4.2** the three steps of the sample heating procedure are reported; during **Step 1** the whole measuring system is baked in order to reach a vacuum level suitable for the pumping speed measurements in a reasonable time. Each part of the experimental system is therefore heated at a certain temperature depending on the component (the temperatures are between 350 °C and 150 °C) for a day in order to enhanced te desorption of all the contaminants entered in the system during the mounting operations. In the meantime the sample is kept at 120 °C in order to be sure that the NEG film is not activated.
An activation of the NEG coating follows the bake-out of the system (**Step 2**).
While the other part of the Fisher-Mommsen Dome reach the degassing temperature, the sample is heated at 230 °C for 24 $h$. Although the $Ti_{30}Zr_{30}V_{40}$ NEG coating have an official activation temperature of 180 °C, the standard procedure used for the LHC LSS choose a temperature higher in order to be sure that all the NEG coated parts are correctly activated.
The degas of the two hot cathodes gauges (30 $min$ for each gauge) used for the pumping speed measurement is performed at the end of the NEG activation (for all the details of the measurement procedure see **AppendixB**).
In **Figure 4.2(a)** the bake-out temperatures of all measurement system parts are reported. The temperatures and the time needed to reach these temperatures are chosen in order to not damage the various components, which are made with different materials. It can be clearly seen how the activation of the NEG thin film is delayed in respect to the bake-out and how it starts only when the degassing temperature is reached.
In **Figure 4.2(b)** the system pressure measured by the cold cathode gauge is shown

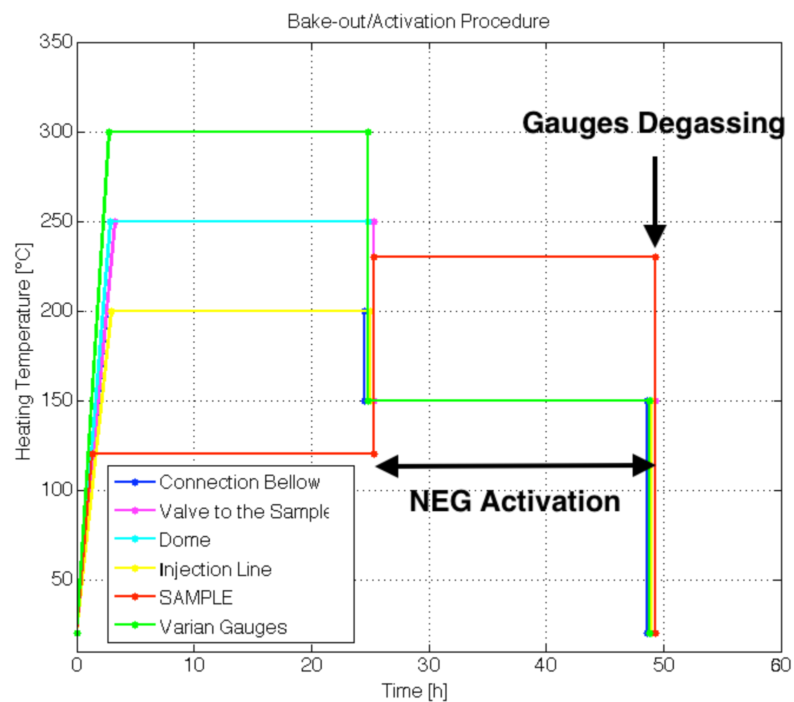


(a) Summary of the Bake-out/Activation procedure used for the ageing campaign. The temperatures of all the measuring system parts are reported.

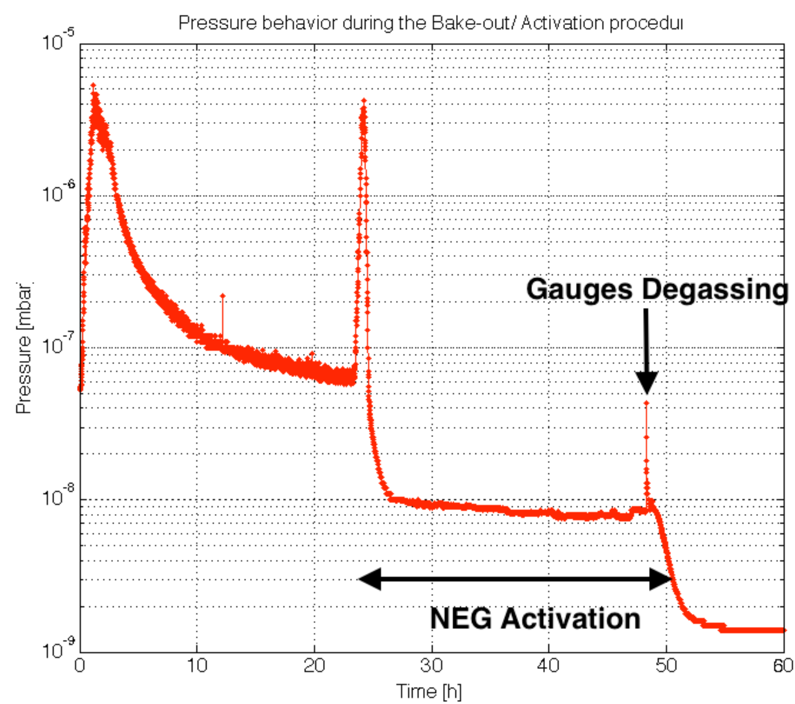


(b) System pressure during the whole Bake-out/Activation procedure as a function of time for sample LSS3_2.

FIGURE 4.2: Bake-out/Activation procedure.

during the whole heating procedure. The pressure increase during the initial part of the bake-out is due to the heating enhanced outgassing of the system metal walls. When the equilibrium between outgassing and the pumped gas quantity is reached the pressure starts to decrease. The second peak in the pressure appears when the NEG activation temperature is reached. The equilibrium, in this case, is reached faster because there is an increase of the total pumping speed of the system due to the fact the the NEG thin film, which coats the internal wall, of the sample starts pumping too. The last small bump in the pressure corresponds to the gauges degas.
Thanks to the bake-out and the added pumping speed the system reach a low pressure (typical values of the UHV range) in a short amount of time: lower $10^{-9}$ after the cool down in the shown case.

### 4.1.3 Experimental Results

For each sample the $H_2$ pumping speed and the number of $CO$ molecules needed to saturate the surface have been measured straight after the cool down. The measuring system is the Fisher-Mommsen dome illustrated in **Section 3.1.3**.
In **Table 4.3** all the results are reported.
Between sample **LSS3_2** and **LSS1_1** a calibration of the two system varian gauges have been performed; the calibration factors are reported in **Section 3.1.3**.

TABLE 4.3: Summary of the experimental results obtained.

| | $H_2$ Pumping Speed $[l \cdot s^{-1}]$ | | | CO Molecules | | |
|---|---|---|---|---|---|---|
| | I Act | II Act | Exp | I Act | II Act | Exp |
| **Reference Sample** | 381 | - | - | $8 \cdot 10^{17}$ | - | - |
| **LSS3_1** | – | 761 | 386 | - | $7 \cdot 10^{17}$ | $5 \cdot 10^{17}$ |
| **LSS3_2** | 395 | - | - | $1 \cdot 10^{18}$ | - | - |
| **LSS1_1** | 615 | - | 669 | $1 \cdot 10^{18}$ | - | - |
| **LSS1_1** | NOT TESTED | | | | | |
| $N_2$ **sealed** | NOT LEAK TIGHT | | | | | |

The **Reference** sample presents a hydrogen pumping speed of 381 $l \cdot s^{-1}$ and $8 \cdot 10^{17}$ CO molecules are needed for saturate the surface. These values have been taken as a reference for the pumping performances of the exposed chambers.

As can be seen from **Table 4.3** no hydrogen pumping speed have been measured for sample **LSS3_1**. The sample, exposed for one month to the atmosphere of Point 3, seems to have been damaged, since non pumping speed has been measured after the activation.
The sample has been activated a second time: it has been brought at 230 °C and heated

for 24 $h$ meanwhile the rest of the measuring system have been kept at room temperature. The hydrogen pumping speed measurement has followed the cool down. A pumping speed considerably higher than that of the reference has been measured : 761 $l \cdot s^{-1}$.

In order to crosscheck the results, a last measurement have been done. The sample has been vented for one night and put again under vacuum the morning after. The standard activation procedure has followed. The hydrogen pumping speed measured is close to the reference one; the air exposure may have affect the pumping properties of the sample.

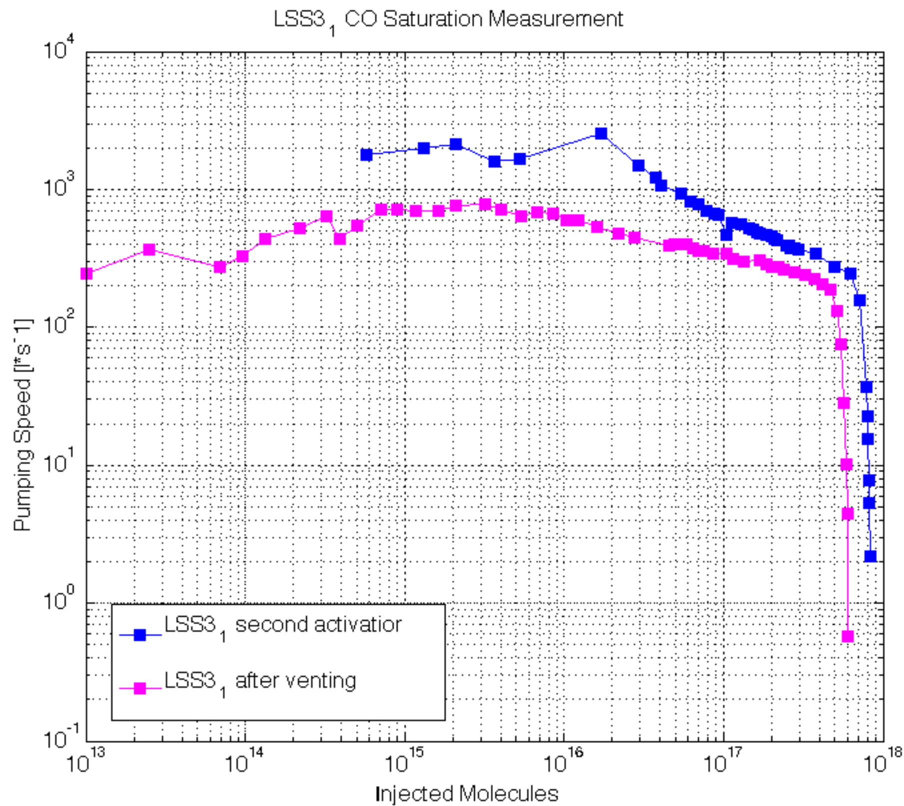


FIGURE 4.3: Comparison between the $CO$ saturation measurements performed on sample **LSS3_1** after the second activation (blu curve) and the air exposure (magenta curve).

In **Figure 4.3** a comparison between the $CO$ saturation measurements is shown: the $CO$ pumping speed is plotted ad a function of the number of CO molecules injected in the dome. The surface saturation occurs when there are no more free site on the film surface for capturing $CO$ molecules: the pumping speed for this gas show, therefore, an abrupt decrease, as can be clearly seen from **Figure 4.3**. It seem that the air exposure has not affected too much the surface capacity for $CO$. A small decrease in the number of molecules needed for saturate the surface is expected

After 3 months of exposure to the LHC tunnel atmosphere **LSS3_2** have been tested. Both the hydrogen pumping speed and the $CO$ molecules for the surface saturation are close to the values measured for the reference; therefore the sample has not been activated a second time.

Sample **LSS1_1** has been tested after 9 months of exposure. Problems during the activation have been observed; in particular the heating system has not been stable and able to reach the 230 °C, as can been seen from the pressure behavior during the bake-out/activation procedure (**Figure 4.4**):

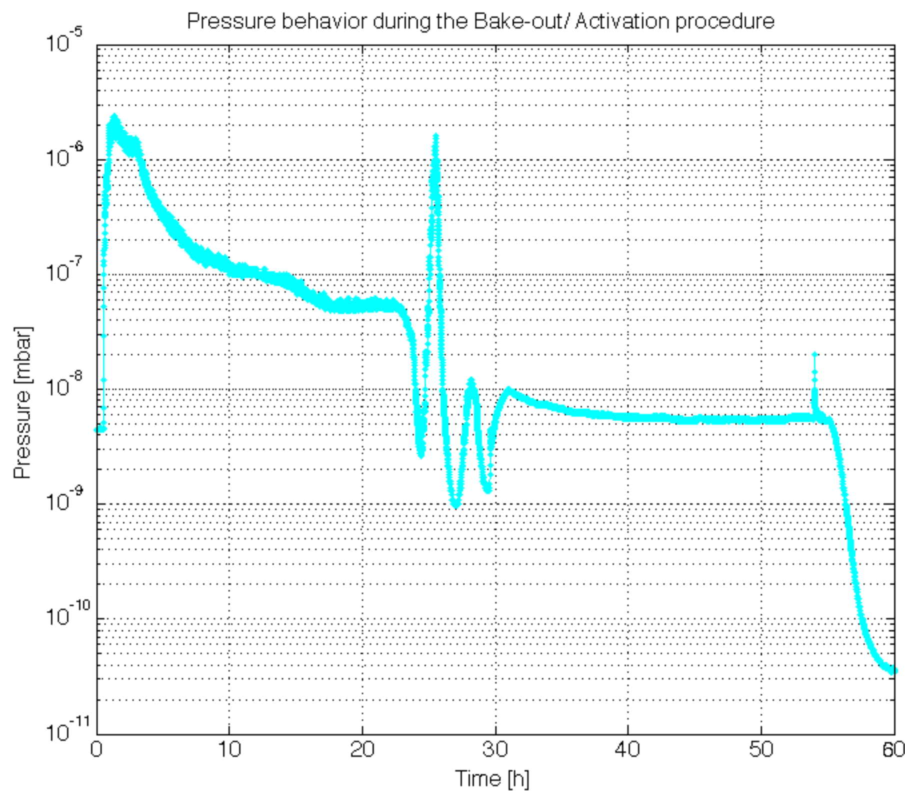


FIGURE 4.4: Pressure during the bake-out/activation procedure of sample **LSS1_1**.

Right after the end of **Step 1** the heating system has switched off. It has been not possible to reach the activation temperature using a heating ramp, therefore the sample was brought at 230 °C increasing manually the temperature: 180 °C for 50 *min*, then 230 °C for 24 *h*.
The hydrogen pumping speed measured is higher than the reference one, meanwhile the $CO$ molecules does not differ from the reference one, as can be seen in **Table 4.3**.
It has been decided to activate a second time the sample after a night of exposure in the laboratory, in order to check the hydrogen pumping speed. After the standard

bake-out/activation procedure a pumping speed closer to the one measured in the first activation: 669 $l \cdot s^{-1}$ in the first case, 615 $l \cdot s^{-1}$ in the second.

## 4.2 Coating Campaign

The coating campaign has been started at CERN in order study the remaining materials of the $IV$ and $V$ groups. An alloy with vacuum properties close to $Ti_{30}Zr_{30}V_{40}$ and maybe lower activation temperature is searched. The types of alloys tested have been chosen considering the results obtained for the $TiZrV$ alloys: since the $V$ presence is needed in order to lower the activation temperature of the $IV$ group elements (see **Chapter 2**), the $ZrV$ and the $HfV$ alloys have been studied. Preliminary studies done on $TiV$ indicate that this alloys does not present good qualities (see **Figures 2.6(a)** and **2.6(b)**), thus further studies have not been made. A quaternary alloy composed by all the $IV$ group elements with the addition of $V$ have been studied too.
In the present work the results obtained for the following alloys are reported:

- $ZrV$ Campaign (4.2.2);
- $HfV$ Campaign (4.2.3);
- $TiZrHfV$ Campaign (4.2.4).

The results obtained are always compared with a reference sample of $TiZrV$.
Samples have been prepared coating DN100 stainless steel tunbes 50 cm long with magnetron sputtering. The cathodes used are braids of the single elements wires (see **Figure 3.7**); the composition of the films have been changed using wires with different diameter or more wires of the same material. The coating parameters used are the same for all the samples and are reported in **Table 4.4**:

TABLE 4.4: Coating parameters.

| | |
|---|---|
| Discharge Gas | $Kr$ |
| Gas Pressure | $4,5 \cdot 10^{-3}$ $Torr$ |
| Solenoid Current | $\sim 100$ $A$ |
| Solenoid Potential | $\sim 40$ $V$ |
| Cathode Potential | $-600$ $V$ |
| Cathode Power | $0,1$ $kW$ (DC) |
| Cathode Current | $0,2$ $A$ |
| Chamber Coating Temperature | 100 °C |

The time need for growing a 1 $\mu m$ thick film of non-evaporable getter material on the

stainless steel chambers depends of the sputtering yield; depending on the sputtered materials a coating can, therefore, lasts between 6 and 9 $h$.

In the following of the section the main results obtained in the coating campaign are reported. The measurements performed on each sample are those listed in **Section ??**. More than 30 samples have been realized: after a brief presentation of all of them, only the most interesting will be discussed in details. In particular, it has been decided to show with some significant examples how the vanadium presence affect the alloys properties. For the discussion of the results see **Chapter 5**.

### 4.2.1 Reference Sample: $Ti_{29}Zr_{31}V_{40}$

At the beginning of the coating campaign a DN100 stainless steel chamber has been coated with a standard $TiZrV$ thin film, in order to have a reference sample for the comparison.
The characteristics of the cathode used are reported in **Table 4.5**; one wire of 3 $mm$ diameter for each element have been used for the sputtering.

TABLE 4.5: $Ti_{29}Zr_{31}V_{40}$ cathode composition.

| Material | Diameter [mm] | Number of wires |
|---|---|---|
| Ti | 3 | 1 |
| Zr | 3 | 1 |
| Hf | - | - |
| V | 3 | 1 |

It has been expected to have an atomic percentage of the three elements in the alloy equal to 30 % for $Ti$ and $Zr$ and 40 % for $V$, as is reported in **Table 4.6**. The composition has been checked by EDS, for the bulk, and XPS for the surface; it is close to the expected values for all the elements. The thickness of the film has been measured with

TABLE 4.6: Composition of the coating in atomic percentage.

| | Ti | | Zr | | Hf | | V | |
|---|---|---|---|---|---|---|---|---|
| | Bulk | Surface | Bulk | Surface | Bulk | Surface | Bulk | Surface |
| Predicted | 30 | - | 30 | - | - | - | 40 | - |
| Measured | 29 | 27 | 31 | 42 | - | - | 39 | 26 |

SEM and it is reported in **Table 4.7**; it is the average of 8 measurements. As explained in **Chapter 3**, two samples have been tested; it can be seen from the results that the film is not uniform, since its thickness changes a lot from spot to spot. In **Figure 4.5** an imagine of one of the film profile used for the thickness measurement, is shown; it is possible to see both the film and the copper substrate.

TABLE 4.7: Coating thickness.

| | | |
|---|---|---|
| Predicted [nm] | | 1000 |
| Measured [nm] | Bottom | $1446 \pm 73$ |
| | Top | $479 \pm 37$ |

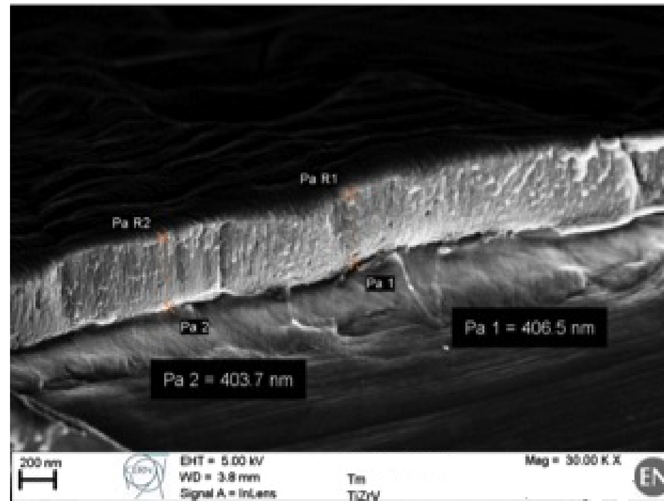


FIGURE 4.5: SEM profile of $Ti_{29}Zr_{31}V_{40}$ top: scale 200 $nm$, EHT 5 $kV$ and magnification 30 K X.

**Figure 4.6** shows SEM imagines of the film surface morphology; for the top and the bottom samples it is formed by closely packed grains with nanometric sizes, but it seem that the top sample (**Figure 4.6(a)**) has finer grains than the bottom one (**Figure 4.10(b)**). In this last figure can also be clearly seen the cauliflower morphology typical of $TiZrV$, meanwhile the film in **Figure 4.6(a)** appears more uniform. The difference between the two surfaces are due to the plasma characteristic during the coating: it could be that during the deposition the plasma has not been uniform along the coating tower.

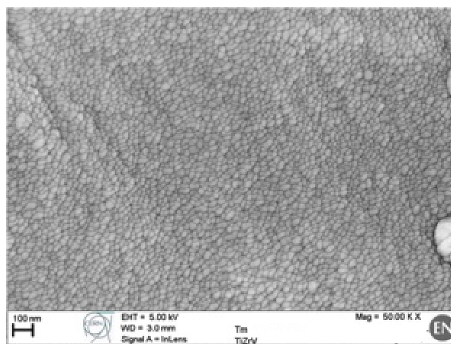

(a) SEM imagine of $Ti_{29}Zr_{31}V_{40}$ top surface: scale 200 $nm$, EHT 5 $kV$ and magnification 50 K X.

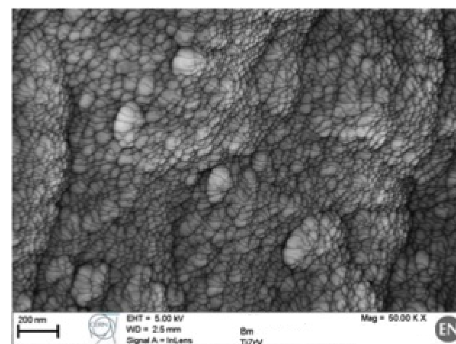

(b) SEM imagine of $Ti_{29}Zr_{31}V_{40}$ bottom surface: scale 200 $nm$, EHT 5 $kV$ and magnification 50 K X.

FIGURE 4.6: SEM imagines of $Ti_{29}Zr_{31}V_{40}$.

The grain dimension measured by the XRD is 2 $nm$ (calculated as explained in **Chapter 3**), which means that the film can be considered nano-crystalline[5]. In **Figure 4.7** the XRD spectrum is reported; the diffraction peak due to the NEG crystalline structure can be clearly seen at a Bragg's angles of 39°. The peak broadening suggests that the film crystalline domains are small.

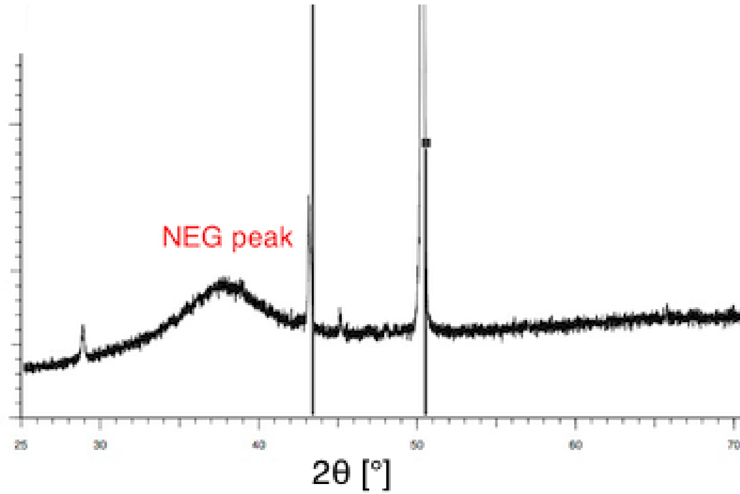


FIGURE 4.7: Not smoothened XRD spectrum of $Ti_{29}Zr_{31}V_{40}$: $Cu$ K$\alpha$ source, 2$\Theta$ from 25°to 145°, step size $0,01$°, step lasting 3 $s$.

The presence of a huge number of crystallites in the film increases the grain boundaries with a positive effect on the activation temperature: the oxygen diffusion, which at low temperature occurs mainly at the grain boundaries, is enhanced. It can be expected that the sample has a low activation temperature. This expectation is confirmed by the XPS, the SP and the ESD measurements.

Sample $Ti_{29}Zr_{31}V_{40}$ is very close to fulfill the CERN requirements for a good activation behavior. It shows a decrease in the $O1s$ area during the XPS heating cycle around the 72 %, but the decrease in the $C1s$ is well below the typical value of 50 %. Carbon on the as received sample is 28 % so within the acceptance limit of 40 %. The carbon transformation into carbide, whereas, is just below the limit of 40 %: it is 38 %.

In **Figure 4.8** the measurements performed for testing the vacuum properties of sample $Ti_{29}Zr_{31}V_{40}$ are shown, meanwhile the results are summarized in **Table 4.8** .

TABLE 4.8: Sticking factor for $H_2$ and $CO$ and variation of the total pressure afte the electron bombardment for sample $Ti_{29}Zr_{31}V_{40}$.

| Temperature [°C] | $\alpha$ $H_2$ | $\alpha$ $CO$ | $\Delta P_{SVT}$ [Torr] |
|---|---|---|---|
| 120 | $1 \cdot 10^{-4}$ | $1 \cdot 10^{-4}$ | $5.7 \cdot 10^{-7}$ |
| 160 | $1.4 \cdot 10^{-4}$ | $7.7 \cdot 10^{-3}$ | $4.0 \cdot 10^{-8}$ |
| 200 | $1.1 \cdot 10^{-2}$ | $5.6 \cdot 10^{-1}$ | $3.4 \cdot 10^{-10}$ |
| 250 | $2.4 \cdot 10^{-2}$ | 1 | $3.4 \cdot 10^{-10}$ |
| 300 | $3.6 \cdot 10^{-2}$ | 1 | $6.6 \cdot 10^{-10}$ |

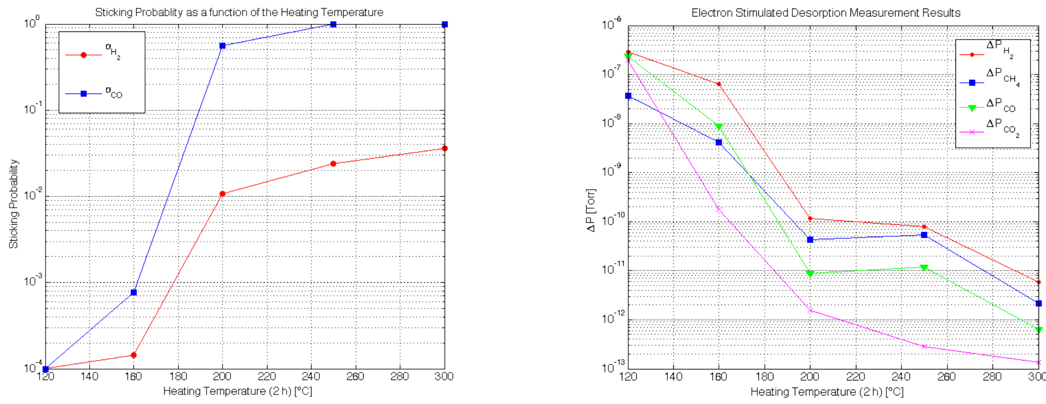


(a) Sample $Ti_{29}Zr_{31}V_{40}$ sticking probability for $H_2$ and $CO$ as a function of the heating temperature; each heating steps last 2 $h$.

(b) Sample $Ti_{29}Zr_{31}V_{40}$ pressure difference before and after electron bombardment as a function of the heating temperature; each heating steps last 2 $h$, whereas the bombardment lasts 100 $s$. The applied voltage is 500 $V$ and a current through the electron source is 1 $mA$.

FIGURE 4.8: Sticking probability and ESD measurements for $Ti_{29}Zr_{31}V_{40}$.

It can be seen from **Figure 4.8(a)** the difference between the $CO$ and $H_2$ sticking probability, already discussed in **Section 2.4**: the $H_2$ sticking probability is about two orders of magnitude lower than the $CO$ sticking probability. For both gases the first signs of activation are present after only two hours of heating at 160 °C. In **Figure 4.8(b)** the variation of the partial pressure during the electron bombardment is shown as a function of the heating temperature. This measurement confirms the results of the sticking probability measurements since the decreasing in the pressure variation is evident already after two hours of hating at 160 °C. The gas with biggest pressure variation decrease is $CO_2$; looking at the RGA data it can be noticed that its partial pressure after electron bombardment change a lot between 120 °C and 160 °C: $4,3 \cdot 10^{-8}$ $Torr$ at the first temperature and $5,7 \cdot 10^{-11}$ $Torr$. No other gas shows such a pressure decrease after the bombardment.
The activation temperature is conventionally defined as the temperature at which the total pressure variation after electron bombardment is equal to $10^{-10}$ $Torr$[5]. Therefore, in the case of sample $Ti_{29}Zr_{31}V_{40}$ the activation temperature is between 160 °C and 200 °C. It is a sample with a low activation temperature, as it is expected looking at its grain dimension.

In the following section the results obtain for $Ti_{29}Zr_{31}V_{40}$ will be used as reference for the other non-evporable getter materials tested.

### 4.2.2 $ZrV$ Campaign

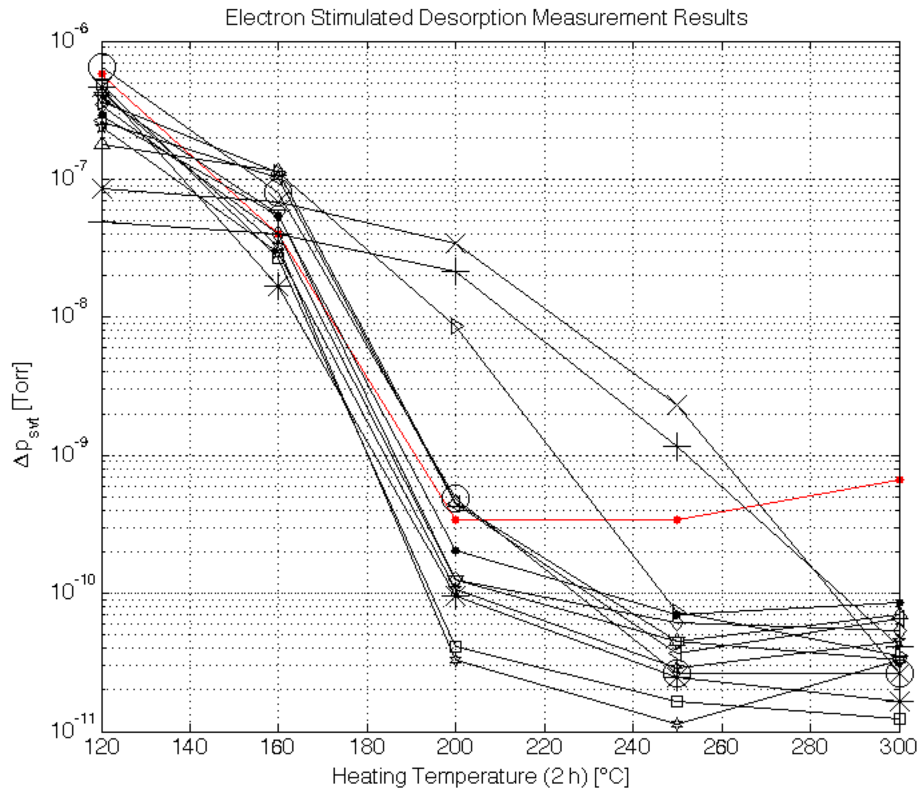


FIGURE 4.9: Results of the ESD measurements performed with an applied voltage of 500 $V$ and a current through the electron source of 1 $mA$ for the $ZrV$ samples tested.

13 samples of $ZrV$ with different composition have been tested so far; the aim of the campaign is finding the compositions with good vacuum properties. In particular, the knowledge acquired with $TiZrV$ alloys suggests that adding a certain amount of $V$ to a $IV$ group elements may help to lower the activation temperature. Therefore, samples with increasing atomic percentages of this element have been realized and tested.
All the samples have been prepared with magnetron sputtering on DN100 stainless steel tubes of 50 $cm$ length and characterized as previously explained.
In **Figure 4.9** the variation of the total pressure after the electron bombardment is shown as a function of the heating temperature for all the samples; the ESD results are compared with the one obtained for $Ti_{29}Zr_{31}V_{40}$ (red curve in the figure). It can be noticed that for some samples the pressure variation is less than the one for the reference, for others is higher only for high temperature (higher than 200 °C), meanwhile few samples show a behavior close to $Ti_{29}Zr_{31}V_{40}$, and even some case even better
In the following the most significant samples are discussed in details.

If a very low atomic percentage of $V$ is added to $Zr$, the film obtained have characteristics close to the pure $Zr$. This is the case of $Zr_{91}V_9$, realized with a cathode composed by two wires: one of $Zr$ with a diameter of 6 $mm$ and the other of $V$ with a diameter of 1 $mm$.

The grain dimension, according to the XRD measurement, is 46 $nm$, therefore the film cannot be considered nano-crystalline (dimension lower than 5 $nm$). The crystallites composing the film can be observed in the SEM imagines reported in **Figure 4.10(a)**

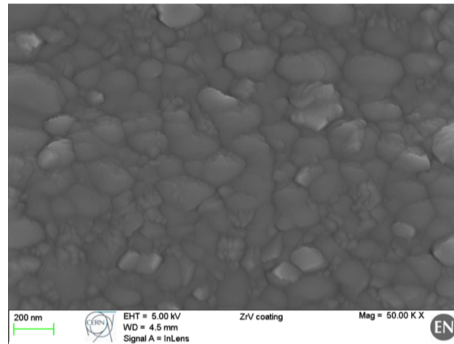


(a) SEM imagine of $Zr_{91}V_9$ surface: scale 200 $nm$, EHT 5 $kV$ and magnification 50 K X.

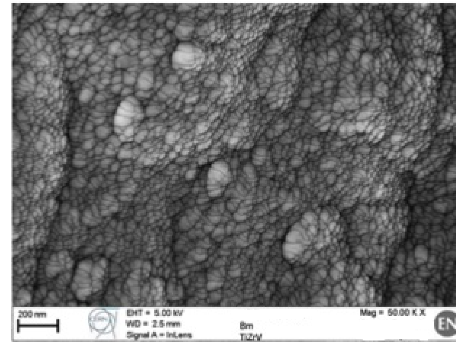


(b) SEM imagine of $Ti_{29}Zr_{31}V_{40}$ surface: scale 200 $nm$, EHT 5 $kV$ and magnification 50 K X.

FIGURE 4.10: Surface morphology of $Zr_{91}V_9$ and $Ti_{29}Zr_{31}V_{40}$.

Looking at the surface morphology of $Zr_{99}V_9$, big compact grains can be distinguished. With such big grains it is expected a high activation temperature since the grain boundaries are few. The sample surface, moreover, is not rough as the $Ti_{29}Zr_{31}V_{40}$, shows in **Figure 4.10**, therefore not satisfying pumping properties are expected.

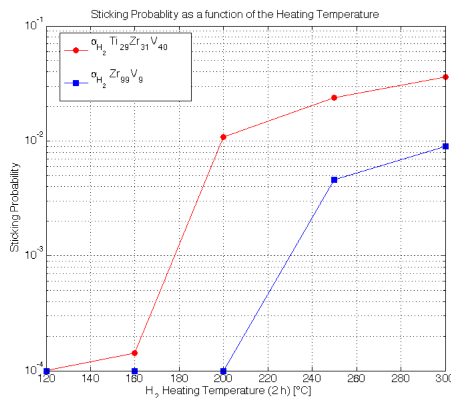


(a) Comparison between the $H_2$ sticking probability of $Zr_{99}V_9$ (blu squares) and $Ti_{29}Zr_{31}V_{40}$ (red dots).

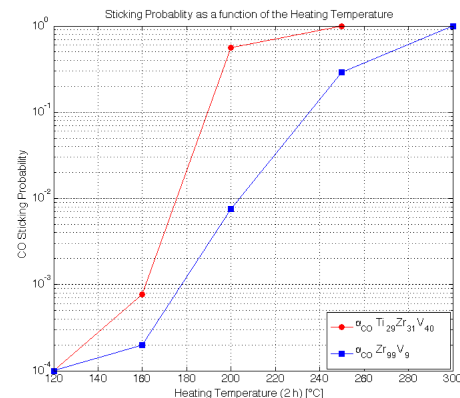


(b) Comparison between the $CO$ sticking probability of $Zr_{99}V_9$ (blu squares) and $Ti_{29}Zr_{31}V_{40}$ (red dots).

FIGURE 4.11: Comparison between the $H_2$ and $CO$ sticking probability of sample $Zr_{99}V_9$ and $Ti_{29}Zr_{31}V_{40}$.

The expectation is confirmed by both sticking probabilities and ESD measurements; it

can be clearly seen from **Figures 4.11** that the sticking probability both for $H_2$ (**Figure 4.11(a)**) and $CO$ (Figure **4.11(b)**) is lower than the one of $Ti_{29}Zr_{31}V_{40}$ (red dots in both plots) for all the heating temperatures. In particular, $Zr_{99}V_9$ does not pump $H_2$ for low temperatures, which it means that its surface is not reactive enough.

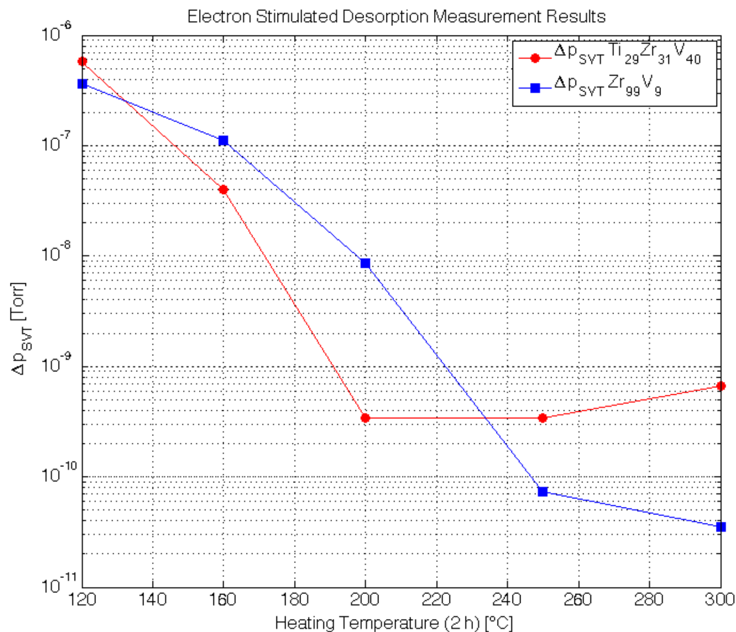


FIGURE 4.12: Results of the ESD measurements performed with an applied voltage of 500 $V$ and a current through the electron source of 1 $mA$ for $Zr_{99}V_9$ (blu squares) compared with $Ti_{29}Zr_{31}V_{40}$ (red dots).

In **Figure 4.12** the ESD results are shown and compared to the one for the reference sample. $Zr_{99}V_9$ variation of total pressure (blue squares) is smaller than the reference one for low temperature, meanwhile becomes comparable for higher ones; this is an indication that the sample surface is not activated until higher temperature are reached: it has the same behavior of pure $Zr$, which is fully activated only at 300 °C.
XPS measurement confirms the fact that $Zr_{99}V_9$ activation begins after 200 °C and is not completed at 250 °C. The decrease in the $O1s$ area is only 28% and also the reduction of carbon into carbide is bad.

A completely different film can be obtained increasing the content of $V$ in the alloy. Three samples have been prepared using a cathode composed by a $Zr$ wire with a 3 $mm$ diameter and a $V$ wire with a 1 $mm$ diameter, in order to have a film with a vanadium atomic percentage around 30%. The samples obtained have properties very close to $Ti_{29}Zr_{31}V_{40}$, as can be seen from the sticking probability measurements shown in **Figure 4.13**. Looking at the sticking probabilities as a function of the heating temperature reported in **Figure 4.13(a)** for $H_2$ and in **4.13(b)** for $CO$, it seems that they

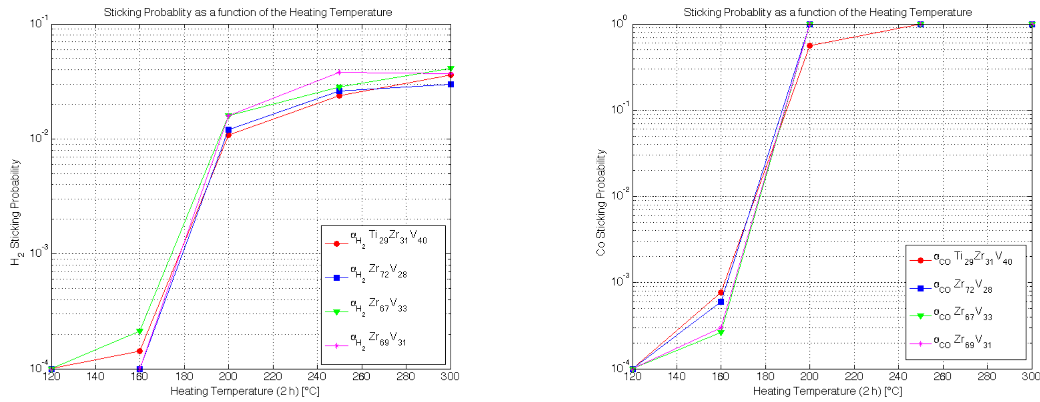


(a) Comparison between the $H_2$ sticking probability of $Zr_{72}V_{28}$ (blu squares), $Zr_{67}V_{33}$ (green triangles), $Zr_{69}V_{31}$ (magenta stars) and $Ti_{29}Zr_{31}V_{40}$ (red dots).

(b) Comparison between the $CO$ sticking probability of $Zr_{72}V_{28}$ (blu squares), $Zr_{68}V_{32}$ (green triangles), $Zr_{69}V_{31}$ (magenta stars) and $Ti_{29}Zr_{31}V_{40}$ (red dots).

FIGURE 4.13: Comparison between the $H_2$ and $CO$ sticking probability of sample $Zr_{72}V_{28}$, $Zr_{68}V_{32}$, $Zr_{69}V_{31}$ (magenta stars) and $Ti_{29}Zr_{31}V_{40}$.

start their activation already after 2 $h$ of heating at 160 °C, result confirmed also by the XPS measurements; for both samples the reduction of $Zr$ and $V$ begins at 160 °C and is fully completed at 200 °C, where the peaks of these elements own only the metallic component.

The oxygen diffusion process start at low temperature since the grain dimensions for both samples is small enough to enhance the diffusion through the grain boundaries. From the XRD spectra a grain size of 4 $nm$ has been calculated for $Zr_{72}V_{28}$ and of 3 $nm$ for $Zr_{67}V_{33}$, meanwhile for $Zr_{69}V_{31}$ no NEG peak has been individuated on the spectrum.

In **Figure 4.14** the ESD results for the two samples are reported and compared with the results for the reference sample. At low temperature the three films have the same behavior: the total pressure variation after electron bombardment starts decreasing at 160 °C, which means that the surfaces are cleaner from the oxide layer already at that temperature.

The good pumping properties are linked to the very rough surface of the samples, which are shown in **Figure 4.15**. The surface morphology of both samples presents small and compact crystalline domains; such a rough surface increase the area available for reacting with the gas molecules (high pumping surface). $Zr_{68}V_{32}$ presents also characteristic parallel lines on its surface, as can be observed in **Figure 4.15(b)**.

Increasing too much the percentage of vanadium inside the $ZrV$ alloy causes the worsening of its pumping properties. This is the case of $Zr_{12}V_{88}$ and $Zr_{13}V_{87}$, realized with the same cathode ($Zr$ wire with 1 $mm$ diameter and $V$ wire with 3 $mm$ diameter). The

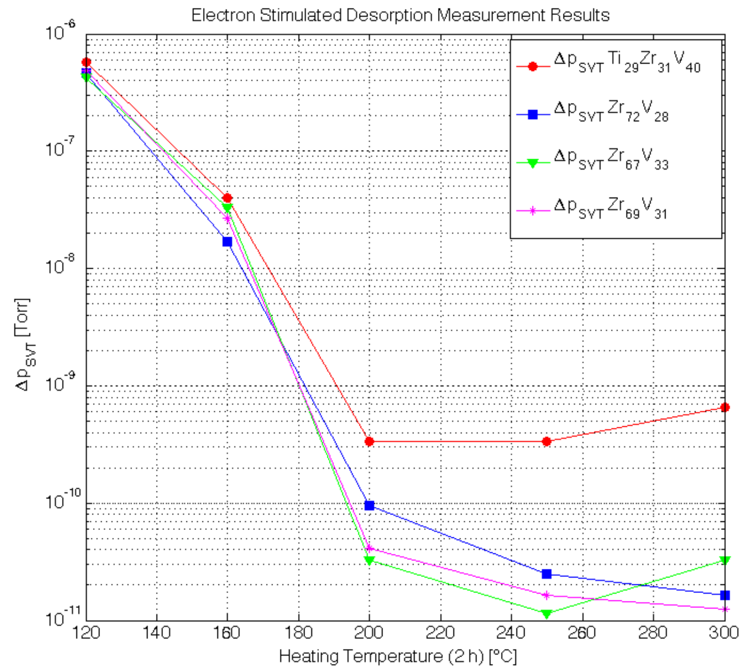


Figure 4.14: Results of the ESD measurements performed with an applied voltage of 500 $V$ and a current through the electron source of 1 $mA$ for $Zr_{72}V_{28}$ (blu squares) and $Zr_{68}V_{32}$ (green triangles), $Zr_{69}V_{31}$ (magenta stars) compared with $Ti_{29}Zr_{31}V_{40}$ (red dots).

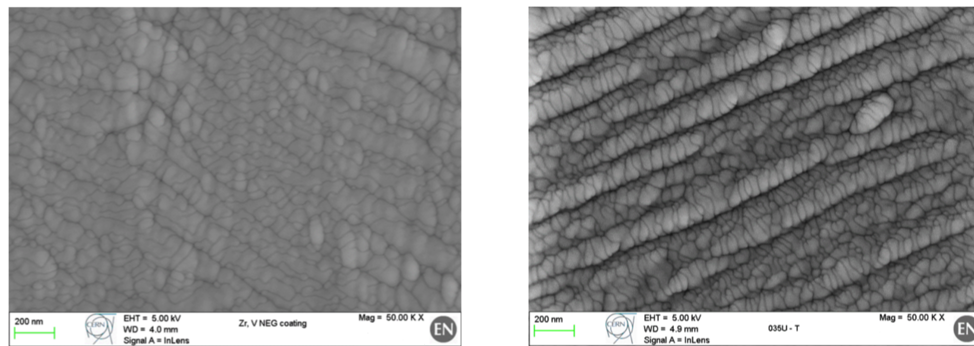


(a) SEM imagine of $Zr_{72}V_{28}$ surface: scale 200 $nm$, EHT 5 $kV$ and magnification 50 K X.

(b) SEM imagine of $Zr_{68}V_{32}$ surface: scale 200 $nm$, EHT 5 $kV$ and magnification 50 K X.

Figure 4.15: Surface morphology of $Zr_{72}V_{28}$ and $Zr_{67}V_{33}$.

properties of these two films are close to the one of vanadium.

The grain dimension is 28 $nm$ for $Zr_{12}V_{88}$ and 25 $nm$ for $Zr_{36}V_{64}$, therefore the films cannot be considered nano-crystalline like $Ti_{29}Zr_{31}V_{40}$. Their big grains do not help the diffusion process, so a high activation temperature is expected.

The XPS measurement confirms the expectation; for both samples the conversion of carbon into carbide takes place but is bad (8% for $Zr_{12}V_{88}$ and 24% for $Zr_{36}V_{64}$). No

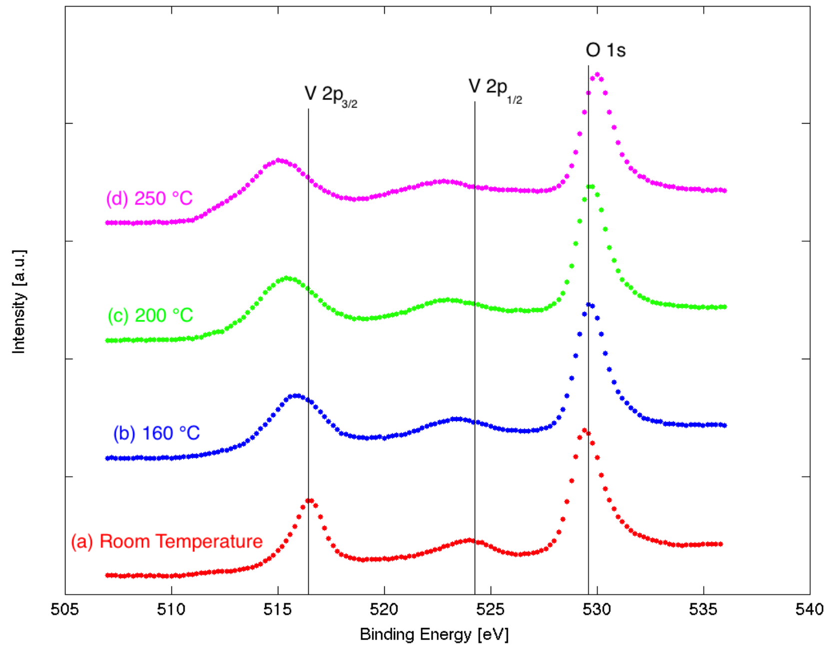


FIGURE 4.16: Comparison between the XPS spectra of $Zr_{12}V_{88}$ for all the heating temperatures (photon energy $1253,6\ eV$, time per step $50\ s$, sweep 16.)

decrease of the O1$s$ area can be observed (an example can be seen for $Zr_{12}V_{88}$ in **Figure 4.16**) in both cases. Moreover for all the heating temperatures for both $Zr$ and $V$ the metallic component in theirs XPS peaks does not appear. This fact can be clearly observed in **Figure 4.16**, where the spectra for $Zr_{12}V_{88}$ are reported; the $V2p$ peaks are not shifted at lower binding energy for none of the heating temperatures tested. This element present on the sample surface changes its oxidation state, since a little shift in the peaks can be noticed, but do not reach the metallic state ($V2p_{3/2}$ binding energy for the metallic state is 512 $eV$, meanwhile for $V2p_{1/2}$ is 520 $eV$). It can be concluded that the vanadium into the film is not reduced for any temperature (the activation does not take place). The same can be said for $Zr$.
As can be seen in **Figure 4.17** the coated samples seem not be able to pump neither $H_2$ nor $CO$ until the heating temperature is higher than 200 °C: both the sticking probabilities are negligible until high activation temperatures are reached. **Figure 4.15**.
The poor pumping properties shown by the two tested samples can be blamed to the smooth surfaces, shown in **Figure 4.18**. The morphologies are completely different form the reference sample: looking at the SEM imagines it is not possible to individuate the cauliflower structure typical of $TiZrV$. Large and elongated grains can be observed on samples surface. For $Zr_{13}V_{87}$ the grains appear compact and uniformly distributed on the substrate (**Figure 4.18(b)**), meanwhile $Zr_{12}V_{88}$ shows more irregularities; in **Figure 4.18(a)** smooth areas and compact grains arrangement are present.

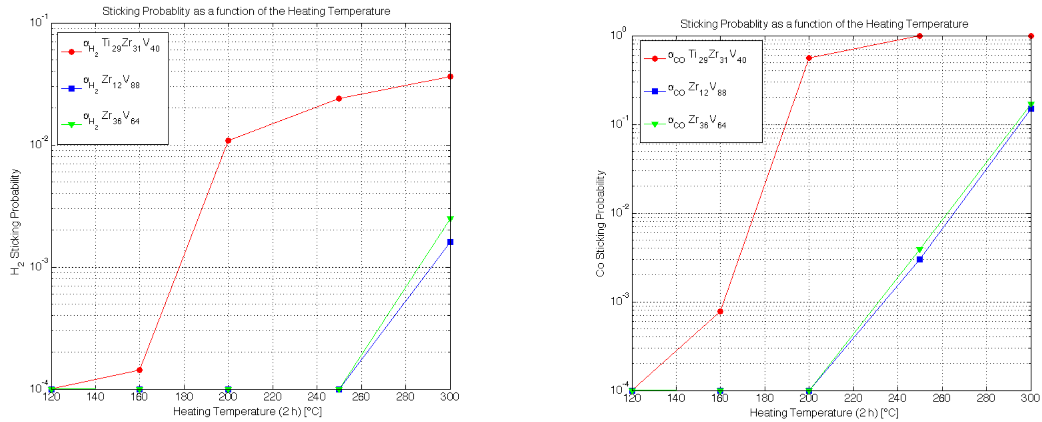


(a) Comparison between the $H_2$ sticking probability of $Zr_{12}V_{88}$ (blu squares), $Zr_{36}V_{64}$ (green triangles) and $Ti_{29}Zr_{31}V_{40}$ (red dots).

(b) Comparison between the $CO$ sticking probability of $Zr_{12}V_{88}$ (blu squares), $Zr_{36}V_{64}$ (green triangles) and $Ti_{29}Zr_{31}V_{40}$ (red dots).

FIGURE 4.17: Comparison between the $H_2$ and $CO$ sticking probability of sample $Zr_{12}V_{88}$, $Zr_{36}V_{64}$ and $Ti_{29}Zr_{31}V_{40}$.

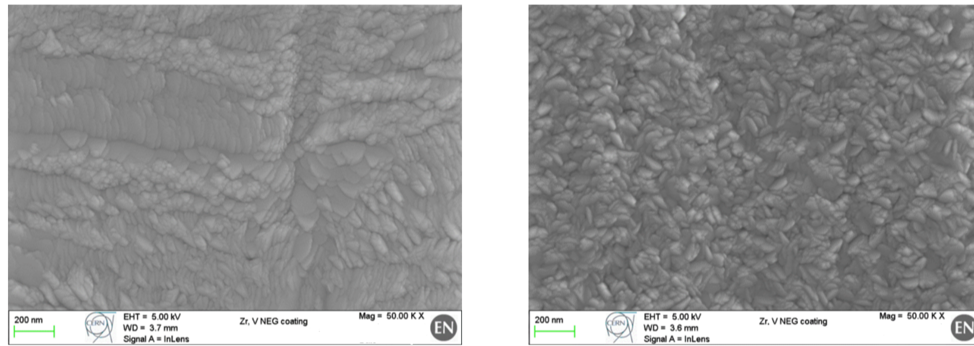


(a) SEM imagine of $Zr_{12}V_{88}$ surface: scale 200 $nm$, EHT 5 $kV$ and magnification 50 K X.

(b) SEM imagine of $Zr_{13}V_{87}$ surface: scale 200 $nm$, EHT 5 $kV$ and magnification 50 K X.

FIGURE 4.18: Surface morphology of $Zr_{12}V_{88}$ and $Zr_{13}V_{87}$.

### 4.2.3 $HfV$ Campaign

11 samples of $HfV$ with different composition have been tested so far. As already explained, for this getter material too the goal is finding a suitable composition for vacuum application in particle accelerators; therefore, it is searched an alloy with low activation temperature and good pumping properties, comparable withe the standard $TiZrV$ NEG thin film coating.

As can be already guessed looking at the ESD results for all the samples tasted in **Figure 4.19**, $HfV$ alloys have higher activation temperatures than reference film $Ti_{29}Zr_{31}V_{40}$ (red dots in the figure), since the total pressure variation for low heating temperatures (not higher than 200 °C) is never lower than $10^{-9}$ $Torr$; only few samples the $10^{-10}$ $Torr$ are reached after two hours of heating at 200 °C.

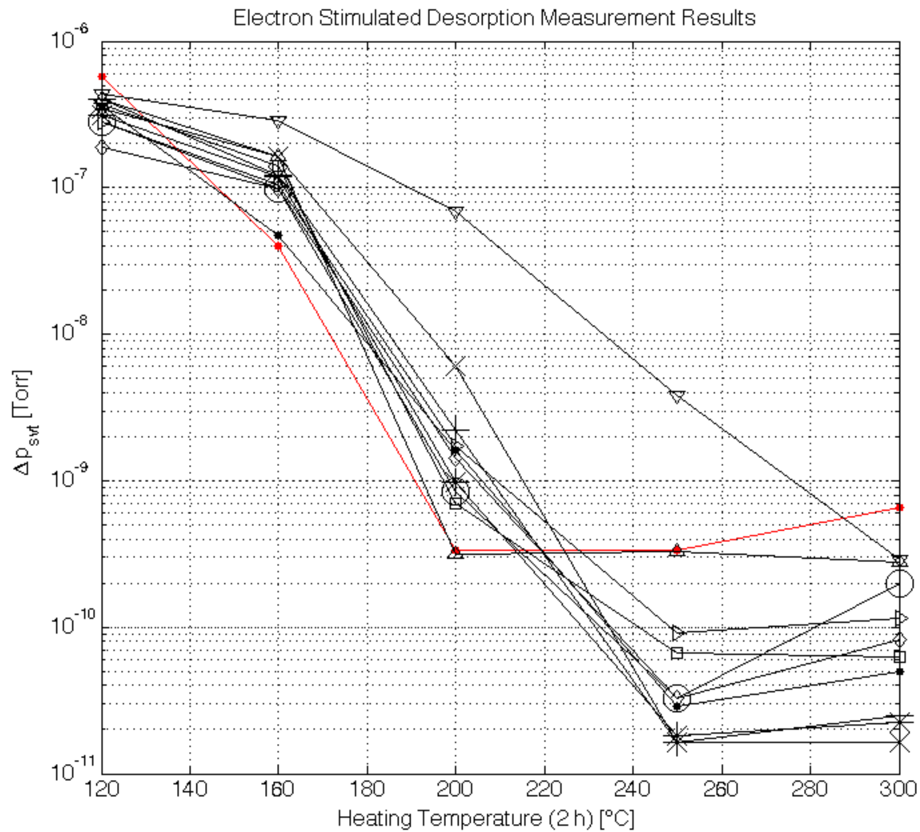


FIGURE 4.19: Results of the ESD measurements performed with an applied voltage of 500 $V$ and a current through the electron source of 1 $mA$ for the $HfV$ samples tested.

All the samples have been prepared with magnetron sputtering on DN100 stainless steel tubes of 50 $cm$ length and characterized as previously explained. As it have been done for $ZrV$, tubes have been coated with $Hf$ thin film with an increasing percentage of $V$, in order to investigate the effects causes by its adding.
In the following the most significant samples are discussed in details.

A very low percentage of $V$ added to a $Hf$ thin film does not help to lower the activation temperature of this element. A thin film coating of $Hf_{95}V_5$, prepared with a cathode composed by two wires, one of $Hf$ (2 $mm$ diameter) and one of $V$ (0, 5 $mm$ diameter), has been tested.
In **Figure 4.20** some details of the XPS spectra at all the heating temperatures are shown. In particular, **Figure 4.20(a)** shows the two $4f$ peaks of $Hf$, meanwhile **Figure 4.20(b)** the two $2p$ peaks of $V$ and the $O1s$ peak. $Hf$ does not present signs of reduction, since its peaks are not shifted at lower binding energy with the increase of the heating temperature. $V$, instead, is partially reduced at 250 °C, as can be seen looking at the $2p_{3/2}$ peak moves to the left. The counts for $V$ are very low since its percentage

in the film is only 5%. The decrease of $O1s$ area is below the requirements (12% where

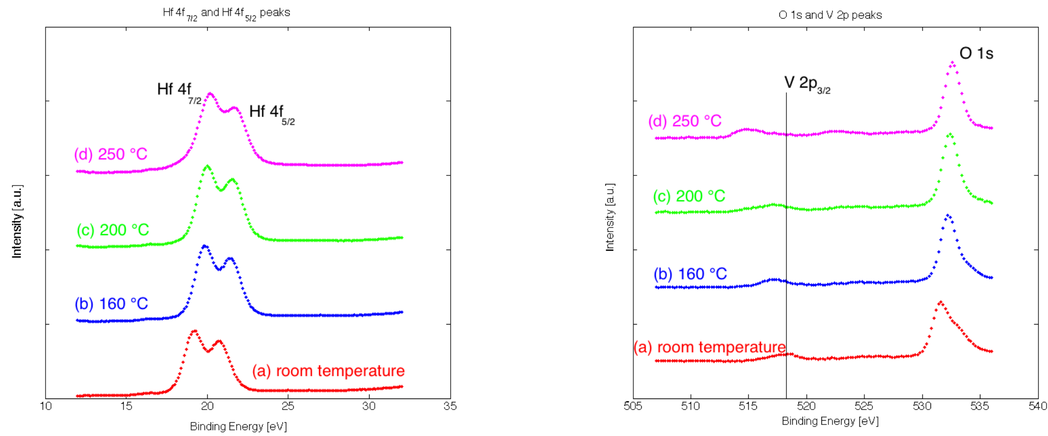


(a) $Hf4f_{7/2}$ and $Hf4f_{5/2}$ peaks of $Hf_{95}V_5$ for all the heating temperature (photon energy 1253, 6 $eV$, time per step 50 $s$, sweeps 20.)

(b) $V2p_{3/2}$, $V2p_{1/2}$ and $O1s$ peaks of $Hf_{95}V_5$ for all the heating temperature (photon energy 1253, 6 $eV$, time per step 50 $s$, sweeps 20.)

FIGURE 4.20: Details of $Hf_{95}V_5$ XPS spectrum:

the 66% is the acceptance limit) and the carbon conversion into carbide is bad as well. The calculated grain dimension is 18 $nm$, which means that $Hf_{95}V_5$ is not nanocrystalline. Comparing the XPS and the XRD results, it can be concluded that the relation between the grain dimension and the activation temperature is verified also for this sample: only films with crystallites dimension smaller than 5 $nm$ own an activation temperature lower than 200 °C.

In **Figure 4.21** a comparison between the surface morphology of $Hf_{95}V_5$ and $Ti_{29}Zr_{31}V_{40}$ is reported. The two shown surface differ in many aspects: $Hf_{95}V_5$ present big compact

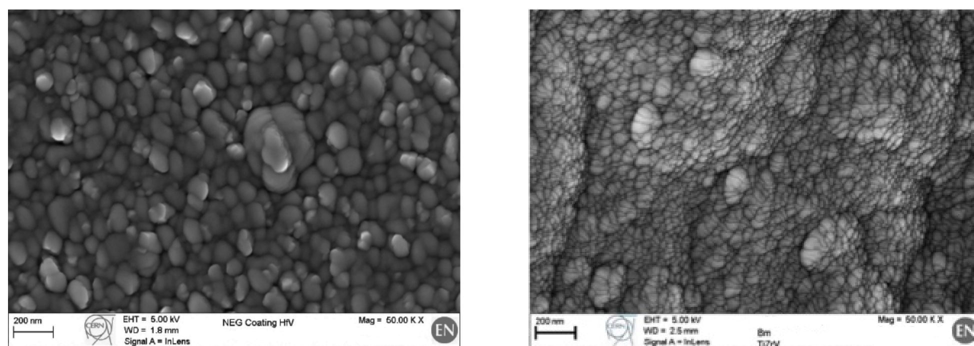


(a) SEM imagine of $Hf_{95}V_5$ surface: scale 200 $nm$, EHT 5 $kV$, WD 1, 6 $mm$ and magnification 50 K X.

(b) SEM imagine of $Ti_{29}Zr_{31}V_{40}$ surface: scale 200 $nm$, EHT 5 $kV$, WD 2, 5 $mm$ and magnification 50 K X.

FIGURE 4.21: Surface morphology of $Hf_{95}V_5$ and $Ti_{29}Zr_{31}V_{40}$.

grains, more similar to $Zr_{91}V_9$ (see **Figure 4.10(a)**) grains than to $Ti_{29}Zr_{31}V_{40}$. This morphology affects the pumping properties of the film which, as can be seen from the

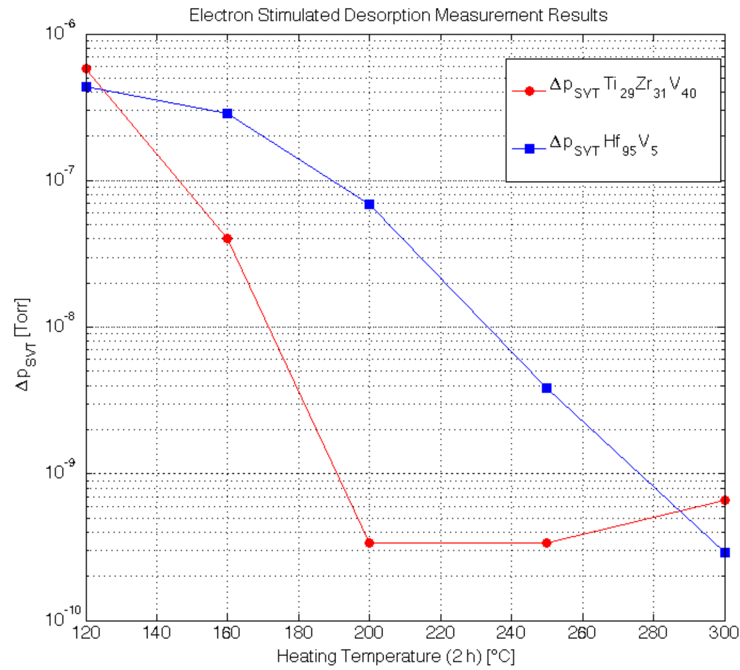


FIGURE 4.22: Comparison between the ESD results of results of $Hf_{95}V_5$ (blu squares) and $Ti_{29}Zr_{31}V_{40}$ (red dots). The measurements have been performed with an applied voltage of 500 $V$ and a current through the electron source of 1 $mA$.

ESD results presented in **Figure 4.22**. The total pressure variation after the electron bombardment for $Hf_{95}V_5$ is very low during the heating cycle, which implies that the surface is not clean and reactive enough: the surface desorption is high because of the presence of the oxide layer and the sticking probability of the film is low. These two conditions cause low pressure variation. Only for 300 °C $Hf_{95}V_5$ seems pumping: probably diffusion of the oxygen into the bulk starts at this temperature.

Increasing the percentage of vanadium in the alloys helps to better the properties of the film, as can be see analyzing the results obtained for $Hf_{70}V_{30}$ and $Hf_{65}V_{35}$. These samples have been realized using a cathode composed by two wires, one of $Hf$ with 2 $mm$ of diameter and one of $V$ with 1 $mm$ of diameter.

In **Figure 4.23** the a detail of the XPS spectra for the two samples is reported. It can be seen that the increase of the vanadium percentage has lowered the activation temperature in both cases: the reduction of the $V$ is shown in **Figure 4.23(a)** for $Hf_{70}V_{30}$, where the shift at lower binding energy of the $V2p_{3/2}$ peak and the decrease of the $O1s$ peak area are clear signs that the activation starts at 160 °C. For $Hf_{65}V_{35}$ the same conclusions can be drawn but for a higher temperature: at 200 °C the reduction of vanadium takes place.

The grains dimensions obtained through the XRD measurement are 7 $nm$ for $Hf_{70}V_{30}$

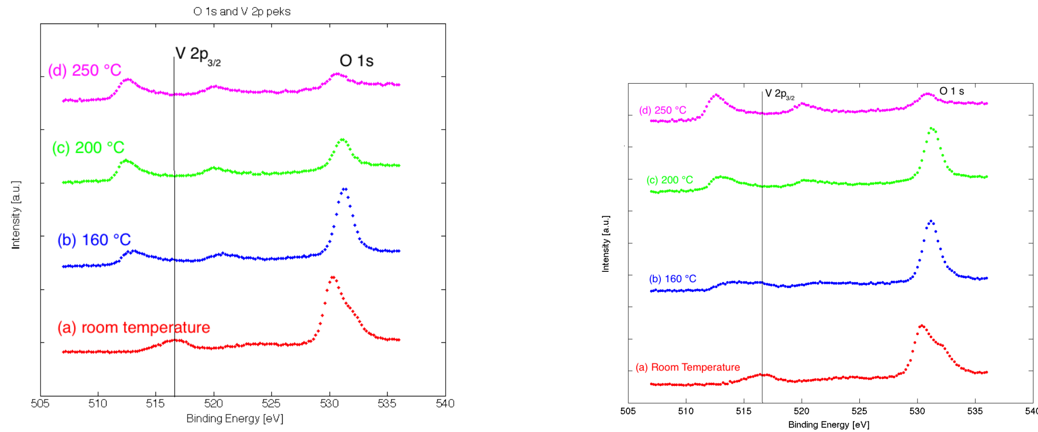


(a) $V2p$ and $O1s$ peaks of $Hf_{70}V_{30}$ for all the heating temperature (photon energy $1253,6\ eV$, time per step $50\ s$, sweeps 16.)

(b) $V2p$ and $O1s$ peaks of $Hf_{65}V_{35}$ for all the heating temperature (photon energy $1253,6\ eV$, time per step $50\ s$, sweeps 16.)

FIGURE 4.23: Details of XPS spectra for $Hf_{70}V_{30}$ and $Hf_{65}V_{35}$.

and 3 $nm$ for $Hf_{65}V_{35}$; they confirm the link between low activation temperature and grain dimension.
The surface morphology of both samples is rough and present round compact grains similar to those of $Ti_{29}Zr_{31}V_{40}$, therefore it is expected by the films pumping properties close to the one of the reference sample.Looking at the SP and ESD results presented in **Figure 4.24**, it can be concluded that this expectation is deluded. For lower temperature (160 °C and 200 °C) both the sticking probabilities are much lower than these of $Ti_{29}Zr_{31}V_{40}$ (**Figures 4.24(a)** and **4.24(b)**). Also the variation of the total pressure is not comparable to the reference sample variation (**Figure 4.24(c)**). It can be concluded that, even if all the microscopic properties of the samples are very close to the ideal one, $Hf_{70}V_{30}$ and $Hf_{70}V_{30}$ have not the sample vacuum performances as $Ti_{29}Zr_{31}V_{40}$.

Adding more vanadium helps to improve the surface morphology, but in this case too the sticking probability is low. Three samples have been realized using a braid of $Hf$ and $V$ wires with diameter 2 $mm$ and 3 $mm$, respectively, in oder to have thin film coating with an equal percentage of the two elements.
In **Figure 4.25(a)** is reported the decrease of the $O1s$ area as a function of the heating temperature for all the three samples realized. It can be seen that the decreasing of the oxygen signal starts at 160 °C. The peak area variations are beyond the CERN acceptance limit for $Hf_{45}V_{55}$ (76%) and $Hf_{40}V_{60}$ (63%), but not for $Hf_{45}V_{55}$, which it is 47%.
If the oxygen diffuses into the bulk, the samples surfaces become clean and reactive, which is proved by the ESD measurements, presented in **Figure 4.25(b)**. The pressure variations of the $HfV$ samples follow the one of $Ti_{29}Zr_{31}V_{40}$ and implies that the three

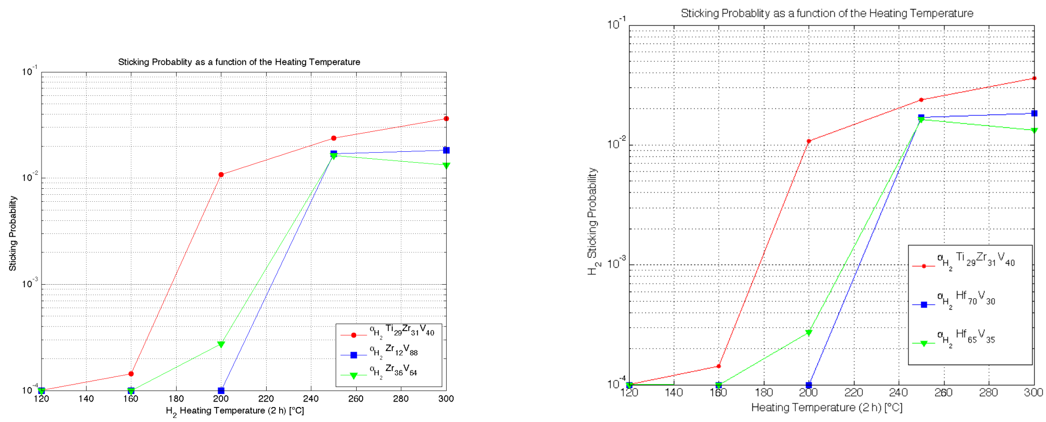


(a) Comparison between the $H_2$ sticking probabilities of $Ti_{29}Zr_{31}V_{40}$ (red dots), $Hf_{70}V_{30}$ (blu squares) and $Hf_{65}V_{35}$ (green triangles) as a function of the heating temperature.

(b) Comparison between the $CO$ sticking probabilities of $Ti_{29}Zr_{31}V_{40}$ (red dots), $Hf_{70}V_{30}$ (blu squares) and $Hf_{65}V_{35}$ (green triangles) as a function of the heating temperature.

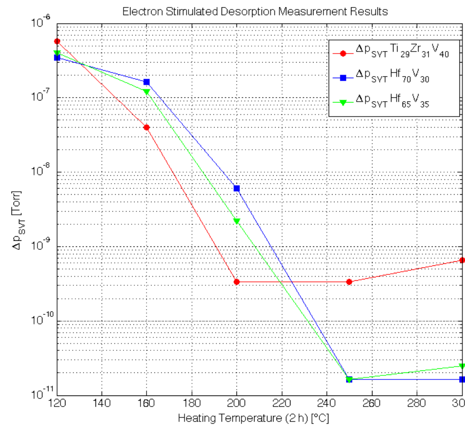


(c) Comparison between the total pressure variations after electron bombardment (500 $V$, 1 $mA$ and 100 $s$) of $Ti_{29}Zr_{31}V_{40}$ (red dots), $Hf_{70}V_{30}$ (blu squares) and $Hf_{65}V_{35}$ (green triangles) as a function of the heating temperature.

FIGURE 4.24: SEM imagines of the $HfV$ samples

samples are able to re-pump the desorbed molecules even at low heating temperature (160 °C).

The pumping properties have been improved, but they are not comparable with those of $Ti_{29}Zr_{31}$. The morphology, shown in **Figure 4.26**, for all the three samples is smooth and uniform, different from that of $Ti_{29}Zr_{31}V_{40}$; for sample $Hf_{45}V_{55}$ (**Figure 4.26(a)**) oval or round shaped fine grains can be individuated. The gains are, instead, closely packed, small and regular for sample $Hf_{40}V_{60}$ (**Figure 4.26(b)**), meanwhile the grains for $Hf_{45}V_{55}$ are polygonal and more elongated (**Figure 4.26(c)**).

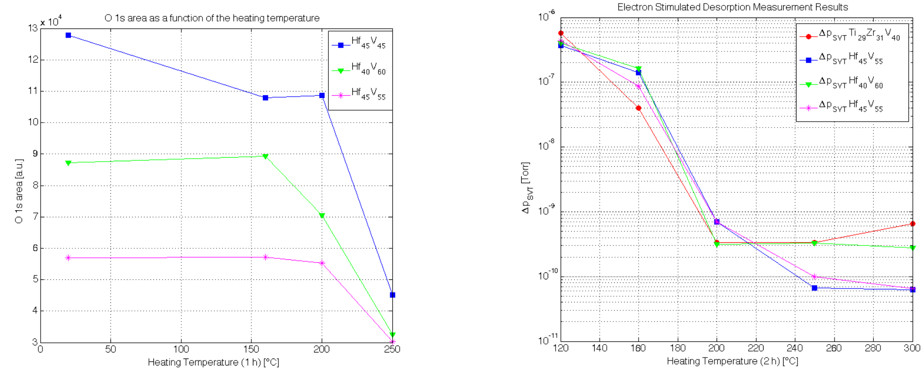


(a) Decrease of the $O1s$ area as a function of the heating temperature for $Hf_{45}V_{55}$ (blue squares), $Hf_{40}V_{60}$ (green triangles) and $Hf_{45}V_{55}$ (magenta stars)

(b) ESD results of $Hf_{45}V_{55}$ (blu squares), $Hf_{40}V_{60}$ (green triangles),$Hf_{45}V_{55}$ (magenta stars) and $Ti_{29}Zr_{31}V_{40}$ (red dots). Measurement parameters: 500 $V$, 1 $mA$.

FIGURE 4.25: XPS and ESD results for samples $Hf_{45}V_{55}$, $Hf_{40}V_{60}$ and $Hf_{45}V_{55}$

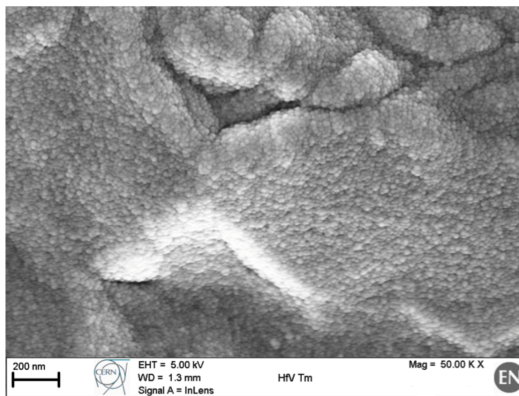


(a) SEM imagine of $Hf_{45}V_{55}$ surface: scale 200 $nm$, EHT 5 $kV$, WD $1,3$ $mm$ and magnification 50 K X.

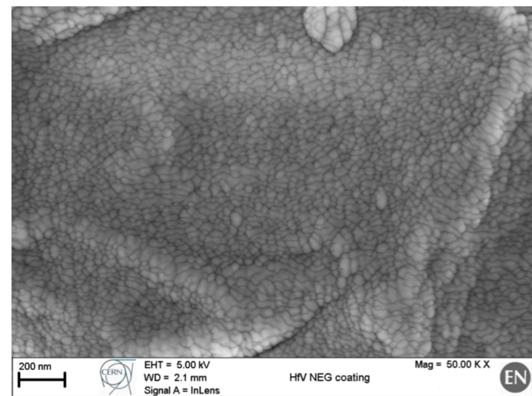


(b) SEM imagine of $Hf_{40}V_{60}$ surface: scale 200 $nm$, EHT 5 $kV$, WD $2,1$ $mm$ and magnification 50 K X.

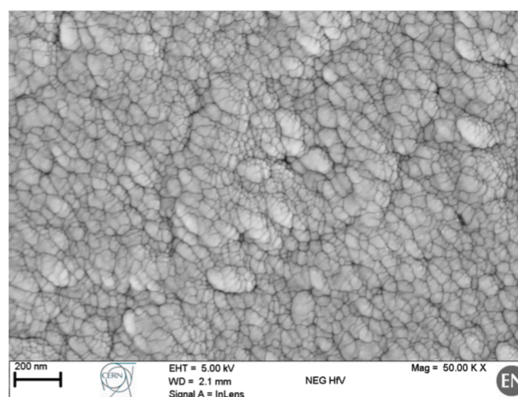


(c) SEM imagine of $Hf_{45}V_{55}$ surface: scale 200 $nm$, EHT 5 $kV$, WD $2,1$ $mm$ and magnification 50 K X.

FIGURE 4.26: SEM imagines of the $HfV$ samples

### 4.2.4 $TiZrHfV$ Campaign

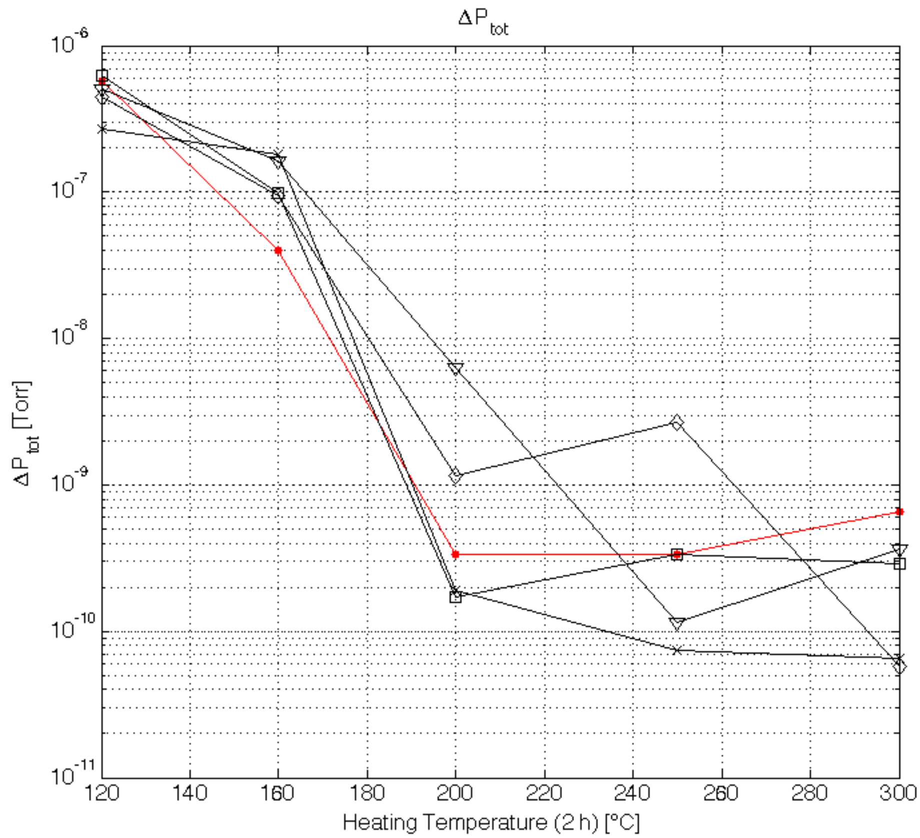


FIGURE 4.27: Results of the ESD measurements performed with an applied voltage of 500 $V$ and a current through the electron source of 1 $mA$ for the $TiZrHfV$ samples tested.

In order to fully characterized this new type of quaternary getter alloy 7 samples have been prepared as usual: the inner surface of stainless steel tubes have been coated with magnetron sputtering technique with a 1 $\mu m$ of $TiZrHfV$ thin film. The film composition have been varied changing the diameter and the number of wires used for the cathodes.
Different types of measurements have been performed:

- four samples have been tested as already done for $ZrV$ and $HfV$ samples;
- $H_2$ pumping speed measurement and $CO$ saturation measurement have been performed on one sample;
- the behavior of $H_2$ pumping speed as a function of the activation time as been evaluated for two samples.

In the following the results of the $TiZrHfV$ campaign are reported. The aim of this campaign is finding the suitable alloy composition for vacuum applications: low activation temperature and good pumping properties.

Looking at **Figure 4.27**, where the ESD results are reported in comparison with those for $Ti_{29}Zr_{31}V_{40}$, it can be seen that two samples shown a behavior very close to the one of the reference sample. They are $Ti_{23}Zr_{13}Hf_{39}V_{25}$ and $Ti_{22}Zr_{3}Hf_{44}V_{31}$, which have been realized with really similar cathode, since the aim was just varying the $Zr$ percentage in the films.

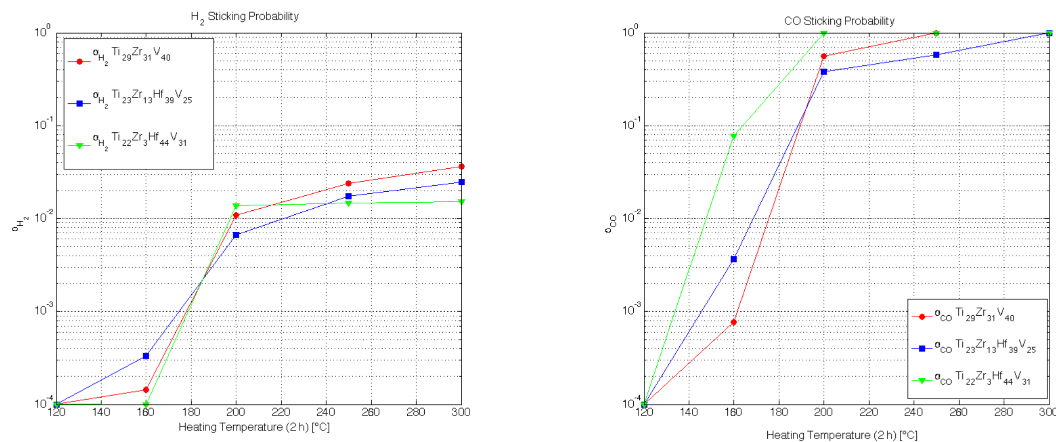


(a) Comparison between the $H_2$ sticking probabilities of $Ti_{29}Zr_{31}V_{40}$ (red dots), $Ti_{23}Zr_{13}Hf_{39}V_{25}$ (blu squares) and $Ti_{22}Zr_{3}Hf_{44}V_{31}$ (green triangles) as a function of the heating temperature.

(b) Comparison between the $CO$ sticking probabilities of $Ti_{29}Zr_{31}V_{40}$ (red dots), $Ti_{23}Zr_{13}Hf_{39}V_{25}$ (blu squares) and $Ti_{22}Zr_{3}Hf_{44}V_{31}$ (green triangles) as a function of the heating temperature.

FIGURE 4.28: $H_2$ and $CO$ sticking probabilities for $Ti_{23}Zr_{13}Hf_{39}V_{25}$ and $Ti_{22}Zr_{3}Hf_{44}V_{31}$ compared with the results obtained for $Ti_{29}Zr_{31}V_{40}$.

In **Figure 4.28** the $H_2$ and $CO$ sticking probabilities for $Ti_{23}Zr_{13}Hf_{39}V_{25}$ and $Ti_{22}Zr_{3}Hf_{44}V_{31}$ are reported as a function of the heating temperatures. Comparing the results for these samples with those of $Ti_{29}Zr_{31}V_{40}$, it can be seen from the plots that the behavior of $H_2$ sticking probability is very close to that of the reference sample (**Figure 4.28(a)**), meanwhile the $CO$ sticking probabilities of $Ti_{22}Zr_{3}Hf_{44}V_{31}$ are better than those of $Ti_{29}Zr_{31}V_{40}$ (**Figure 4.28(b)**). It can be interesting to observed that for the same heating temperature the $H_2$ sticking probability is always lower than that for $CO$, which means that is more difficult for a getter pumping $H_2$ than $CO$.

In **Figure 4.29** the ESD results are shown as a function of the heating temperature. The variation of the total pressure for the two $TiZrHfV$ samples has the same behavior that the one of the reference sample; these two samples have, therefore, a clean and reactive surface event at low temperatures (160 °C and 200 °C).

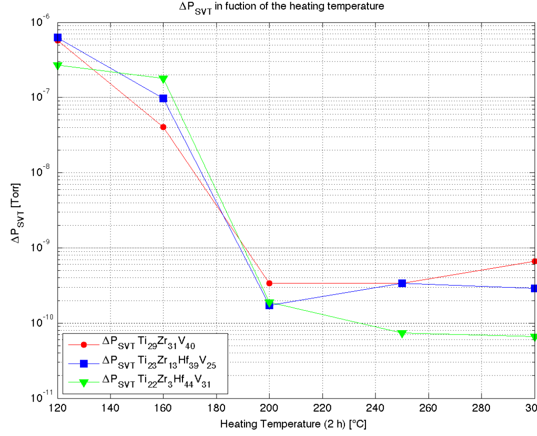


FIGURE 4.29: Results of the ESD measurements for $Ti_{29}Zr_{31}V_{40}$ (red dots), $Ti_{23}Zr_{13}Hf_{39}V_{25}$ (blu squares) and $Ti_{22}Zr_{3}Hf_{44}V_{31}$ (green triangles) as a function of the heating temperature (500 $V$, 1 $mA$ and 100 $s$).

The good pumping properties of $Ti_{23}Zr_{13}Hf_{39}V_{25}$ and $Ti_{22}Zr_{3}Hf_{44}V_{31}$ can be related with their rough surfaces, whose morphologies are similar to the that of $Ti_{29}Zr_{31}V_{40}$. They are reported in **Figure 4.30**, where the elongated and closely packed grains of both samples can be observed. In **Figure 4.30(b)** and **4.30(d)** the film profiles of $Ti_{23}Zr_{13}Hf_{39}V_{25}$ and $Ti_{22}Zr_{3}Hf_{44}V_{31}$ are respectively shown. These imagines have been realized peeling off the films from the copper substrate on which they have been grown. It is possible to see the columnar growth of the film and also its bulk structure. The grains dimensions for both samples have been calculated using the XRD spectrum; for $Ti_{23}Zr_{13}Hf_{39}V_{25}$ a dimension of 2 $nm$ results, meanwhile for $Ti_{22}Zr_{3}Hf_{44}V_{31}$ the dimension is 1 $nm$. The XRD spectrum of $Ti_{22}Zr_{3}Hf_{44}V_{31}$ is shown in **Figure 4.31**. The NEG peak, found at a Bragg angle of 37°, is broaden, which it means that is composed by a lot of nano-crystalline domain casually oriented. The peak FWHM, measured on a smoothed spectrum is 9°. The other sharp peaks present on the spectrum are diffraction peaks of the $Cu$ substrate.
In **Figure** the decrease of the $O1s$ area is reported in function of the heating temperature for $Ti_{23}Zr_{13}Hf_{39}V_{25}$ and $Ti_{22}Zr_{3}Hf_{44}V_{31}$. It can be seen that both samples show activation signs already at 160 °C, since the oxygen on the surface is lower than at room temperature. However, both the samples present some anomalies in respect to the CERN acceptance limits, as can be seen from **Table 4.9**. For example, $Ti_{23}Zr_{13}Hf_{39}V_{25}$ has a $C$ percentage on the surface in the as received conditions which is slightly higher than the limit and the decrease of the $C1s$ area is poor for both samples.

Other two compositions of $TiZrHfV$ have been tested: $Ti_{25}Zr_{23}Hf_{40}V_{12}$ and $Ti_{13}Zr_{12}Hf_{55}V_{20}$. The vanadium percentage inside both films is lower than 30% and both samples has a grain dimension around 10 $nm$. This is another prove that a certain percentage of $V$ is

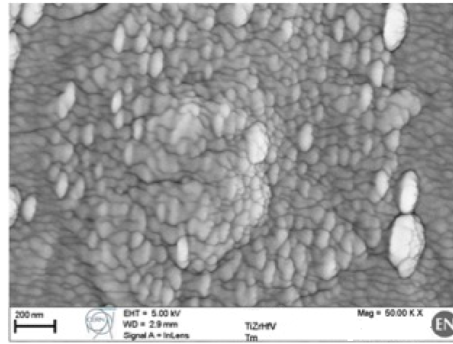


(a) SEM imagine of $Ti_{23}Zr_{13}Hf_{39}V_{25}$ surface: scale 200 $nm$, EHT 5 $kV$ and magnification 50 K X.

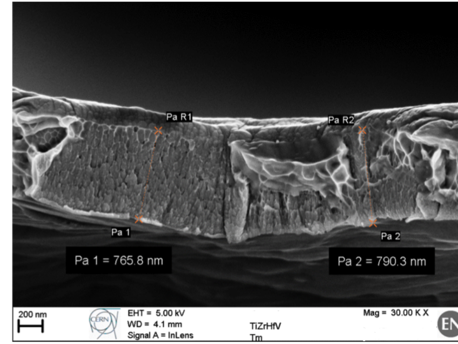


(b) SEM profile of $Ti_{23}Zr_{13}Hf_{39}V_{25}$: scale 200 $nm$, EHT 5 $kV$ and magnification 30 K X.

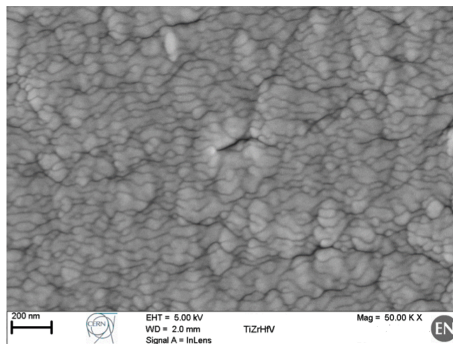


(c) SEM imagine of $Ti_{22}Zr_{3}Hf_{44}V_{31}$ surface: scale 200 $nm$, EHT 5 $kV$ and magnification 50 K X.

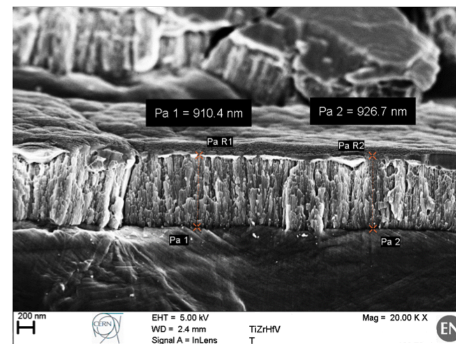


(d) SEM profile of $Ti_{22}Zr_{3}Hf_{44}V_{31}$: scale 200 $nm$, EHT 5 $kV$ and magnification 2 K X.

FIGURE 4.30: SEM imagines of surfaces and profiles of $Ti_{23}Zr_{13}Hf_{39}V_{25}$ and $Ti_{22}Zr_{3}Hf_{44}V_{31}$.

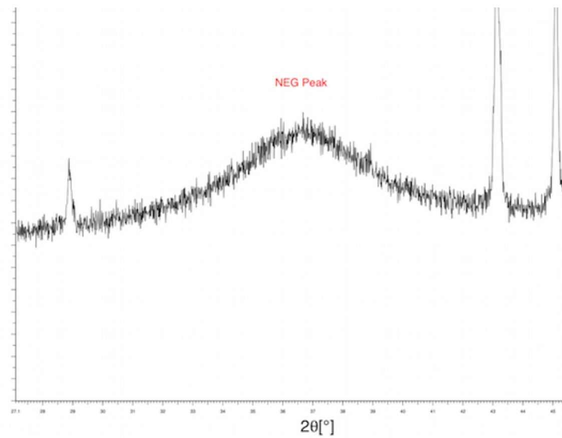


FIGURE 4.31: Not smoothed XRD spectrum of $Ti_{22}Zr_{3}Hf_{44}V_{31}$: $Cu$ K$\alpha$ source, 2Θ form 25°to 145°, step size 0, 01°and step lasting 3 $s$.

needed in order to have small grains.

In **Figure 4.33** the sticking probabilities for both the tested gases are reported in function of the heating temperatures. It can be seen that the two samples do not show activation signs until 250 °C are reached and, even when they start pumping, the sticking

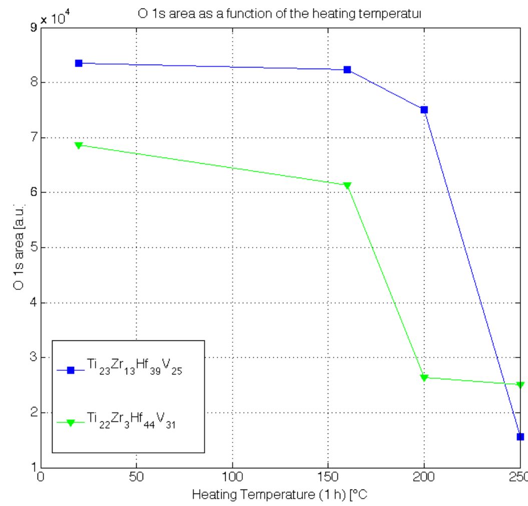


FIGURE 4.32: Decrease of the $O1s$ area as a function of the heating temperature for $Ti_{23}Zr_{13}Hf_{39}V_{25}$ (blu squares) and $Ti_{22}Zr_{3}Hf_{44}V_{31}$ (green triangles).

TABLE 4.9: XPS acceptance requirements for $Ti_{23}Zr_{13}Hf_{39}V_{25}$ and $Ti_{22}Zr_{3}Hf_{44}V_{31}$

| Sample | $O1s$ Decrease | $C$ a.r. | $C1s$ Decrease | $C_{carbide}/C_{tot}$ at 250 °C |
|---|---|---|---|---|
| $Ti_{23}Zr_{13}Hf_{39}V_{25}$ | 81% | 37% | 38% | 45% |
| $Ti_{22}Zr_{3}Hf_{44}V_{31}$ | 63% | 21% | 34% | 35% |
| Acceptance limit | $\geqslant$ 66% | $\leqslant$ 28% | $\sim$ 50% | $\sim$ 40% |

probabilities are lower than the those of the reference sample for the same temperature. The XPS measurements confirms that they do not activate correctly: the reduction of

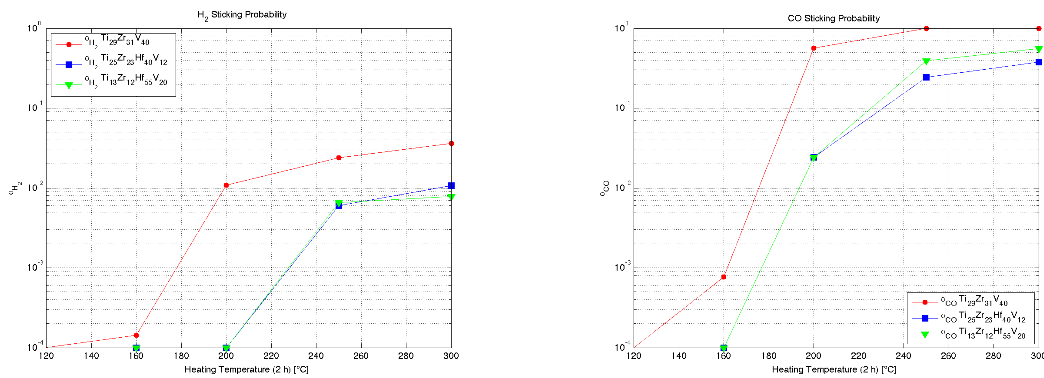


(a) Comparison between the $H_2$ sticking probabilities of $Ti_{29}Zr_{31}V_{40}$ (red dots), $Ti_{25}Zr_{23}Hf_{40}V_{12}$ (blu squares) and $Ti_{13}Zr_{12}Hf_{55}V_{20}$ (green triangles) as a function of the heating temperature.

(b) Comparison between the $CO$ sticking probabilities of $Ti_{29}Zr_{31}V_{40}$ (red dots), $Ti_{25}Zr_{23}Hf_{40}V_{12}$ (blu squares) and $Ti_{13}Zr_{12}Hf_{55}V_{20}$ (green triangles) as a function of the heating temperature.

FIGURE 4.33: $H_2$ and $CO$ sticking probabilities for $Ti_{25}Zr_{23}Hf_{40}V_{12}$ and $Ti_{13}Zr_{12}Hf_{55}V_{20}$ compared with the results obtained for $Ti_{29}Zr_{31}V_{40}$.

the metals in the film is not sufficient and starts at high temperature.

It can be concluded that $Ti_{25}Zr_{23}Hf_{40}V_{12}$ and $Ti_{13}Zr_{12}Hf_{55}V_{20}$ are not suitable film compositions for vacuum applications.

As already said a the beginning of the section, one $TiZrHfV$ sample has been tested using a Fisher-Mommsen dome (see **Chapter 3**), in order to measure its pumping properties; in particular, the $H_2$ pumping speed have been measured and the number of $CO$ molecules needed to saturate the sample have been calculated after $CO$ injections[1].
The sample tested is $Ti_{17}Zr_{29}Hf_{30}V_{24}$; the film has been coated on a DN100 stainless steel tube 50 $cm$ long with magnetron sputtering. The cathode used is composed by 5 wires: one of $Ti$ (1 $mm$ diameter), one of $Zr$(2 $mm$ diameter), two of $V$ (1 $mm$ diameter) and one of $Hf$ (2 $mm$ diameter).
The tubes coated with $Ti_{17}Zr_{29}Hf_{30}V_{24}$ has been mounted on the Fisher-Mommsen dome and after the pump down the bake-out activation procedure has began. The procedure used is the one explained in **Section 4.1**, with a different activation temperature: instead of 230 °C, the sample has been activated at 180 °C for 24 $h$, in order check if the activation temperature is close to that of standard $TiZrV$.
The measured $H_2$ pumping speed is 236 $l \cdot s^{-1}$ and it has been calculated as the average of 7 hydrogen injections. Through a Montecarlo simulation the sticking probability for $H_2$ has been calculated: $1 \cdot 10^{-3}$. The $CO$ saturation curve is shown in **Figure 4.34**, where it can be seen that the number of molecules need for saturate the $CO$ pumping speed is $2 \cdot 10^{17}$. If such a large number of molecules can remain sticked on the surface,

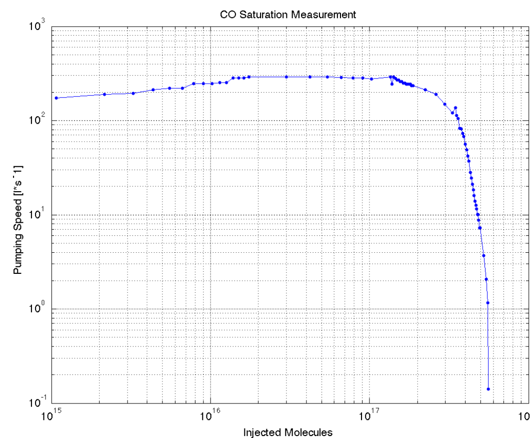


FIGURE 4.34: $Ti_{17}Zr_{29}Hf_{30}V_{24}$ $CO$ pumping speed in function of the total number of $CO$ molecules injected in the Fisher-Mommsen dome.

$Ti_{17}Zr_{29}Hf_{30}V_{24}$ should have a very rough and porous surface. The SEM imagines reported in **Figure 4.35**. In **Figure 4.35(a)** regular grains on the sample surface can

[1] The pumping speed system used is not that described in **Section 3.1.3**. It has been used a horizontal system.

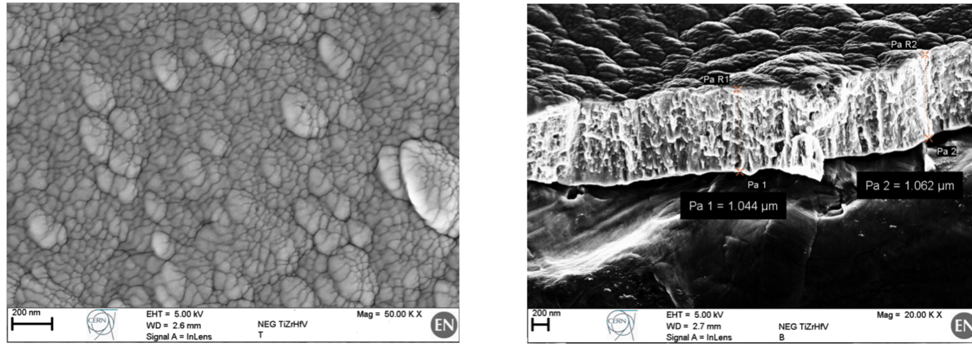


(a) SEM imagine of $Ti_{17}Zr_{29}Hf_{30}V_{24}$: scale 200 $nm$, EHT 5 $kV$ and magnification 50 K X.

(b) SEM profile of $Ti_{17}Zr_{29}Hf_{30}V_{24}$: scale 200 $nm$, EHT 5 $kV$ and magnification 20 K X.

FIGURE 4.35: SEM imagines of $Ti_{17}Zr_{29}Hf_{30}V_{24}$.

be observed; the morphology is very close to that of $TiZrV$, but the grains are slightly larger: 9 $nm$. $Ti_{17}Zr_{29}Hf_{30}V_{24}$ profile is shown in **Figure 4.35(b)**; both the columnar growth and the rough surface can be observed.

The last type of measurements performed in order to fully characterized the $TiZrHfV$ alloy consist in the evaluation of the $H_2$ pumping speed in function of the activation time. Two tubes have been coated with $TiZrHfV$ thin films of different compositions and tested on a Fisher-Mommsen dome in the following way (see **Appendix A** for more details):

1. sample mounted on the system and put under vacuum;
2. 24 $h$ of bake-out of the system while the sample has been kept at 80 °C;
3. degassing of the two measuring gauges for 15 $min$;
4. while the system is at the degassing temperature the sample is activated for 3 $h$ at 180 °C;
5. at the end of the activation the two measuring gauges have been degassed for 15 $min$;
6. cool down of the system and the sample;
7. $H_2$ pumping speed measurement;

At the end of the measurement the sample has been activated again, while the system has been kept at room temperature, but the activation time has been increased from 3 $h$ to 9 $h$. After this new activation the $H_2$ pumping speed has been measured again. This

procedure has been repeated for different activation time: 3 $h$, 9 $h$ and 24 $h$. At the end of the cycle the sample has been activated for the last measurement at 230 °C for 24 $h$. The aim of this measurement is evaluate how long should last the activation in order to reach the maximum $H_2$ pumping speed (details of the measurements procedure are in **Appendix A**).

Two sample have been tested and their results have been compared with a reference sample coated with a standard composition of $Ti_{31}Zr_{29}V_{40}$. The results are summarized in **Table 4.10**.

TABLE 4.10: $H_2$ pumping speed for the $TiZrHfV$ sample tested.

| Sample | $S_{H_2}$ $[l \cdot s^{-1}]$ 3 $h$ at 180 °C | $S_{H_2}$ $[l \cdot s^{-1}]$ 9 $h$ at 180 °C | $S_{H_2}$ $[l \cdot s^{-1}]$ 24 $h$ at 180 | $S_{H_2}$ $[l \cdot s^{-1}]$ 24 $h$ at 230 °C |
|---|---|---|---|---|
| $Ti_{31}Zr_{29}V_{40}$ | 220 | 462 | 619 | 785 |
| $Ti_{13}Zr_{24}Hf_{41}V_{21}$ | 56 | 433 | 565 | 820 |
| $Ti_3Zr_3Hf_{19}V_{76}$ | 4 | 4 | 6 | 77 |

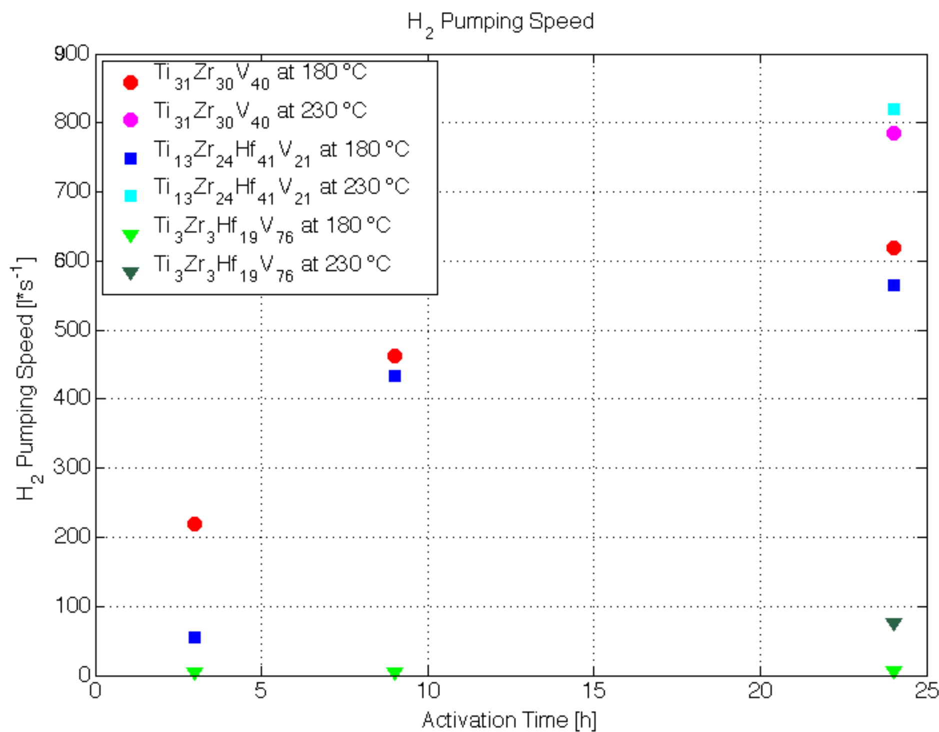


FIGURE 4.36: $H_2$ pumping speed in function of the activation time for $Ti_{31}Zr_{29}V_{40}$ (red dots), $Ti_{13}Zr_{24}Hf_{41}V_{21}$ (blue squares) and $Ti_3Zr_3Hf_{19}V_{76}$ (green triangles).

In **Figure 4.36** the $H_2$ pumping speed is reported in function of the activation time. It can be seen that for short activation (3 $h$) only $Ti_{31}Zr_{29}V_{40}$ presents a non negligible $H_2$ umping speed. In order to activate $Ti_{13}Zr_{24}Hf_{41}V_{21}$ the heating time should be longer, but from the plot it seems that 9 $h$ at 180 °C are enough to reach a pumping speed comparable to that of the reference sample. $Ti_3Zr_3Hf_{19}V_{76}$ is not activate for

any of the heating durations and temperatures tested. This is a confirmation of the fact that too much vanadium in the film does not allow to have good pumping properties.

# Chapter 5

# Discussion of the results

In the following chapter the results obtained in the two different campaign illustrated in the previous chapter are discussed in details. In particular, the answers to the following questions are given:

- does the atmosphere of the LHC tunnel affect the pumping properties of the NEG coated vacuum chambers?
- are the three NEG alloys tested suitable for vacuum application?

As **Chapter 4**, the chapter is divided in two sections where the results of the two different campaign are discussed.

## 5.1 Ageing Campaign: Influence of the LHC tunnel atmosphere

The ageing campaign has been started in order to have a deeper knowledge go the effects that the tunnel air has in the NEG coated vacuum chambers of the Long Straight Section when they are opened and exposed.
In **Table 5.1** the $H_2$ capture probability and sticking probability for the samples are reported. It can be seen that **LSS1_1** sticking probability is higher than the one of the **Reference** sample, even if it has been exposed for 9 months to the Point 1 atmosphere. As it has already pointed out in **Section 4.1**, some problems with the heating system presented during the first activation. The sample has been vented and activated a second time. This time the heating system worked correctly, as can be seen in **Figure 5.1**, but the measured pumping speed is even higher than the first value, therefore high

TABLE 5.1: $H_2$ capture probability and sticking probability for the samples tested in the ageing campaign.

| | $H_2$ Capture Probability | | | $H_2$ Sticking Probability | | |
|---|---|---|---|---|---|---|
| | I Act. | II Act. | Vent. | I Act. | II Act. | Vent. |
| **Reference Sample** | 0, 11 | - | - | $4 \cdot 10^{-3}$ | - | - |
| **LSS3_1** | – | 0, 22 | 0, 11 | - | $1,5 \cdot 10^{-2}$ | $4 \cdot 10^{-3}$ |
| **LSS3_2** | 0, 11 | - | - | $4 \cdot 10^{-3}$ | - | - |
| **LSS1_1** | 0, 18 | - | 0, 19 | $1 \cdot 10^{-2}$ | - | $1 \cdot 10^{-2}$ |
| **LSS1_2** | NOT TESTED | | | | | |
| $N_2$ **sealed** | NOT LEAK TIGHT | | | | | |

measured pumping speeds cannot be ascribed to the malfunction of the heating system. These unexpected sticking probability can be due to some problem inside the Fischer-Mommsen dome, the residual pressures during both the activations are around $10^{-9}$ $Torr$, meanwhile for the other sample tested is $10^{-11}$ $Torr$.

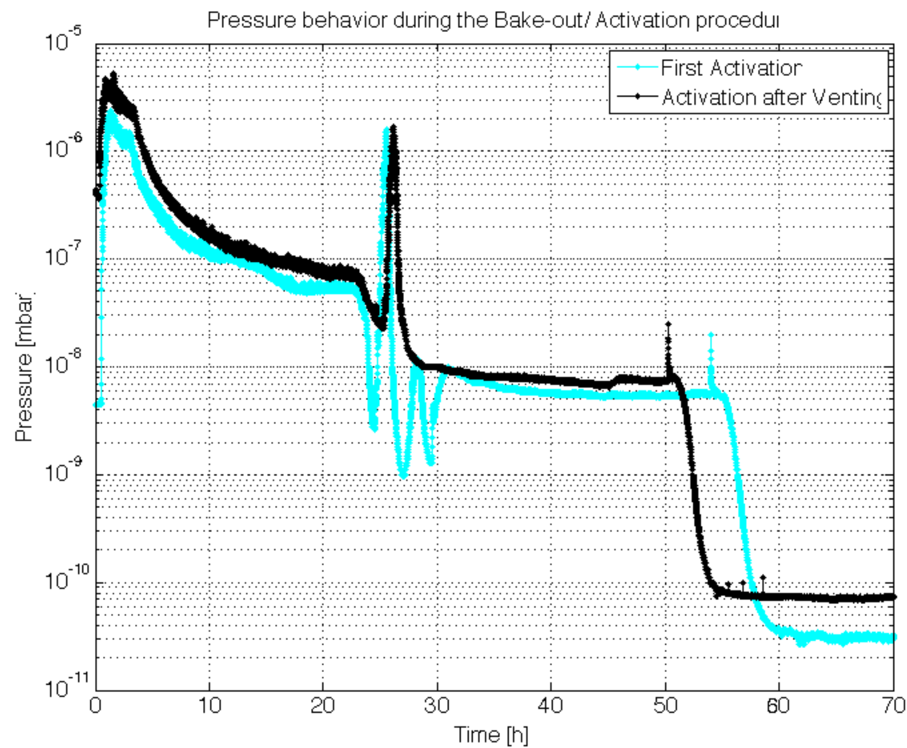


FIGURE 5.1: Grain size in function of the vanadium atomic percentage fir all the NEG materials tested.

In **Figure 5.2** the $CO$ saturation curves are reported. The samples pumping speed decrease with the increasing of the number of $CO$ molecules injected until the saturation is reached. It can be seen from the figure that the number of molecules need to saturate the surface in not affected to the exposure duration.

Unfortunately it has been not possible to conclude the campaign. As can be seen form

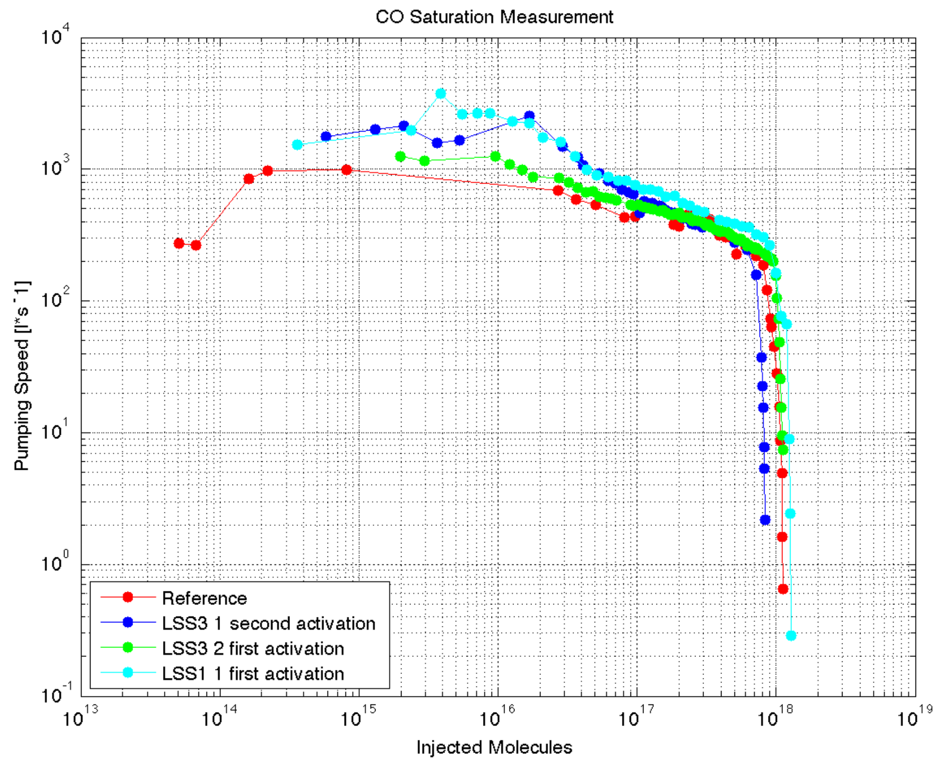


FIGURE 5.2: Comparison between the CO saturation measurements of the samples tested in the ageing campaign.

**Table 5.1**, LSS1_2 has been not tested. The sample is, in fact, located in Point 1 of LHC which is currently cooling down, therefore it is forbidden to enter that part of the tunnel. Meanwhile the sample sealed with $N_2$ has been mounted on the testing dome, but it is not leak thigh. Looking at the flange of the DN100 stainless steel tube it is possible to see that its knife is damaged. Since no UHV conditions can be reached, it is impossible to test the pumping speed of the NEG coated tubes.

Because of all the problems described, a conclusion about the effects of the LHC tunnel atmosphere on the NEG coated vacuum chambers cannot be drawn: further investigations are needed.

## 5.2 Coating Campaign: Influence of Vanadium on the *IV* Group Elements

In this section the results obtained for the three alloys tested are discussed in details. In particular, the characteristics that a NEG thin films should provide for being suitable for vacuum application are:

- low activation temperature, which means compatible with the bake-out temperature of the vacuum chambers structural materials;
- high pumping speed;
- high surface capacity.

In this section it will be show that only nanocrystalline samples have low activation temperature (smaller than 200 °C) and that nanocrystallinity is linked with the film composition. Meanwhile, the pumping properties have been found to be affected by the sample morphology.

Let us discuss the $ZrV$ samples tested. In **Table 5.2** the most important information for all the samples are reported[1].

TABLE 5.2: Main information of the $ZrV$ samples tested. In the cathode column the equivalent diameter of the wires used is reported for $Zr$ and $V$ respectively.

| Sample | Cathode | $H_2$ at 200 °C | $H_2$ at 250 °C | Grain Size $[nm]$ |
|---|---|---|---|---|
| $Zr_{91}V_9$ | (6,1) | $1 \cdot 10^{-4}$ | $5 \cdot 10^{-3}$ | 46 |
| $Zr_{72}V_{28}$ | (3,1) | $1 \cdot 10^{-2}$ | $3 \cdot 10^{-2}$ | 2 |
| $Zr_{69}V_{31}$ | (3,1) | $2 \cdot 10^{-2}$ | $4 \cdot 10^{-2}$ | - |
| $Zr_{67}V_{33}$ | (3,1) | $2 \cdot 10^{-2}$ | $3 \cdot 10^{-2}$ | 3 |
| $Zr_{55}V_{45}$ | (3,2) | $2 \cdot 10^{-2}$ | $3 \cdot 10^{-2}$ | 4 |
| $Zr_{59}V_{61}$ | (3,2) | $2 \cdot 10^{-2}$ | $3 \cdot 10^{-2}$ | 4 |
| $Zr_{38}V_{62}$ | (3,3) | $3 \cdot 10^{-3}$ | $8 \cdot 10^{-3}$ | 4 |
| $Zr_{36}V_{64}$ | (3,3) | $3 \cdot 10^{-3}$ | $2 \cdot 10^{-2}$ | 4 |
| $Zr_{35}V_{65}$ | (3,3) | $4 \cdot 10^{-3}$ | $7 \cdot 10^{-3}$ | 4 |
| $Zr_{25}V_{75}$ | (2,3) | $1 \cdot 10^{-4}$ | $2 \cdot 10^{-3}$ | 4 |
| $Zr_{24}V_{76}$ | (2,3) | $4 \cdot 10^{-4}$ | $9 \cdot 10^{-3}$ | 4 |
| $Zr_{13}V_{87}$ | (1,3) | $1 \cdot 10^{-4}$ | $1 \cdot 10^{-4}$ | 25 |
| $Zr_{12}V_{88}$ | (1,3) | $1 \cdot 10^{-4}$ | $1 \cdot 10^{-4}$ | 27 |

As can be already guessed looking at the behavior of the pressure difference in the ESD measurements reported in **Figure 4.9**, few $ZrV$ samples own properties close the the one of the $TiZrV$ sample used as reference. The difference between the samples tested is the composition of the alloy; therefore, in order to see which is the optimal atomic percentage of vanadium in the alloy, the $H_2$ sticking probability in function of the vanadium concentration is reported in **Figure 5.3(a)**. The sticking probability reported is the that measured after 2 $h$ of heating at 200 °C. This is the threshold temperature for deciding if a NEG thin film is suitable to be activated with an *in situ* baking, since it is the maximum temperature at which an aluminum vacuum camber can be heated: if the thin film has a higher activation temperate it cannot be used for coating aluminum chambers.

[1]For $Zr_{69}V_{31}$ no peak have been found on the XRD spectrum.

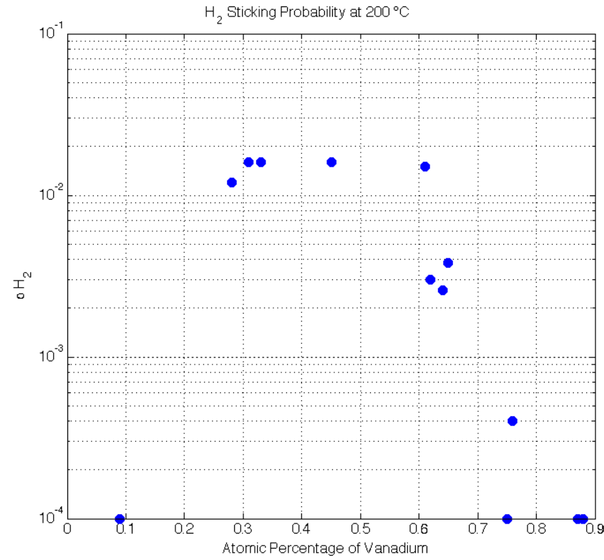


(a) $H_2$ sticking probability in function of the vanadium concentration obtained after 2 $h$ of heating at 200 °C for all the $ZrV$ samples tested.

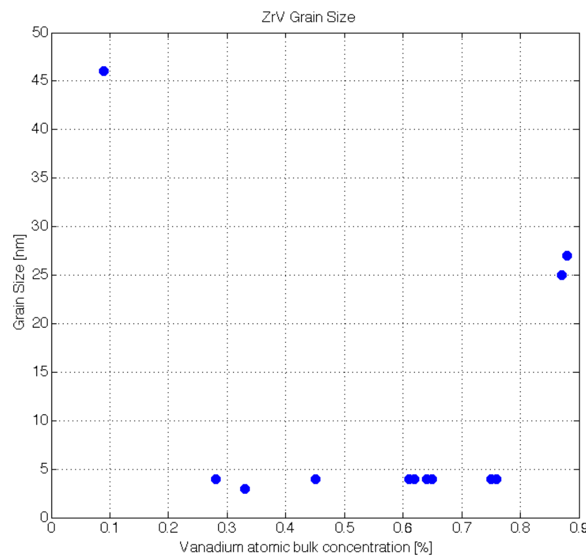


(b) Grain size in function of the vanadium atomic concentration for all the $ZrV$ samples tested.

FIGURE 5.3: $H_2$ sticking probability and grain size for all the $ZrV$ sample tested.

From **Figure 5.3(a)** it can be clearly seen that $H_2$ sticking probabilities in the order of $10^{-2}$ at 200 °C, which means comparable to those that can be obtained for a $TiZrV$ thin film, are measured for $ZrV$ film with a percentage of vanadium between the 30% and 60%. These NEG tin film have been realized using two types of cathodes: the first one composed by one wire of $Zr$ with 3 $mm$ diameter and a wire of $V$ with 1 $mm$ diameter, meanwhile the second have been realized inter-twisting one 3 $mm$ diameter wire of $Zr$

and two wires 1 $mm$ diameter of $V$. Looking at **Table 5.2** it ca be seen that with the first cathodes $V$ percentage around 30% can be reached for the film, higher percentage with the other type.

The XPS measurements confirms that the activation of these samples begins at 160 °C and is completed at 200 °C. Even their surface morphologies presents the same characteristics of the $TiZrV$ films: they are rough and porous, characteristics that affect both the sticking probability and the surface gas capacity.

As can be seen in **Figure 5.3(b)**, these NEG thin films are nano-crystalline since their grain size is lower than 5 $nm$. Other samples are nano-crystalline, which means that a wider range of atomic vanadium percentage guarantee film small grains: from 30% to 75%. For the samples with a vanadium concentration between the 60% and 75% the nano-crystallinity implies low activation temperature; the surface surface chemical composition analyses indicate that the activation starts at low temperature but it is not completed at 200 °C: higher temperatures are needed to have $H_2$ sticking probability comparable to that of $TiZrV$. It can be concluded that for percentage of vanadium into the film between the 30% and the 60% the $ZrV$ thin film coating are suitable for vacuum applications.

As it has already been said in **Section 4.2.3**, even for nano-crustalline films the vacuum performances of $HfV$ are not comparable with those of $TiZrV$ thin films.

In **Table 5.3** the most important information for all the samples are reported. It can

Table 5.3: Main information of the $HfV$ samples tested. In the cathode column the equivalent diameter of the wires used is reported for $Hf$ and $V$ respectively.

| Sample | Cathode | $H_2$ at 200 °C | $H_2$ at 250 °C | Grain Size [$nm$] |
|---|---|---|---|---|
| $Hf_{95}V_5$ | (2, 0,5) | $4 \cdot 10^{-4}$ | $7 \cdot 10^{-4}$ | 18 |
| $Hf_{70}V_{30}$ | (2,1) | $1 \cdot 10^{-4}$ | $2 \cdot 10^{-2}$ | 7 |
| $Hf_{65}V_{35}$ | (2,1) | $3 \cdot 10^{-4}$ | $2 \cdot 10^{-2}$ | 3 |
| $Hf_{56}V_{44}$ | (2,2) | $3 \cdot 10^{-4}$ | $2 \cdot 10^{-2}$ | 2 |
| $Hf_{48}V_{52}$ | (2,2) | $9 \cdot 10^{-4}$ | $2 \cdot 10^{-2}$ | 2 |
| $Hf_{46}V_{54}$ | (2,2) | $5 \cdot 10^{-4}$ | $2 \cdot 10^{-2}$ | 2 |
| $Hf_{45}V_{55}$ | (2,3) | $3 \cdot 10^{-4}$ | $2 \cdot 10^{-2}$ | 2 |
| $Hf_{40}V_{60}$ | (2,3) | $6 \cdot 10^{-4}$ | $2 \cdot 10^{-2}$ | 2 |
| $Hf_{34}V_{66}$ | (2,4) | $1 \cdot 10^{-4}$ | $6 \cdot 10^{-3}$ | 2 |
| $Hf_{18}V_{82}$ | (2,6) | $2 \cdot 10^{-4}$ | $6 \cdot 10^{-3}$ | 33 |

be noticed in **Figure 5.4(a)** that the $H_2$ sticking probabilities at 200 °C is lower than $10^{-2}$ for all the samples tested: the pumping properties of this NEG material are poor than those of $TiZrV$. It can be due to the surface morphology, which appears for these alloy smooth and uniform. In some cases the characteristic structures, shown in **Figure 5.5** have been found on the samples surfaces.

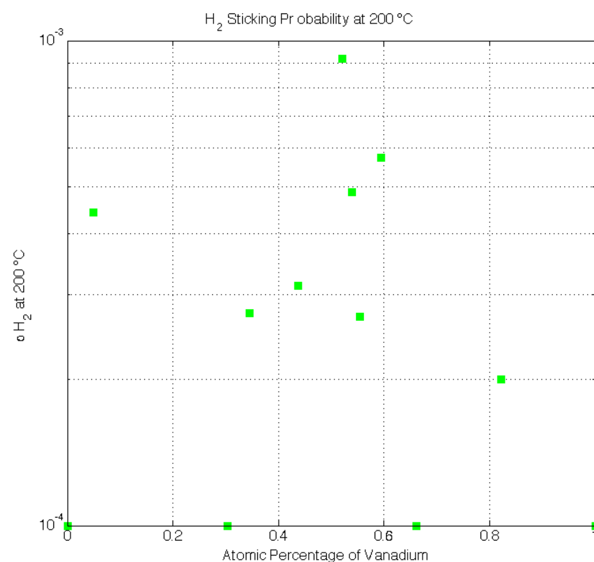


(a) $H_2$ sticking probability in function of the vanadium concentration obtained after 2 $h$ of heating at 200 °C for all the $HfV$ samples tested.

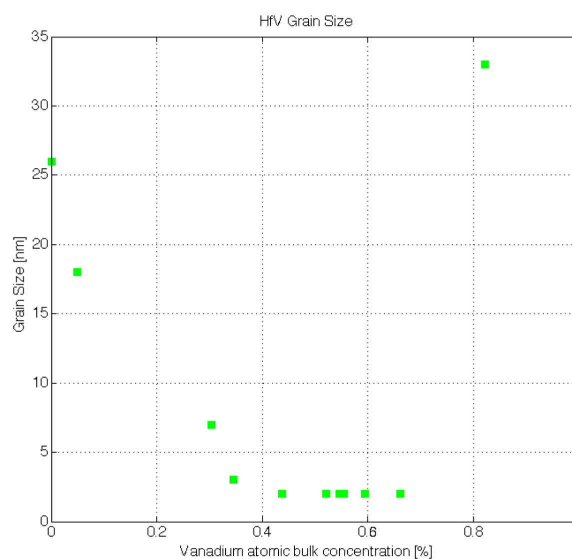


(b) Grain size in function of the vanadium atomic concentration for all the $ZrV$ sample tested.

FIGURE 5.4: $H_2$ sticking probability and grain size for all the $HfV$ sample tested.

Nano-crystalline films can be obtained adding to hafnium a percentage of vanadium between 0, 35 and 0, 65, as can be seen in **Figure 5.4(b)**. The XPS measurements confirm that these samples own low activation temperature, but, even when the activation starts correctly at 160 °C, it is fully completed at 250 °C.

The elements present in the alloy affect the properties of the film; the lack of $Ti$ or $Zr$ may be the cause of the poor vacuum properties of $HfV$.

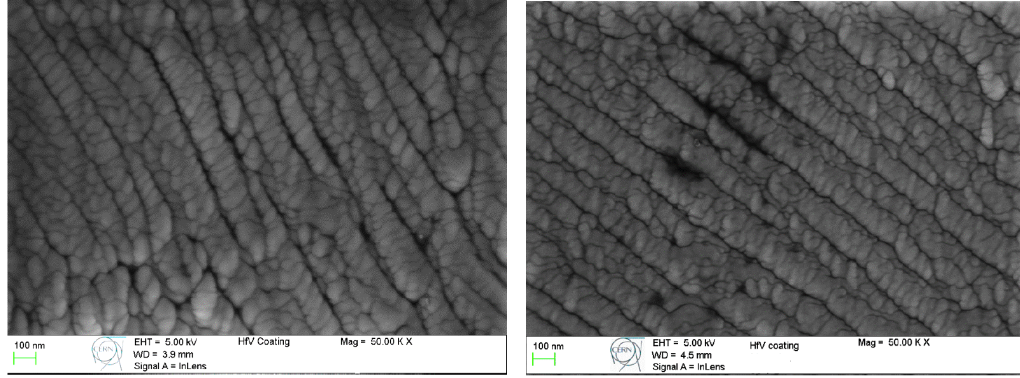


(a) SEM imagine of $Hf_{70}V_{30}$ surface: scale 100 $nm$, EHT 5 $kV$ and magnification 50 K X.

(b) SEM imagine of $Hf_{66}V_{44}$ surface: scale 100 $nm$, EHT 5 $kV$ and magnification 50 K X.

FIGURE 5.5: Characteristic surface structures found in some $HfV$ samples.

The last NEG material tested is a quaternary alloy: $TiZrHfV$. In **Table 5.4** all the samples tested are summarized.

TABLE 5.4: Main information of the $TiZrHfV$ samples tested. In the cathode column the equivalent diameter of the wires used is reported for $Ti$, $Zr$, $Hf$ and $V$ respectively.

| Sample | Cathode | $H_2$ at 200 °C | $H_2$ at 250 °C | Grain Size [$nm$] |
|---|---|---|---|---|
| $Ti_{25}Zr_{23}Hf_{40}V_{13}$ | (2,2,2,1) | $1 \cdot 10^{-4}$ | $6 \cdot 10^{-3}$ | 9 |
| $Ti_{13}Zr_{12}Hf_{55}V_{20}$ | (1,1,2,1) | $1 \cdot 10^{-4}$ | $6 \cdot 10{-}33$ | 10 |
| $Ti_{13}Zr_{24}Hf_{41}V_{21}$ | (1,2,2,2) | – | – | 2 |
| $Ti_{17}Zr_{30}Hf_{31}V_{24}$ | (1,2,2,2) | – | – | 8 |
| $Ti_{15}Zr_{13}Hf_{40}V_{25}$ | (2,2,2,2) | $7 \cdot 10^{-3}$ | $2 \cdot 10^{-2}$ | 2 |
| $Ti_{22}Zr_{3}Hf_{43}V_{31}$ | (2,1,2,2) | $1 \cdot 10^{-2}$ | $1 \cdot 10^{-2}$ | 1 |
| $Ti_{3}Zr_{3}Hf_{19}V_{76}$ | (0,25,0,25,6,1) | – | – | - |

Looking at **Figure 4.28** and **Figure 4.36**, it can be seen that some of the film deposited have the same pumping properties as $TiZrV$ thin films and sometimes even better. Both the $H_2$ and $CO$ sticking probabilities for low temperature, i.e. 160 °C, are higher than the those of the reference sample at the same temperature, which suggest a lower activation temperature. $TiZrHfV$ thin film coatings with low activation temperature have been already observed [34]; the results obtained in the present confirms the observation. Moreover, other film compositions, with different percentages of the four elements, have been characterized showing that the good activation behavior is linked with the sample crystalline structure which is link to the composition, as for the other NEG material tested. In **Figure 5.6** the grain dimension has been reported as a function of the atomic vanadium percentage and it is compared with that of the other NEG materials tested. Nano-crystallinity is obtained, even for this quaternary material, for vanadium percentage higher than 20%, with the only exception of $Ti_{17}Zr_{29}Hf_{30}V_{24}$, whose grains are 8 $nm$ width. The XPS measurements confirm that the samples with grain sizes smaller than 5 $nm$ start their activation at low temperature.

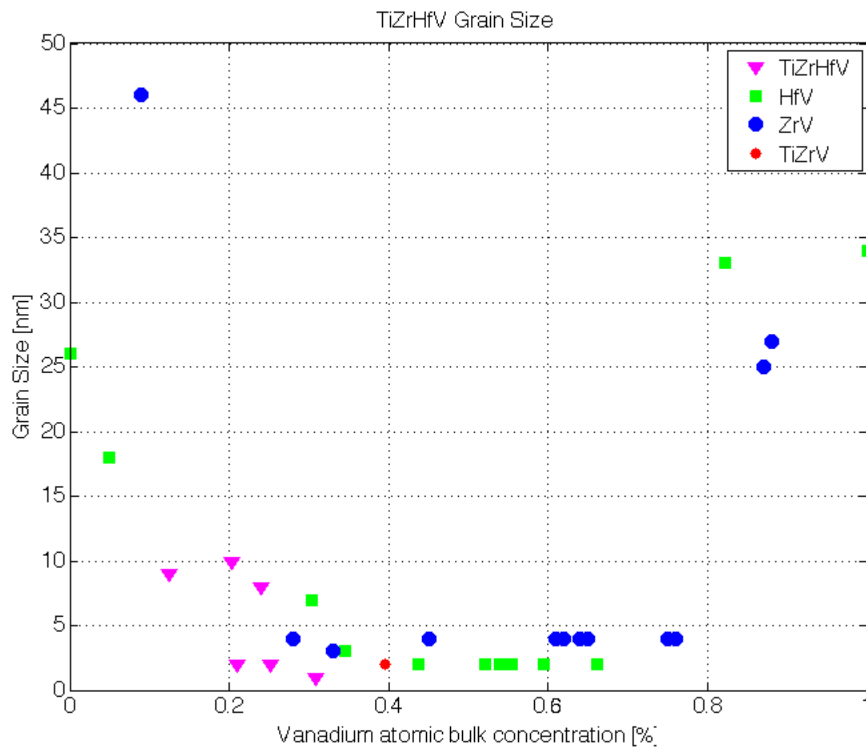


FIGURE 5.6: Grain size in function of the vanadium atomic percentage fir all the NEG materials tested.

It can be concluded that even for $TiZrHfV$ alloys the relation between crystalline structure, activation temperature and vanadium atomic percentage has been observed. These materials shown an interesting behavior at low temperature, since at 160 °C the pumping properties are better than those of $TiZrV$ films. Further investigations are needed.

In conclusion of this chapter a comparison between the $H_2$ sticking probability in function of the vanadium atomic percentage in the thin film for all the alloy tested is reported for two different heating temperature: 200 °C in **Figure** 5.7(a) and 250 °C in **Figure** 5.7(b). The behavior of a NEG thin film at 200 °C is fundamental since 200 °C i maximum temperature at which an aluminum vacuum chamber can be baked. Films with higher activation temperature or with pumping properties poor after the heating at this temperature cannot be used for vacuum applications, since their use is limited to stainless steel and copper vacuum chambers. Looking at **Figure** 5.7 it is clear that all the $HfV$ alloy are not suitable since at 200 °C the composition tested are or not activated or own to poor pumping properties. Meanwhile some compositions of $ZrV$ and $TiZrHfV$ can be used as internal coating for all the types of vacuum chambers.

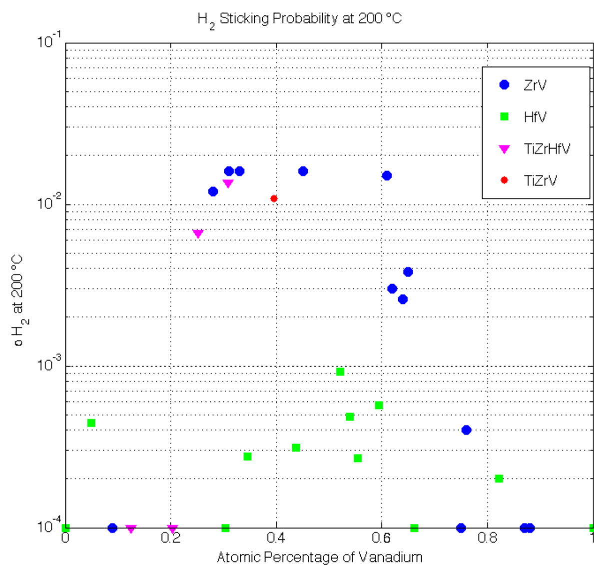


(a) Comparison between the $H_2$ sticking probability at 200 °C of all the alloys tested.

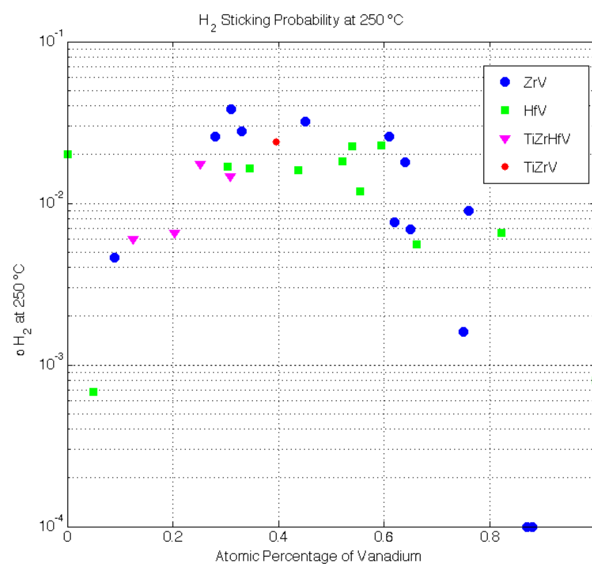


(b) Comparison between the $H_2$ sticking probability at 250 °C of all the alloys tested.

FIGURE 5.7: $H_2$ sticking probability in function of the vanadium percentage in the film for all the three alloys tested.

# Chapter 6

# Conclusions

The Non-Evaporable Getter (NEG) Material are capture pumps, which means materials able to remove molecules from the gas phases; they chemically react with the most gases present in the vacuum system forming with them stable compounds at room temperature. They are widely used in a variety of applications including particle accelerators. They can be sputtered in order to form a thin film coating on the internal walls of vacuum chambers, transforming them from a gas source into a pump.
NEG thin film coatings provide some advantages if compared to traditional pumps:

- reaction of the thermal outgassing;
- reduction of the ions induced degassing;
- lower ultimate pressure;
- simplification of vacuum chambers design;
- reduction of the secondary electron yield.

The NEG active surface is obtained by heating *in situ* the surface; this procedure, called activation, allows the diffusion of the oxygen composing the surface oxide layer into the bulk of the material leaving a very reactive and clean surface. The dissolution of the native oxide layer is possible only if the transfer of oxygen in the solid solution is thermodynamically allowed and the oxygen diffusion rate in the film is sufficiently fast (temperature dependence of both the process). Therefore, all the NEG material own an activation temperature; it is of fundamental importance that this temperature is compatible with the vacuum chambers structural materials in order to allow the activation of the NEG coating during the bake-out.

NEG thin film coating are already used in particle accelerators and synchrotron. By far their most significant benchmark is the Large Hadron Collider (LHC) at CERN, where about six kilometer of beam pipes are coated with $Ti_3Zr_{30}V_{40}$ thin films.
The NEG coated vacuum chambers already installed may be subject of maintenance. In the LHC, for example, a Long Shutdown (LS1) ended in June 2014 and others are planned in order to high the ma-chine luminosity. Since LS1 the NEG reactivation, after the exposure to the LHC atmosphere, presented problems in some cases, it has been decided to study in details if the exposure to tunnel atmosphere for long periods affects the pumping properties of a NEG coated vacuum chamber. An ageing campaign has, therefore, been planned. In the first part of the present work the results obtain in this campaign have been presented; six $Ti_{30}Zr_{30}V_{40}$ coated vacuum chambers have been exposed for different periods and in different points of the tunnel. $H_2$ pumping speed and CO saturation measurements have been performed.
The results obtained suggest that the exposition at the LHC tunnel atmosphere does not affect the the pumping properties of the NEG coating. However, there have been problems in the activation of some chambers due to the experimental set-up. Further investigations are needed.

After the application in the LHC, the NEG materials obtained the attention of the scientific world, since it was clear that they are the solution for most of the ultra high vacuum issues. Systematic study of their properties is needed in order to provide a better understanding of the activation mechanism; it could allow us to find out rules for the selection of new alloys, maybe with lower activation temperature and better pumping properties.
It is known that the elements of the $IV$ group of the periodic table are suitable candidate for being NEG material since they are reactive, they show high solubility for oxygen and good diffusivity. Unfortunately, if sputtered on a vacuum chamber, their activation temperatures are high. Therefore, considering the results obtained for $TiZrV$ alloys, in the present work vanadium has been added to the $IV$ group elements thin films. In particular, two binary alloys, $ZrV$ and $HfV$, and a quaternary alloy, $TiZrHfV$, have been studied in order to find compositions with low activation temperature and good pumping properties.
The obtained results prove that, as the case of $TiZrV$, even for all the alloys tested low activation temperatures are linked with the nano-crystallinity of the film: only films with crystalline grains smaller than 5 $nm$ have activation temperatures lower than 200 °C. Such a small grain dimension can be reached only adding to $IV$ group elements a certain percentage of vanadium: from 30% up to 75% for $ZrV$, from 35% up to 65% for $HfV$ and higher than 20% for $TiZrHfV$.
The pumping properties are affected by the surface morphology and the elements present

in the alloy. Rough surface increases the probability of multiple collisions and the area available for reactions. Rough surface can be obtained for all the alloy tested, but $ZrV$ and $TiZrHfV$ are much more effective in pumping than $HfV$; even for those $HfV$ samples with low activation temperature and rough surface the pumping performances after 2 $h$ of heating at 200 °C are not comparable to those of $TiZrV$. Meanwhile there are compositions for both $ZrV$ and $TiZrHfV$ with characteristics very close to those of $TiZrV$. Adding between 30% and 60% of vanadium into a zirconium film it is possible to have both low activation temperature and $H_2$ sticking probability after two hours of activation at 200 °C in the order of $1 \cdot 10^{-2}$. These types of $ZrV$ alloy are, therefore, suitable for vacuum applications. $TiZrHfV$ alloys are suitable for vacuum applications: they show an interesting behavior at low temperature, since at 160 °C the pumping properties are better than those of TiZrV films. It can be noted that the two samples with the best properties ($Ti_{23}Zr_{13}Hf_{39}V_{25}$ and $Ti_{22}Zr_{3}Hf_{44}V_{31}$) have a low percentage of zirconium in them. It could be interesting see what happen if $Zr$ is eliminated from the alloy. Further investigations for $TiZrHfV$ could be needed.

# Appendix A

# Pumping Speed Measurements Procedure

In the following the pumping speed measurement procedure for the ageing campaign samples and for the coating campaign samples are reported in details.

## A.1 Pumping Speed Measurement Procedure for the Ageing Campaign Samples

The following measurement procedure is that used for testing the ageing campaign samples. The Fischer-Mommsen dome used is that shown in **Figure 3.13**.

1. mount the sample on the DN100 ending flange of the Fischer-Mommsen dome;
2. open the gate valve;
3. open the connection between the TMP and the primary pump;
4. switch on the TMP;
5. when the TMP has reached its maximum speed, switch on the cold cathode gauge;
6. perform a leak detection using a leak detector;
7. if no leaks have been found, put the thermocouples on the sample;
8. put the heating equipment on the sample;
9. open the two needle valves connecting the dome with the injection line;

10. start the bake-out activation procedure;
    - bake the system for 24 $h$, while the sample is kept at 120 °C (the temperatures are reported in **Figure 4.2(a)**).
    - when the system has reached the degassing temperature, start the activation of the sample for 24 $h$ at 230 °C;
11. 30 $min$ before the ending of the activation, close the two needle valves;
12. start degassing the two hot cathode gauges;
13. cool down the system;
14. clean the injection line:
    - open the $H_2$ bottle;
    - fill the line with $H_2$;
    - close the $H_2$ bottle;
    - fill the cryo-trap with liquid nitrogen;
    - open the connection between the cryo-trap and the primary pump;
    - open the two valves connecting the injection line to the trap;
    - when the line is empty, close the two valves;
    - repeat the procedure for two or three times and at the end close the connection between the primary pump and the trap;
15. open the $H_2$ bottle;
16. fill the line with $H_2$;
17. take note of the pressure displayed by the two hot cathode gauges;
18. start injecting $H_2$ from the bottom needle valve:
    - open he bottom needle valve until the pressure is one order of magnitude higher than the residual pressure,
    - let the pressure stabilize;
    - take note of the pressures displayed in the two hot cathode gauges;
    - open a little bit more the bottom needle valve;
    - repeat previous instructions in order to have three or four pressures values;
19. close the bottom needle valve;
20. close the $H_2$ bottle;

21. let the system pressure goes down until the pressure residual values are reached again;
22. clean the injection line from $H_2$:
    - fill the cryo-trap with liquid nitrogen;
    - open the connection between the cryo-trap and the primary pump;
    - open the two valves connecting the injection line to the trap;
    - when the line is empty, close the two valves;
    - open the $CO$ bottle;
    - fill the line with $CO$;
    - close the $CO$ bottle;
    - open the connection between the cryo-trap and the primary pump;
    - open the two valves connecting the injection line to the trap;
    - when the line is empty, close the two valves;
    - repeat the procedure for two or three times and at the end close the connection between the primary pump and the trap;
23. open the $CO$ bottle;
24. fill the line with $CO$;
25. take note of the pressure displayed by the two hot cathode gauges;
26. start injecting $CO$ from the bottom needle valve:
    - open he bottom needle valve until the pressure is one order of magnitude higher than the residual pressure,
    - let the pressure stabilize;
    - take note of the pressures displayed in the two hot cathode gauges and of the time;
    - open a little bit more the bottom needle valve;
    - repeat previous instructions every 30 $s$ until the $CO$ pumping speed is saturated;
27. close the bottom needle valve;
28. close the $CO$ bottle;
29. for dismounting the sample:
    - switch off all the gauges:

- close the gate valve;
- close the connection between the TMP and the primary pump;
- switch off the TMP;
- open the sample flange.

## A.2 Pumping Speed Measurement Procedure for the Coating Campaign Samples

The following measurement procedure is that used for testing the coating campaign samples. The Fischer-Mommsen dome used is that shown in **Figure 3.13**.

1. mount the sample on the DN100 ending flange of the Fischer-Mommsen dome;
2. open the gate valve;
3. open the connection between the TMP and the primary pump;
4. switch on the TMP;
5. when the TMP has reached its maximum speed, switch on the cold cathode gauge;
6. perform a leak detection using a leak detector;
7. if no leaks have been found, put the thermocouples on the sample;
8. put the heating equipment on the sample;
9. open the two needle valves connecting the dome with the injection line;
10. start the bake-out activation procedure;
    - bake the system for 24 $h$, while the sample is kept at 80 °C (the temperatures, except the one of the sample, are reported in **Figure 4.2(a)**).
    - when the system has reached the degassing temperature, close the two needle valves;
    - start degassing the two hot cathode gauges for 15 $min$;
    - at the end of the degassing, start the activation of the sample for 3 $h$ at 180 °C;
11. 15 $min$ before the ending of the activation, start degassing the two hot cathode gauges for 15 $min$;

12. cool down the system;

13. clean the injection line:

    - open the $H_2$ bottle;
    - fill the line with $H_2$;
    - close the $H_2$ bottle;
    - fill the cryo-trap with liquid nitrogen;
    - open the connection between the cryo-trap and the primary pump;
    - open the two valves connecting the injection line to the trap;
    - when the line is empty, close the two valves;
    - repeat the procedure for two or three times and at the end close the connection between the primary pump and the trap;

14. open the $H_2$ bottle;

15. fill the line with $H_2$;

16. take note of the pressure displayed by the two hot cathode gauges;

17. start injecting $H_2$ from the bottom needle valve:

    - open he bottom needle valve until the pressure is one order of magnitude higher than the residual pressure,
    - let the pressure stabilize;
    - take note of the pressures displayed in the two hot cathode gauges;
    - open a little bit more the bottom needle valve;
    - repeat previous instructions in order to have three or four pressures values;

18. close the bottom needle valve;

19. close the $H_2$ bottle;

20. start the heating the sample for 9 $h$ at 180 °C;

21. repeat the procedure from point 12 to point 19;

22. start heating the sample for 24 $h$ at 180 °C;

23. repeat the procedure from point 12 to point 19;

24. start heating the sample for 24 $h$ at 230 °C;

25. repeat the procedure from point 12 to point 19;

26. for dismounting the sample:

    - switch off all the gauges:
    - close the gate valve;
    - close the connection between the TMP and the primary pump;
    - switch off the TMP;
    - open the sample flange.

# Appendix B

# Coating Procedure

## B.1 Stainless Steel Tubes Cleaning Procedure

In the following the cleaning procedure used for the stainless steel tubes used as substrate for the NEG coatings tested in the coating campaign is reported. The procedure name is Net Inox and it has been developed at CERN.

- pickling:
  - Net inox (pure) : $HNO_3$;
  - temperature: 20 °C. (50%)+$HF$(3%);
  - time: $30 \div 90$ $min$;
  - rinsing with water;
- neutralization with detergent and ultrasonic:
  - detergent $NGL$ 17.40 spec. $ALU$ III: 10 $g/l$;
  - Temperature: $50 \div 60$ °C;
  - Time: $5 \div 10$ $min$;
- rinsing with water;
- rinsing with demineralised water
- alcohol drying with clean compressed air;
- bake-out.

## B.2 Stainless Steel Tubes Coating Procedure

In this section the procedure followed for the preparation of all the samples tested in the coating campaign is reported in some details. the scheme of the system used is reported in **Figure ??**.
The first thing to be prepared is the cathode.
After the assembly of the coating tower, it has to be put under vacuum:

1. put the tower on the support and close the flange;
2. open the bypass valve;
3. open the main valve;
4. open the connection between the primary pump and the TMP;
5. switch on the TMP;
6. when the TMP has reached the maximum speed, switch on the cold cathode gauge;
7. perform a leak detection.

Once that the coating tower is mounted, put under vacuum and in case of no leaks found, the coating can be performed:

1. ran a scan of the RGA taking note of the total pressure;
2. remove the RGA from the system (switch of SEM and Emission and close the communication with the computer);
3. connect the cathode to the power supply;
4. lower the magnet;
5. cable the magnet;
6. heating the sample at 100 °C;
7. open the bypass valve;
8. close the main valve;
9. change the pressure channel of the cold cathode gauge (channel 2);
10. open the $Kr$ bottle;
11. open the $Kr$ injection valve;

12. let the pressure going up until it reaches $6 \cdot 10^{-3}$ $mbar$;

13. program the limit values of power supply:

    - power $P = 0,1\ kW$;
    - potential difference $U = 600\ V$;
    - current $I = 0,2\ A$;

14. when the sample is at 100 °C and the pressure is more or less stable at $6 \cdot 10^{-3}$ $mbar$, switch on the magnetic field and the electric field;

15. take note of the parameters evolution during the coating, writing them on the excel file. The excel sheet calculates the thickness of the coating and can be used for evaluating the duration of the coating;

16. when 1 $\mu m$ of coating thickness is reached, the electric and magnetic filed can be switched off.

17. close the $Kr$ injection valve;

18. close the $Kr$ bottle;

19. open the main valve in order to let the pressure go down;

20. switch off the heating of the sample;

21. disconnect the solenoid and lift it:

22. when the pressure reaches $10^{-7}$ $mbar$ on channel 1 of the gauge, close the main valve and let the system cool down.

For dismounting the sample from the coating tower follow the following procedure:

1. switch off all the gauges;

2. close the main valve;

3. close the bypass valve;

4. switch off the TMP;

5. close the connection between the primary pump and the TMP;

6. start unscrewing the screws at the bottom of the tower.

# Appendix C

# Sticking Probability and ESD Measurement Procedure

In the following the procedure for performing the sticking probability and the electron stimulated desorption measurements is reported in details. The system used is that described in **Section 3.3.3**. For all the abbreviations used in the following see **Figure C.2**

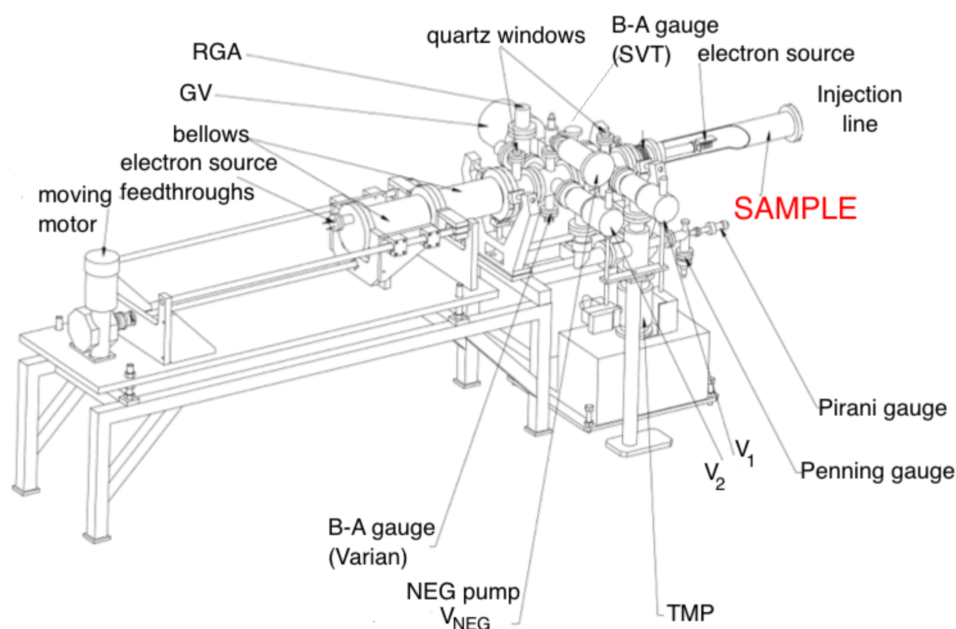


FIGURE C.1: ESD system: it has been used for performing both the sticking probability and the electron stimulated desorption measurements.

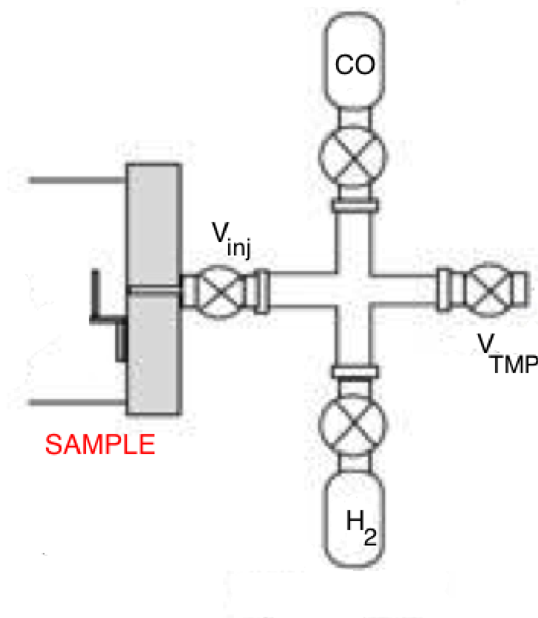


FIGURE C.2: ESD system particular of the injection line used for the sticking probability measurementszs.

## C.1 Mounting and Dismounting Samples

### C.1.1 Dismounting Samples

In order to dismount a sample from the measurement system the sample vacuum chamber must be isolated from the rest of the system. Therefore, all the valve that connect this chamber with the pumping group must be closed. The connection between the electron source vacuum chamber and the pumping group must be opened.

1. Close $GV$;
2. close $V_1$;
3. open $V_2$;
4. close $V_{NEG}$;
5. close $V_{inj_1}$ and $V_{inj_2}$;
6. switch off the filament and the power of the $SVT$ gauge;
7. start dismounting the sample from the measurement system unscrewing all the screws.

### C.1.2 Mounting Samples

After the dismounting of a sample the system is ready for a new sample to be tested. In order to make the vacuum inside the sample vacuum chamber the $TMP$ must be switch off.

1. Open $V_{NEG}$;
2. close $V_2$;
3. close the connection between the primary pump and the $TMP$;
4. switch off the $TMP$ using its control panel;
5. mount the NEG coated tube on the measurement system. This operation can be performed while the speed of the $TMP$ goes to zero.
    - Distance the injection line form the rest of the system in order to have enough space to put the tube that has to be mounted;
    - put some screws inside the flanges of both sides in order to support the new gaskets;
    - put the support for the tube on the table;
    - clean two new gasket with alcohol ($C_2H_5OH$);
    - for both sides of the system insert the gasket between the two flanges;
    - approach the injection line to the rest of the system in order to close the flanges;
    - tight all the screws;
6. open $V_1$;
7. switch on the $TMP$ using its control panel;
8. open the connection between the primary pump and the $TMP$;
9. wait for the $TMP$ to gain speed and pump down;
10. switch on the SVT gauge

### C.1.3 Leak Detection

After the mounting of new samples it has to be checked that there are no leaks, therefore a leak detection must be performed. During this procedure the part of the system that

has been opened is exposed to a small flux of $He$ and the amount of $He$ inside the system is monitored thanks to a RGA calibrated to follow only the time evolution of mass number four.
This procedure can be performed in two different ways: using the RGA installed on the measurement system or using an external one.
In the following of the section both the procedures are going to be illustrated step by step.

#### C.1.3.1 Procedure 1

If the RGA has to be used, this procedure has to be followed:

1. open $GV$;
2. open $V_1$;
3. close $V_2$;
4. close $V_{NEG}$;
5. open the program *TuneUp*;
6. using the $He$ tank expose the flanges of the system to a small flux of $He$:
    - all the circumference of the flange must be exposed to the $He$ flux;
    - all the flanges that have been opened must be checked starting from the furthest from the pumping group;
7. if there is a peak on the spectrum you have a leak; if, instead, the spectrum remains flat there are no leaks in the system.

This procedure must be followed by a full bake-out.

#### C.1.3.2 Procedure 2

If an external leak detector has to be used, this procedure has to be followed:

1. close $GV$;
2. open $V_1$;
3. close $V_2$;

4. open $V_{NEG}$;
5. connected the leak detector with the $TMP$;
6. switch on the leak detector;
7. when the leak detector is ready (on its screen you should read "pret a cycle") press "cycle" in order to make vacuum inside it;
8. when the vacuum is made close the connection between the primary pump and the $TMP$;
9. open the connection between the $TMP$ and the leak detector;
10. using the $He$ tank expose the flanges of the system to a small flux of $He$:
    - all the circumference of the flange must be exposed to the $He$ flux;
    - all the flanges that have been opened must be checked starting from the furthest from the pumping group;
11. if the quantity of $He$ on the screen of the leak detector increase significantly, then there is a leak. Attention must be payed to the fluctuation of the detector itself: sometimes the quantity of $He$ increase even if there is no leak in the system; therefore, when the flux on the display increases a lot, check again, because maybe it is just a fluctuation.
12. when it is clear that there are no leaks in the system, the leak detector can be disconnected from the system;
13. close the connection between the leak detector and the $TMP$;
14. open the connection between the $TMP$ and the primary pump;
15. switch off the leak detector.

## C.2 Bake-out Procedure

### C.2.1 Full Bake-out

After mounting the new sample on the machine a full bake-out of the machine is often required. This procedure consists in the heating of the whole machine in order to enhanced the outgassing of the contaminants gas from the walls. Once the particles have left the walls, they are pumped more easily and better pressure conditions can be reached inside the system in short time.
In the following of the section the whole procedure is described in details.

1. Put the heating bands around the whole system, paying attention the the bellow that is very fragile. The whole machine must be wrapped in aluminum foil in order to guarantee a more homogeneous heating;

2. dismount all the electronics equipment from the machine (the RGA electronics);

3. connect the thermocouples and the heating equipment to the right heating channels. In **Table C.1** are listed all the components of the system and the channel to which they must be connected.

4. program the heating channels using the *RAK system*. In **Table C.1** are listened the temperature at which all the components of the system must be heated:

All the bake-out procedure must be followed by the *degassing procedure*. During a degassing all the filaments inside the gauges are cleaned.
The standard procedure is described in the following of the section:

1. reassemble the RGA electronics dismounted before the bake-out;

2. open and close several times $V_1$, $V_2$ and GV in order to improve the releasee of the contaminants attached on their surfaces. Leave all the valves open;

3. degas the RGA.The degassing of the filament used for the pressure measurements (*filament 1*) last 45 min;

4. degas the SVT gauge.

    - look behind the control panel for the orange cable;
    - put this cable from the "measurement" plug to the "degassing" plug;
    - insert the bypass into the SVT gauge;
    - in the front of the control panel switch the control knob from "measurement" to "degassing";
    - switch on the power;
    - switch on the filament;
    - with the help of a little screwdriver change gradually the current in the filament from 0 mA to 50 mA. Change from a decade to the following one after the stabilization of the pressure in the system. The pressure can be checked using the Varian gauge;
    - once reached 50 mA wait for 30 min;
    - lower the current from 50 mA to 20 mA.

5. degas the Varian gauge pushing the button "degas" in its control panel. The degassing last approximately 15 min and must be repeated twice.

6. degas the electron source. This step must be performed after the heating of the sample at 120 °C and every time that we want to perform an ESD measurement.

   - remove the thermocouples from the sample;
   - put the safety box on the sample. Note that the system is built in such a way that the degassing cannot be performed without the safety box on the sample.
   - change the current flowing in the filament from 1 mA to 10 mA using the control knob;
   - switch on the high voltage;
   - switch on the current;
   - take note of the real current flowing in the filament. It can be read using an ammeter;
   - after 10 min switch off the current;
   - switch off the high voltage;
   - change the current flowing in the filament from 10 mA to 1 mA.

After the bake-out and the degassing the system is ready to be used for the measure of the sticking probability measurements and ESD measurement.

### C.2.2 Partial Bake-out

Sometimes instead of a total bake-out just a partial one is required after the mounting of a new sample on the machine. In this case only the sample vacuum chamber is heated; the electron source vacuum chamber is put in a static vacuum.

1. close GV;

2. close $V_2$;

3. open $V_{NEG}$;

4. open $V_1$;

5. put the heating bands around the sample vacuum chamber and then wrap everything with aluminum;

Table C.1: Heating temperatures of a full bake-out of the ESD system.

| TC | Increasing Time [h] | Steady Temperature [°C] | Duration [h] Time [h] | Decreasing Temperature [°C] | Degassing |
|---|---|---|---|---|---|
| 1 | 2 | 250 | 24 | 1 | 150 |
| 2 | 2 | 250 | 24 | 1 | 150 |
| 3 | 2 | 300 | 24 | 1 | 150 |
| 4 | 2 | 140 | 24 | 1 | 140 |
| 5 | 2 | 250 | 24 | 1 | 150 |
| 6 | 2 | 250 | 24 | 1 | 150 |
| 7 | 2 | 350 | 24 | 1 | 180 |
| 8 | 2 | 140 | 24 | 1 | 140 |
| 9 | 2 | 250 | 24 | 1 | 350 |
| 10 | 2 | 250 | 24 | 1 | 150 |
| 11 | 2 | 250 | 24 | 1 | 150 |
| 12 | 2 | 300 | 24 | 1 | 150 |
| 21 | | 80 | | | |
| 22 | 2 | 150 | 24 | 1 | 150 |
| 23 | | 80 | | | |
| 24 | 2 | 150 | 24 | 1 | 150 |
| 25 | | 80 | | | |
| 26 | 2 | 150 | 24 | 1 | 150 |
| 27 | 2 | 150 | 24 | 1 | 150 |
| 28 | 2 | 350 | 24 | 1 | 150 |
| 29 | 2 | 150 | 24 | 1 | 150 |
| 30 | 2 | 150 | 24 | 1 | 150 |
| 31 | 2 | 150 | 24 | 1 | 150 |
| 32 | 2 | 350 | 24 | 1 | 150 |

6. connect the thermocouples and the heating equipment to the right heating channels. In **Table C.2** are listed all the components of the system and the channel to which they must be connected.

7. program the heating channels using the *RAK system*. In **Table C.2** are listened the temperature at which all the components of the system must be heated:

After the bake-out and the degassing the system is ready to be used for the measure of the sticking probability measurements and ESD measurement. Once the degassing procedure is completed the sample must be activated in order to characterize it thanks to the sticking probability measurements and the ESD measurements.

## C.3 Activation Procedure

The standard procedure consists in heating the sample at increasing temperature in order to dissolve the oxide layer on its surface making it more reactive (activated). The

TABLE C.2: Heating temperatures of a partial bake-out of the ESD system.

| TC | Increasing Time [h] | Steady Temperature [°C] | Duration [h] Time [h] | Decreasing Temperature [°C] | Degassing |
|---|---|---|---|---|---|
| 2 | 2 | 250 | 24 | 1 | 150 |
| 4 | 2 | 140 | 24 | 1 | 140 |
| 5 | 2 | 250 | 24 | 1 | 150 |
| 6 | 2 | 250 | 24 | 1 | 150 |
| 10 | 2 | 250 | 24 | 1 | 150 |
| 11 | 2 | 250 | 24 | 1 | 150 |
| 12 | 2 | 300 | 24 | 1 | 150 |
| 21 | | 80 | | | |
| 22 | 2 | 150 | 24 | 1 | 150 |
| 23 | | 80 | | | |
| 24 | 2 | 150 | 24 | 1 | 150 |
| 25 | | 80 | | | |
| 26 | 2 | 150 | 24 | 1 | 150 |
| 27 | 2 | 150 | 24 | 1 | 150 |
| 28 | 2 | 350 | 24 | 1 | 150 |
| 29 | 2 | 150 | 24 | 1 | 150 |
| 30 | 2 | 150 | 24 | 1 | 150 |
| 31 | 2 | 150 | 24 | 1 | 150 |
| 32 | 2 | 350 | 24 | 1 | 150 |

first heating step is a 120 °C, then the temperature is increased by $40 - 50$ per step. Between a heating step and the following the measurements take place.
The first heating must be done when the system is still at the degassing temperature and the SVT gauge in the degassing mode with a current of 20 mA flowing in the filament. In the following the detail procedure is described both for the first heating and for the following one.

1. Close $GV$;
2. open $V_1$;
3. open $V_2$;
4. open $V_{NEG}$;
5. using the RAK system heat manually the sample to 120 °C. The heating lasts 2 h;
6. bring to 0 mA the current flowing in the SVT filament;
7. switch off the filament;
8. switch off the power;
9. remove the bypass on the SVT gauges;

10. turn the control knob from "degassing mode" to 10 mA;

11. put the orange cable from the "degassing" plug to the "measurement" plug;

12. switch on the power and the filament;

13. close $V_1$;

14. open $V_2$;

15. close $V_{NEG}$;

16. degas the electron source (for the complete procedure see Chapter **??** section C.2.1);

17. open GV;

18. take a RGA scan registering the pressure in the chambers:

    - open the folder *My Computer*;
    - open the folder *System (C:)*;
    - open the folder *QS32BIT*;
    - open the program *Measure*;
    - once in the program *Measure*, select *Scan*;
    - choose *Analog*;
    - choose *SCAC_ESD.SAP*;
    - once the scan has started, from the menu *file* select *Save Cycle Data*;
    - the file must be saved with a name that contains the year, the number of the sample and the number of the scan in the folder created for the sample;
    - on the screen will appear a window asking you the number of cycles to save: change from 1 cycle to 3;
    - select *save measurement+data+info*.

The procedure for the other heating steps (160 °C, 200 °C, 250 °C and 300 °) is described in the following:

1. close GV;

2. close $V_2$;

3. open $V_1$;

4. open $V_{NEG}$;

5. put the heating equipment on the sample;
6. program the heating in the RAK system;
7. take note of the pressure in the sample vacuum chamber at the beginning of the heating procedure, at the end of the heating ramp and at the end of the heating;
8. run a scan with the RGA taking note of the pressure;
9. close $V_1$;
10. open $V_2$;
11. degas the electron source (for the complete procedure see Chapter **??** section C.2.1);
12. open GV;
13. run a scan with the RGA taking note of the pressure in both the chambers.

In **Table C.3** the steps of the activation procedure are reported.

TABLE C.3: Steps of the ESD activation procedure.

| Increasing Time | Steady Temperature [°C] | Duration [h] Time [h] |
|---|---|---|
| manual | 120 | 2 |
| 1 h 30 min | 160 | 2 |
| 2 h | 200 | 2 |
| 2 h | 250 | 2 |
| 3 h | 300 | 2 |

## C.4 Sticking Probability Measurements

The first temperature step is at 120 °C in order to have a sample not activated. Increasing the temperature we make the its surface more reactive until the activation temperature. At this temperature the surface of the material behaves as a chemical pump.

1. Run a scan with the RGA in order to follow the time-evolution of different gas masses inside the system:
   - open the folder *My Computer*;
   - open the folder *System (C:)*;
   - open the folder *QS32BIT*;

- open the program *Measure*;
- once in the program *Measure* select *MID*;
- choose from the menu *Versus Time*;
- choose between the different file inside the folder opened *ZEROGASC.MIP*;
- once the scan has started, select from the menu *file Save Cycle Data*;
- the file must be saved with a name that contains the type of measurement, the number of the sample and the heating temperature in the folder created for the sample;
- on the screen will appear a window asking you the number of cycles to save: select 100000;
- select *save measurement+data+info*.

2. once the scan has started (and the RGA current is constant) begin the injection of $H_2$:

   - open $H_2$ calibrated leak;
   - open $V_{inj1}$ and $V_{inj2}$;
   - Close $V_{TMP}$;
   - take note of the pressure of the *Varian Gauge* and of the SVT Gauge and the cycle;

3. When the equilibrium of $H_2$ is reached, take note of the cycle and of the pressure of the *Varian Gauge* and of the SVT Gauge;

4. stop the injection of $H_2$:

   - open $V_{TMP}$;
   - close $V_{inj1}$ and $V_{inj2}$;
   - close $H_2$ calibrated leak;

5. when the RGA current is constant and has the same intensity of the current before the $H_2$ injection, the injection of CO can begin:

   - open $CO$ calibrated leaks;
   - open $V_{inj1}$ and $V_{inj2}$;
   - Close $V_{TMP}$;
   - take note of the pressure of the *Varian Gauge* and of the SVT Gauge and the cycle;

6. since long time has to waited for the *CO* saturation of the NEG surface, it has been decided to take as reference point for the measurement the $5^{th}$ cycle after the injection of *CO* in the system. Take, therefore, note of the pressure of the *Varian Gauge* and of the SVT Gauge for this cycle when it is reached;

7. stop the injection of *CO*:

   - open $V_{TMP}$;
   - close $V_{inj1}$ and $V_{inj2}$;
   - close *CO* calibrated leaks;

This procedure must be followed for the sticking probability measurement after each heating step.

## C.5 Electron Stimulated Desorption Measurements

In the following the detailed procedure for performing an electron stimulated desorption measurement is reported.

1. Make sure that the *Gate Valve* is completely open;
2. descend the electron source pushing the button *descend*;
3. Rewire the HV supply;
4. check that there are no short cuts using an ammeter;
5. Put the security box on the machine.
6. Save the measurement;
7. Take note of the cycle, pressure and current;
8. Turn on the electron source and take note of the current on the filament (around $1mA$);
9. The measure lasts $100s$;
10. Passed $100s$ take note of the cycle, pressure and current;
11. Turn off the electron source;
12. Turn off the HV;
13. Rewire HV power supply;

14. Retract the electron source;
15. Close $V_2$;
16. Open $V_1$;
17. Open $V_{NEG}$;
18. Close the gate valve.

This procedure must be followed for the ESD measurement after each heating step.

# Bibliography

[1] C Benvenuti. Recent Advances in Vacuum Techniques for Particle Accelerators. In *Proceeding of the Tenth International Conference on Cyclotrons and their Applications*, pages 540–546, Eadt Lansing MI USA, 30 April-3 May 1984.

[2] C Benvenuti, J M Cazeneuve, P Chiggiato, F Cicora, A Escudeiro-Santana, V Johanek, V Ruzinov, and J Fraxedas. A Novel Route to Extreme Vacua: the Non-Evaporable Getter Thin Film Coatings. *Vacuum*, 53(1-2):219–25, 1999.

[3] A E Prodromides, C Scheuerlein, M Taborelli. Lowering the Activation Temperature of TiZrV Non-Evaporable Getter Films [for LHC]. *Vacuum*, 60(1-2):35–41, 2001.

[4] C Benvenuti, P Chiggiato, P Costa-Pinto, A Escudeiro-Santana, T Hedley, A Mongelluzzo, V Ruzinov, and I Wevers. Vacuum Properties of TiZrV Non-Evaporable Getter Films [for LHC Vacuum System]. *Vacuum*, 60(1-2):57–65, 2001.

[5] A E Prodromides. *Non-Evaporable Getter Thin Film Coatings for Vacuum Applications*. PhD thesis, Ecole Polytechnique, Lausanne, Genève, September 2002.

[6] P Chiggiato, R Kersevan. Synchrotron Radiation-Induced Desorption from a NEG-Coated Vacuum Chamber [of ESRF Beamline]. *Vacuum*, 60(1-2):67–72, 2001.

[7] E Fischer, H Mommsen. Montecarlo Computations on Molecular Flow in Pumping Speed Test Domes. *Vacuum*, 17(309-315), 1967.

[8] April 2014. URL http://www.symmetrymagazine.org/article/april-2014/ten-things-you-might-not-know-about-particle-accelerators.

[9] O. Gröbner C. Benvenuti, R. Calder. Vacuum for Particle Accelerators and Storage Rings. *Vacuum*, 37(6):699 – 707, 1987.

[10] C Benvenuti. Non-evaporable getters: from pumping strips to thin film coatings. Technical report, CERN, 1998.

[11] P Chiggiato, P Costa-Pinto. TiZrV Non-Evaporable Getter Films: from Development to Large Scale Production for the Large Hadron Collider. *Thin Solid Films*, 515(CERN-TS-2006-001. 2):382–388. 13 p, December 2005.

[12] C Benvenuti. A New Pumping Approach for the Large Electron Positron Collider (LEP). *Nuclear Instruments and Methods*, 205:391–401, 1983.

[13] P Chiggiato, C Benvenuti. Obtention of Pressures in the $10^{-14}$ Torr Range by Means of a ZrVFe Non Evaporable Getter. *Vacuum*, 44(5-7):511–513, 1993.

[14] R. Kersevan. NEG-Coated Vacuum Chambers at the ESRF: Present Status and Future Plans. In *Proceeding of EPAC*, Paris, June 2002.

[15] V Johanek, P Chiggiato, JM Cazeneuve. internal note CERN-EST-SM-DA, 1998.

[16] R. Kersevan. Performance of a Narrow-Gap, NEG-Coated, Extruded Aluminum Vacuum Chamber at the ESRF. In *Proceeding of EPAC*, Wien, 2000.

[17] F Cicoira, C Benvenuti, P Chiggiato, Y. L'Aminot. Nonevaporable Getter Films for Ultrahigh Vacuum Applications. *Journal of Vacuum Science & Technology A*, 16(148), 1998.

[18] C Benvenuti, S Calatroni, J Carver, P Chiggiato, H Neupert, W Vollenberg, S Amorosi, M Anderle. Study of the Discharge Gas Trapping During Thin Film Growth. In *Proceeding of the Sixth European Vacuum Conference*, Lyon, Dec 1999.

[19] C Benvenuti. Molecular Surface Pumping: The Getters Pumps. In *Proceeding of the CERN Accelerator School*, Scanticon Conference Center; Snekersten, Denmark, 28 May - 3 June 1999.

[20] A E Prodromides, C Benvenuti, P Chiggiato, A Mongelluzzo, V Ruzinov, C Scheuerlein, M Taborelli, F Lévy. Influence of the Elemental Composition and Crystal Structure on the Vacuum Properties of TiZrV Non-Evaporable Getter Films. Technical Report CERN-EST-2001-002-SM",, CERN, Geneva, Jul 2001.

[21] P Costa-Pinto, C Benvenuti, P Chiggiato, A E Prodromides, V Ruzinov. Influence of the Substrate Coating Temperature on the Vacuum Properties of TiZrV Non-Evaporable Getter Films. *Vacuum*, 71(1-2 Spec.):307–315, 2003.

[22] James M. Lafferty, editor. *Foundations of Vacuum Science and Technology.* Wiley-Interscience Publication, 1998.

[23] C Benvenuti, A Escudeiro-Santana, V Ruzinov. Ultimate pressures achieved in TiZrV Sputter-Coated Vacuum Chambers. *Vacuum*, 60(CERN-EST-99-008-SM. 1-2):279–84. 6 p, Dec 1999.

[24] Sir James Jeans. *An Introduction to the Kinetic Theory of Gases.* Cambridge University Press, Cambridge, 1967.

[25] P. Chiggiato. Vacuum technology for particle accelerators.

[26] Hiro Tawara Yasunori Yamamura. Energy Dependence of Ion-Induced Sputtering Yields from Monoatomic Solids at Normal Incidence. *National Institute for Fusion Science, Chigusa-ku, Nagoya, 464-01, Japan*, 1996.

[27] J S Colligon, A Hannah, R Valizadeh, O. B Malyshev, V. M Vishnyakov. Comparison oF TiZrV Nonevaporable Getter Films Deposited Using Alloy or Twisted Wire Sputter-Targets. *Journal of Vacuum Science & Technology A*, 28(1404), 2010.

[28] J.T Yate Jr, R.D Ramsiee. Electron-Stimulated Desorption: Principles and Applications. *Surface Science Reports*, 12:246–378, 1991.

[29] R Gamer D Menzel. Desorption from Surfaces by Slow Electron Impact. *Journal of Chemical Physics*, 40:1164, 1964.

[30] P. A Readhead. Interactions of Slow Electrons with Chemisorbed Oxygen. *Canadian Journal of Physics*, 42:886, 1964.

[31] M Taborelli. Quality Control of TiZrV NEG Coatings by X-Ray Electron Spectroscopy. SOP-MME-SC-05 EDMS Id: 630214, CERN, 2005.

[32] L. E Alexander, H. P Klug. *X-Ray Diffraction Procedure: for Polycrystalline and Amorphous Materials.* Wiley-Interscience Publication, New York, second edition edition, 1974.

[33] G. Bregliozzi. Template for the Bake-Out and Activation of the LSS NEG Coated Beam Pipes. Technical report, CERN.

[34] A N Hannah, O. B Malyshev, R Valizadeh. Pumping Properties of TiZrHfV Non-Evaporable Getter Coating. *Vacuum*, 100(26 e 28), 2014.